Development of paper-based biosensors for DNA recognition and proteolytic activity

Hélvio Miguel Rodrigues Simões

Thesis to obtain the Master of Science Degree in

Biotechnology

Supervisors: Professor Duarte Miguel de França Teixeira dos Prazeres

Examination Committee

Chairperson: Professor Arsénio do Carmo Sales Mendes Fialho

Supervisor: Professor Duarte Miguel de França Teixeira dos Prazeres

Members of the Committee: Doctor Pedro Miguel Neves Ribeiro Paulo

September 2019

Preface

The work presented in this thesis was performed at the Institute for Bioengineering and Biosciences of Instituto Superior Técnico (Lisbon, Portugal), during the period October 2018-July 2019, under the supervision of Prof. Miguel Prazeres and in the context of the project “CBM-X: Biorecognition as a Tool for the Functionalization of Cellulose-based Materials with Biomolecules and Nanostructures” (PTDC/CTM-CTM/30790/2017), funded by Fundação para a Ciência e Tecnologia.

Declaration

I declare that this document is an original work of my own authorship and that it fulfills all the requirements of the Code of Conduct and Good Practices of the Universidade of Lisboa.

Acknowledgements

I would like to start by thanking my supervisor, Professor Miguel Prazeres, for giving me a try at this project, as well as for the helpful guidance and availability that was shown to me. It really made this whole process a lot easier.

Talking about guidance, I would be remiss not to mention the incredible help that Cláudia Alves and Rui Silva gave me during the last year. Thank you for showing me the ropes around the lab, for sharing with me your knowledge and for being all-around good friends.

I extend this thank you to all the remaining people of the 7th and 8th floors, especially to my colleagues of the 7-6.7, 7-6.10, 7-6.11 and 8-6.11. I'm sure I would forget names if I started mentioning them one by one, so it's best I just leave it at that.

To the friends I made along my academic life, thank you for the sharing of ideas, moments and, most of all, good times. Special thanks to João Rocha and Natércia Marcelino, for being good friends since the FCUL days and being there for me up to now, and to Luís Almeida, that despite being far away taking over the world, still remains present in my mind in the lesson that he taught me that if at first you don't succeed, you may have better luck on the second try.

To my friends and family, thank you for putting up with me in these more trying times. A major thank you to my roommates Daniel Domingos and Pedro Tremoceiro and my parents, for enduring my endless pacing around and spinning in my chair when I am trying to think, and for supporting me the whole way through.

Abstract

The design of new diagnostic solutions that are more affordable and easier to manage is of great interest for economic and health safety reasons. These tests should be simple, portable and requiring small sample volumes with little to no preparation, so they can be used at the point of care (POC) without the need for elaborate equipment. The ubiquity and ease of handling of paper make it an excellent support for such tests. One strategy to achieve this goal is to combine paper with gold nanoparticles (AuNPs), which produce a colorimetric signal visible to the naked eye. In this work, two tests were developed using AuNPs detection by bioactivating cellulose with the carbohydrate binding module CBM3-C. This protein was thoroughly characterized and employed for sensing a) complementary DNA (cDNA) capture and b) proteolytic activity. For cDNA recognition, a capture oligonucleotide was conjugated with CBM3-C using two different strategies: i) the formation of a nickel complex with trisNTA-modified oligonucleotides via the hexa-histidine tag of CBM3-C and ii) the formation of a covalent bond between the terminal thiol moiety of CBM3-C and maleimide-modified oligonucleotides. Recognition of cDNA by the conjugates was performed in a wax-printed microfluidic device both directly and indirectly, in a 2- or 3-oligonucleotide system, respectively. The nickel complex conjugate was able to accurately detect cDNA in the 2-oligonucleotide system, but the covalent conjugate was less discriminatory. Both conjugates returned positive signals in assays without the target strand. CBM3-C was also successfully used in a proof-of-concept assay for measurement of the extent of a proteolytic reaction using a non-specific protease.

Key words: Biosensor, Paper-Based Devices, Gold Nanoparticles, Carbohydrate-Binding Module, DNA recognition, Proteolytic Activity

Resumo

O design de novos testes de diagnóstico mais acessíveis é de grande interesse por razões económicas e de saúde. Estes testes deverão ser simples, portáteis e exigir pequenos volumes de amostra com pouca a nenhuma preparação prévia, para que possam ser aplicados no ponto de tratamento sem necessitar de equipamentos sofisticados. A ubiquidade e facilidade de manuseio do papel fazem dele um bom suporte para este tipo de testes (PADs). A combinação com nanopartículas de ouro (AuNPs), que produzem um sinal colorimétrico a olho nu, é uma estratégia para atingir esse objetivo. Neste trabalho, dois testes em papel foram desenvolvidos recorrendo a AuNPs para detecção e utilizando celulose ativada com o módulo de ligação a carbohidratos CBM3-C. Esta proteína foi caracterizada e utilizada para detetar a captura de DNA complementar (cDNA), bem como atividade proteolítica. Para o reconhecimento de cDNA, duas estratégias de conjugação de CBM3:DNA foram exploradas: i) formação de complexo de níquel com oligonucleótidos modificados com NTA via tag de hexa-histidinas e ii) formação de ligação covalente entre um grupo tiol terminal do CBM3-C e oligonucleótidos modificados com maleimida. Os conjugados permitiram reconhecer DNA complementar tanta direta como indiretamente, num sistema de 2 ou 3 oligonucleótidos, respectivamente usando dispositivos microfluídicos delimitados por cera. O conjugado via complexo de níquel consegue distinguir cDNA no sistema de 2 oligonucleótidos, tendo os conjugados preparados por ligação covalente sido menos discriminatórios. Ambos os conjugados deram sinal positivo sem a cadeia cDNA alvo. O CBM3-C foi também usado num ensaio de prova de conceito, medindo a extensão de uma reação proteolítica por uma protease não específica.

Palavras-chave: Biosensor, Dispositivos de Papel, Nanopartículas de Ouro, Carbohydrate-Binding Module, Reconhecimento de DNA, Atividade Proteolítica

Table of contents

List of tables

List of figures

List of abbreviations

µPAD	Microfluidic Paper-Based Analytical Device
APS	Ammonium Persulfate
AuNPs	Gold Nanoparticles
BCA	Bicinchoninic Acid
BSA	Bovine Serum Albumin
CAZy	Carbohydrate-Active Enzymes database
CAZymes	Carbohydrate-Active Enzymes
CBDs	Cellulose Binding Domains
CBHI	Cellobiohydrolase I
CBMs	Carbohydrate-Binding Modules
cDNA	Complementary DNA
CenA	Endo-β-1,4-glucanase
CexA	Exo-β-1,4-glucanase
CNTs	Carbon nanotubes
DMSO	Dimethyl Sulfoxide
DNA	Deoxyribonucleic Acid
dsDNA	Double-Stranded DNA
DTSSP	3,3'-dithiobis(sulfosuccinimidyl propionate)
ePAD	µPAD coupled with electrochemical detection
LFA	Lateral Flow Assay
NTA	Nitrilotriacetic acid
PAD	Paper-Based Analytical Device
PAGE	Polyacrylamide Gel Electrophoresis
PDMS	poly(dimethylsiloxane)
POC	Point-Of-Care
RNA	Ribonucleic Acid

RPLC	Reverse-Phase Liquid Chromatography
SARS	Severe Acute Respiratory Syndrome
SDS	Sodium Dodecyl Sulfate
SEC	Size Exclusion Chromatography
SEM	Scanning Electron Microscopy
SPCE	Screen-Printed Carbon Electrode
ssDNA	Single-Stranded DNA
sSMCC	sulfosuccinimidyl 4-[*N*-maleimidomethyl]cyclohexane-1-carboxylate
TCEP	tris(2-carboxyethyl)phosphine
TEMED	tetramethylethylenediamine
TST	Tris-Saline-Tween buffer

1. Introduction

1.1. The need for better diagnostics

In an ever-changing world, the search for faster, more reliable and affordable methods of diagnosis is paramount. Better diagnostics would be of major support in several areas related to global health, such as environmental safety, food and water quality testing and disease control. As these three factors are very interconnected, a rampant uncontrolled outbreak can lead to serious problems worldwide.

Over the last 19 years, there have already been quite a few major pandemics, from severe acute respiratory syndrome (SARS) in 2003 in Asia, the H1N1 influenza in 2009, the Ebola virus outbreak in 2014, to the Zika virus epidemic of 2015-16. In order to better contain these diseases, their cause needs to be identified and those affected need to be readily diagnosed. Thus, faster methods of diagnostics would be of utmost assistance in managing disease spread. In 2016, the Commission on a Global Health Risk Framework for the Future from the National Academy of Medicine published a report estimating a cost of over $6 trillion in the 21st century – more than $60 billion per year – for pandemic disease events response[1] (Figure 1). The Commission also recommended investing $4.5 billion annually in order to reduce the threat generated by said events – this includes $1 billion on R&D – to try to find low-cost, more effective diagnostics. Responding to the Ebola outbreak of 2014, Bill Gates identified several factors that should be improved in the future in order to have a more robust response to eventual pandemics[2]. He defended that conventional laboratory testing is not suitable for the rapid response to pandemics. The required equipment for detection and diagnosis of Ebola patients is not field-deployable, and the affected regions, normally developing countries, don't possess enough skilled workforce in order to respond to the growing demands. Also, Bill Gates endorsed a decentralization of testing, which needs to be more accessible at the point-of-need, as well as an increased affordability of the diagnostics method.

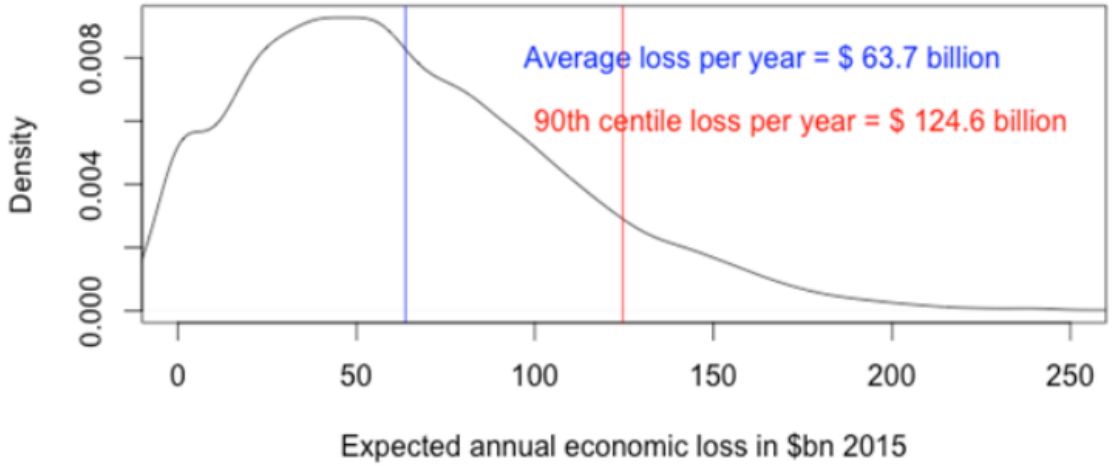

Figure 1: Distribution of expected economic losses related to pandemics response and treatment in the 21st century.
From GHRF Commission, 2016, Appendix C[1].

1.1.1. Point-of-care diagnostics

According to the World Health Organization, an appropriate diagnostic test should follow the ASSURED criteria: Affordable, Sensitive, Specific, User-friendly, Rapid and robust, Equipment-free and Deliverable to end-users[3].The introduction of point-of-care (POC) testing aims to meet these conditions and solve some of the aforementioned bottlenecks. Requiring minute amounts of sample with low analyte concentration and little to no preparation, POC diagnostics are tailored for the quick responses needed in case of a pandemics outbreak. As they are simple and user-friendly, they can be deployed on the field without the need for expert technicians; because they are inexpensive, they can be afforded even by developing countries, whose limited resources could bar them from purchasing more sophisticated technologies. Furthermore, the speed inherent to POC diagnostics makes them a perfect tool to provide an adequate response to pandemics.

According to a report by Grand View Research, the global POC diagnostics market was valued at $18.09 billion in 2018 with a Compound Annual Growth Rate of 3.3% until 2025. The report further estimates that the continuous developments in R&D focusing on miniaturizing molecular diagnostic tests, combined with improvements in lab automation techniques might propel the growth even higher[4]. This growth in POC diagnostics is exemplified in Figure 2, which displays estimates of the market size in the United Kingdom, separated by type of product.

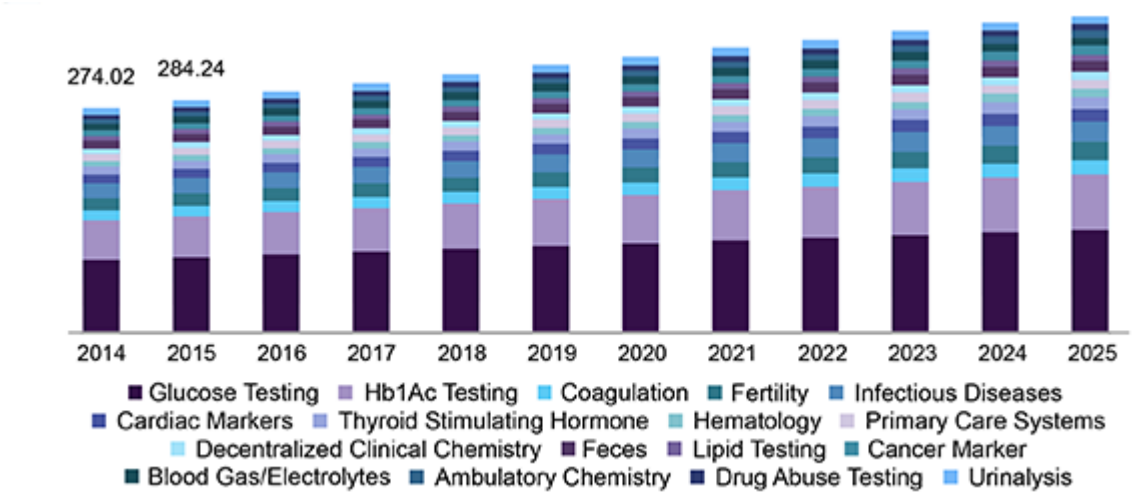

Figure 2: Market Size of POC diagnostics in the United Kingdom, separated by type of product, from 2014 to 2025 (in $ Million). Adapted from Grand View Research report[4].

POC diagnostics includes a variety of tests. The most common POC tests are blood glucose monitoring[5] and home pregnancy tests[6]. Other applications for POC tests have been developed, such as the detection of carpal tunnel syndrome, in which the device measures nerve conduction[7]. A POC cardiac troponin assay proved helpful in aiding the diagnostic of Troponin-only Manchester Acute Coronary Syndromes[8]. POC tests can also be useful in detecting diseases such as Ebola, whose initial symptoms closely mimic other diseases such as malaria[9]. Detection of drugs of abuse in urine samples is also possible with POC tests[10,11]. Applications not directly involving human health are also being pursued, as exemplified by the testing of genetically modified crops[12] and the on-farm diagnosis of mastitis[13]. POC tests are often conducted using instruments and devices that are portable, easy to

transport and handheld. Many of these devices operate on the basis of the transport and distribution of very small volumes of analyte-containing samples and reagents. Such microfluidic POC diagnostics come in all shapes, sizes, and materials. Traditionally, microfluidic devices were made from silicon and glass, which provide a defined geometry and inertness[14,15]. However, these materials had a drawback: high expense on scalability. Current polymers such as poly(dimethylsiloxane) (PDMS) have also been used in POC diagnostic devices. These materials are moderate in cost and are somewhat capable of mass fabrication. Despite this, the trend in microfluidic POC diagnostics seems to be moving towards the use of more affordable materials, such as paper[16] or thread[17]. Besides cutting production costs, the use of these materials would facilitate scalability and improve usability.

1.2. Paper as a substrate material

Having paper, or other porous hydrophilic materials, as the substrate for POC diagnostics has unique advantages over materials like glass, silicon or PDMS. In addition to being cheap and ubiquitous, paper displays a set of very convenient features: (i) it has an inherent ability to wick fluids, i.e., it is able to transport fluids without the need for external pumping instrumentation; (ii) it can hold/store active reagents in its fiber network; (iii) its high surface area to volume ratio improves detection limits, e.g. if a colorimetric method should be used; (iv) it can be easily modified, whether by cutting and folding or by chemical treatment; (v) it is easy to scale by printing; and (vi) it is easy to dispose of by incineration. Due to these characteristics, paper has been used in various analytical testing applications, ranging from spot tests for metals[18] to dipstick tests for diabetes[19], detection of foodborne pathogens[20] and lateral flow assays (LFA)[21]. Paper can also be used even if the available sample amount is low. Such microfluidic paper-based analytical devices (µPAD) were first developed in 2007 by Martinez et al. who designed an innovative patterned paper assay for the detection of artificial samples of glucose and protein in clinically relevant ranges[22].

1.2.1. Microfluidic paper-based analytical devices

The standard µPAD consists of a paper strip with a given geometric arrangement of channels and target areas defined by boundaries, that guide and confine fluids in the device. The earliest paper-based tests used manually cut paper pre-treated with a chemical reagent, which would react with an analyte and produce a colored product[16]. The introduction of said boundaries allowed the µPAD to incorporate different functions, defining different areas, each with a different purpose.

The first µPADs were made using photoresist to create the barriers[22,23], but this material was abandoned due to its cost and potential for background reactivity. Instead, and more advantageously, the boundaries of the system can be made out of inert, low-cost materials such as wax[24]. The method used to apply the wax to paper can range from manual application and stamping[25], to printing with wax-based office printers[24]. With this latter method, the boundaries of the microfluidic network are first printed on the surface of an adequate paper matrix using a solid, hydrophobic, wax-based ink. The paper with the imprinted design is then heated – this melts the wax that was deposited on the surface and promotes its vertical diffusion. The final result is a three-dimensional barrier across the thickness of the paper, which is impervious to most aqueous-based solutions. As printing turned out to be the most successful

µPAD fabrication method, some slightly more complex designs have also been developed, such as hemi-enclosed channels within the paper (in opposition to fully-enclosed channels)[26]. Applying different amounts or thicknesses of wax can also change the size of the created channels[27]. Alternatives to wax printing have also been developed, the most common being inkjet printing, flexographic printing, photolithography and simple paper cutting/reshaping[16].

1.2.2. Immobilization of biomolecules in paper

Several components need to be assembled when setting up a typical µPAD or LFA (Figure 3). The ultimate goal is to define areas in the circuit for sample loading, deposition of reagents and occurrence of recognition events. The areas in the paper surface designed for test and control reactions are often functionalized with some kind of bioreceptor (e.g. antibodies, DNA strands). The key role of this component is to capture the analyte, via biorecognition, in a precise location. Other events follow involving secondary reagents that ultimately produce an observable and measurable signal that confirms detection. In order to correctly deposit the desired bioreceptors in the designated locations, immobilization must be done in such a way that minimizes non-specific adsorption. In this regard, the use of paper as a substrate is disadvantageous, due to the abundant hydroxy groups present in the cellulose fiber surface. Immobilization via physical adsorption, through Van der Waals forces, hydrogen bonds and hydrophobic interactions, results in a matrix with low surface density, arbitrary orientation of the bioreceptor and levels of adsorption that vary depending on the chemistry of the biomolecules used. Covalent binding, although an effective method of immobilization, would require activation of the hydroxy groups of cellulose, transforming them into more reactive groups, more suitable to covalent coupling. Lastly, the target bioreceptor molecule can be conjugated to a protein with affinity to cellulose, thus allowing specific local immobilization and avoiding non-specific binding to the paper matrix. Carbohydrate-binding modules are one such family of cellulose-interacting proteins.

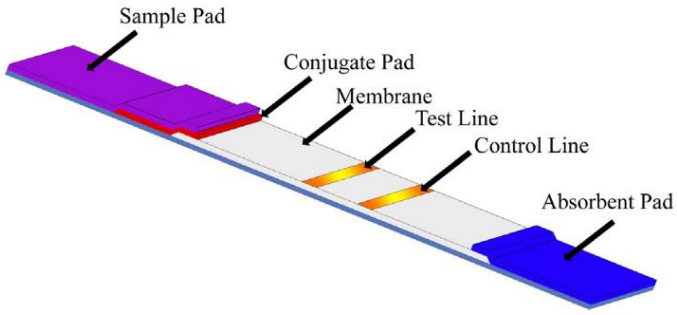

Figure 3: Schematic view of a standard lateral flow test strip, with the most common zones of interest. From Syedmoradi et al.[28]

1.3. Carbohydrate-binding Modules

Carbohydrate-Binding Modules (CBMs) are contiguous sequences of amino acid residues present in a carbohydrate-active enzyme (CAZyme) with a structurally discrete fold that displays carbohydrate-binding activity[29–31]. CBMs do not possess any catalytic activity themselves, but are often found accompanying catalytic domains, directing them to their substrate[32]. CBMs (originally termed as cellulose binding domains, CBDs) were first successfully isolated in the late 1980s from

cellobiohydrolase CBHI from *Trichoderma reesei*[33] and cellulases CenA and CexA from *Cellulomonas fimi*[34]. The discovery of these sugar-binding proteins confirmed the suspicions that arose in the 1940s, when Reese and co-workers proposed that an unknown nonhydrolytic component had a role in the destabilization of the cellulose structure, leading to the enzymatic degradation of crystalline cellulose[35].

The earlier designation of CBD was challenged when an increasing number of modules that fit the criteria of a CBD but bound carbohydrates other than cellulose, such as starch[36], were found in CAZymes. Since the change in nomenclature, CBMs have been found affixed on enzymes that interact with most carbohydrate materials, from cellulose and xylan to algal saccharides and yeast cell wall glucans.

1.3.1. Classification of CBMs

An updated list of CBM-containing proteins organized by CBM family is maintained in the Carbohydrate-Active Enzymes database (CAZy, http://www.cazy.org)[37]. As of September 12, there are 183919 known CBMs, 183030 of which are classified into one of 85 available families. CBM families are established on the basis of amino acid similarity. However, CBMs within the same family can bind different carbohydrate ligands.

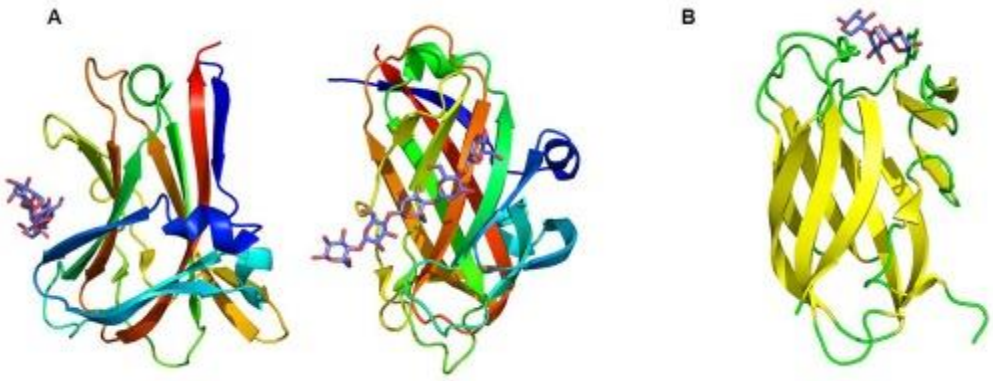

Figure 4: The CBM β-sandwich fold. A – CBM27 from *Thermotoga maritima* mannanase, side and front view (PDB ID 1OF4)[38]. B – CBM6 from *Clostridium stercorarium* xylanase (PDB ID 1NAE)[39]. Binding sites of CBMs in A and B are located in the face and loop region of the β- sheet, respectively. Image taken from CAZypedia website[40].

CBMs can also be classified into one of 7 fold families[29]. The β-sandwich fold, which is the most common across CBM, comprises two β-sheets, each one with three to six antiparallel β-strands (Figure 4). The ligand may bind to one of the faces of the β-sheet (Figure 4A) or within the variable loop region of the β-sheet (Figure 4B). The remaining fold families and the corresponding CBM families are presented in Table 1.

Table 1: CBM fold families. Adapted from Oliveira et al, 2015[41].

Fold Family	Fold	CBM families
1	β-Sandwich	2, 3, 4, 6, 9, 11, 15, 16, 17, 20, 21, 22, 25, 26, 27, 28, 29, 30, 31, 32, 33, 34, 35, 36, 40, 41, 42, 44, 47, 48, 51, 70
2	β-Trefoil	13, 42
3	Cysteine knot	1
4	Unique	5, 12
5	OB fold	10
6	Hevein fold	18
7	Hevein-like fold	14

Furthermore, CBMs are also classified into three types (A, B and C)[31], depending on the shape and degree of polymerization of the target ligand. Type A CBMs bind to crystalline surfaces. This is made possible due to the abundance of aromatic amino acids in the CBM binding site, which form a flat platform that matches the planar surface of carbohydrates such as chitin or cellulose[42]. Type B and type C CBMs bind to different parts of the amorphous region of carbohydrates. Type B CBMs bind to internal glycan chains and are able to accommodate longer sugar chains in their groove-like binding sites. Type C CBM's bind to the termini of glycans, as their binding sites are short pockets that recognize one to three monosaccharide units. The binding of the three types of CBM is schematically shown in Figure 5.

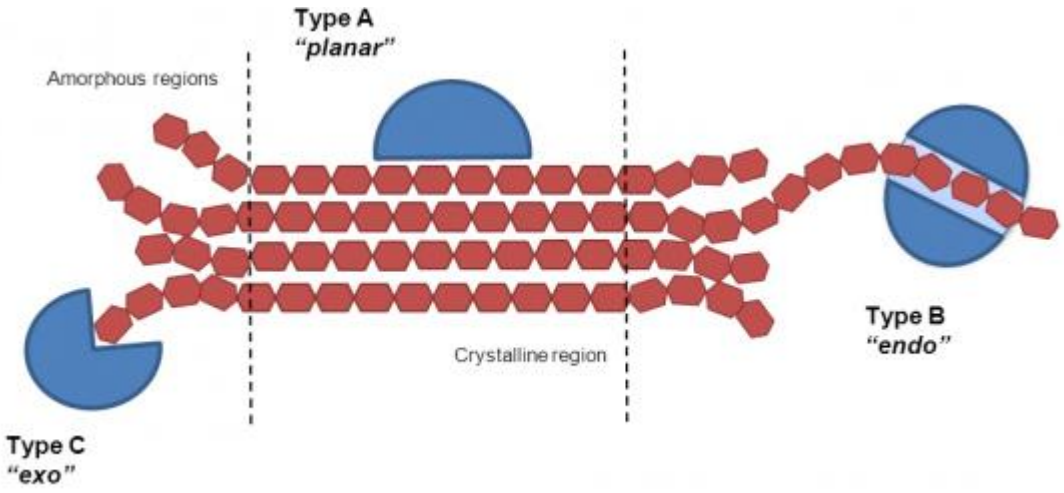

Figure 5: Types of CBM. Visual representation of the three types of CBM highlighting the binding to different regions of the polysaccharide substrate. Image adapted from the CAZypedia webpage[40].

1.3.2. Biotechnological interest of CBMs

CBMs have been widely used in various biotechnological applications, from enzyme immobilization to bioremediation (Figure 6). For biosensing purposes, Type A CBMs show greater potential due to their ability to bind to the paper's fibrous cellulosic matrix. In order to be useful in biosensors, CBMs are

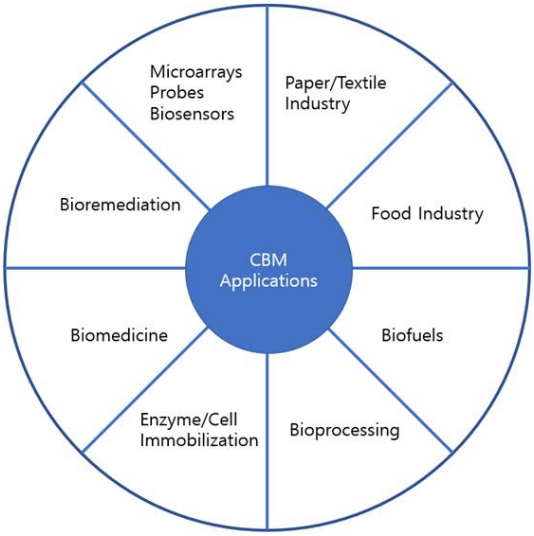

Figure 6: Panorama of the major areas of biotechnological application of CBMs.

usually fused to the target bioreceptor. With this strategy, the CBM moiety grants the fusion binding to a solid support while the remaining bioreceptor moieties are free to play their role in analyte capture or detection. For example, an autoclavable, regenerable glucose biosensor has been successfully developed and applied in microbial fermentation monitoring and control by resorting to a fusion of glucose oxidase to a CBM[43,44]. In another application, Tolba et al developed a method for oriented immobilization of bacteriophage T4 by fusing a *cbm* gene with the small outer capsid protein gene. The recombinant phages retained their lytic activity and were able to specifically capture and infect the host bacterium, detecting as few as 800 cells within 2 hours. Detection of *E. coli* cells captured by the immobilized phages was done by a phage multiplication assay coupled with real-time PCR[45]. A different method for detection of *E. coli* cells in water was recently developed by Hinkley et al[46]. This group created a reporter bacteriophage by genetically engineering a T7 coliphage in order to express a fusion of NanoLuc, a newly developed luciferase, with a CBM. In the developed assay, the water sample is first supplemented with concentration growth media to allow resuscitation of *E. coli,* and after an incubation period, the reporter phage and microcrystalline cellulose are added. This allows infection of the present *E. coli* cells and expression of NanoLuc-CBM occurs, which will bind to the cellulose (Figure 7). The cellulose was pelleted and then its luminescence was evaluated. Detection of *Staphylococcus aureus* cells was also possible with a fusion of five CBM9s with five human anti-*S. aureus* antibodies, linked by a verotoxin B subunit. After impregnation of the CBM fusion in cellulose fibers, detection of *S. aureus* binding was done by transferring the cellulose to a 96-well microtiter plate and submerging it in peroxidase substrate, which created color that could be measured at 450 nm[47]. Immunoassays involving CBM have also been shown to provide an accurate DNA recognition system, whether using µPADs[48] or cellulose microparticles in an aqueous suspension[49], by using a fusion of a CBM with the ZZ fragment of the staphylococcal protein A. The fusion captures IgG antibodies through their Fc portion. Immobilization of an anti-biotin IgG led to accurate capture of biotinylated DNA.

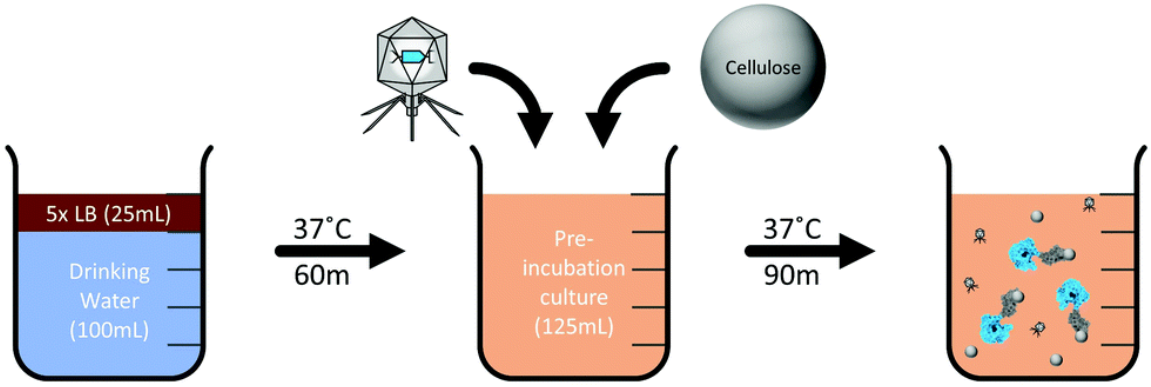

Figure 7: Schematic representation of the assay for detection of *E. coli* cells in water using the T7 coliphage genetically engineered with a NanoLuc-CBM fusion. Image taken from Hinkley et al[46].

1.4. Detection of signals in paper-based biosensors

With the issue of correct bioreceptor immobilization on paper tackled, it is important to figure out how the binding of the analyte to the bioreceptor will be recognized. Different signal reporters may be used for this purpose. Detection of analytes in PADs has been successful using chemiluminescence, fluorescence, electrochemical sensing and colorimetric methods. The sensitivity of these methods has been increasing recently with the development of the nanotechnology field, namely its association with medical diagnostics. An increasing number of POC biosensors have been reported using carbon nanotubes, graphene and metal nanoparticles, which allow detection of trace concentrations of analytes[50]. Overall, the incorporation of nanomaterials in POC assays is advantageous since it results in sensitive, rapid and cost-effective assays, with sample amounts being minimal[28,50].

1.4.1. Chemiluminescence

Biosensors based in chemiluminescence measure the intensity of light emitted by a chemical reaction. The interest in this detection method stems from the fact that typical necessary reagents are inexpensive, while the measurement is highly sensitive[16]. For example, Zhou et al.[51] developed a DNA hybridization sensor in which a biotinylated DNA target probe containing Cy3-labeled oligonucleotides hybridized with single-stranded DNA probes present in a complex of green-emitting upconverting phosphors functionalized with streptavidin and immobilized via adsorption on paper. After excitation of the conjugate probe at 980 nm, the luminescence emission was measured by an epifluorescence microscope.

As a subset of this type of detection, electrochemiluminescence uses electrochemical reactions to generate luminescence. This modality can be preferable to chemiluminescence due to its lower background optical signals, ease of controlling electrode potential vs controlling reagent addition at precise timepoints, and enhanced selectivity by control of electrode potential[16]. For example, Delaney et al.[52] used a mobile phone camera to detect electrochemiluminescence, with the electrochemical reaction being initiated by driving electrode potential from the audio socket of said phone. Software on the phone could control the frequency, amplitude and duration of the pulses that were sent to the paper-

based electrode. Videos of the reaction were taken and red-channel intensity of individual frames was proportional to analyte concentration.

1.4.2. Fluorescence

The use of fluorophores in µPADs is interesting due to their sensitivity. On the other hand, the addition of paper whitening chemicals can increase background fluorescence. DNA recognition sensors with CBMs have been successfully made using fluorophores as signal reporters[48]. In one example, a CBM3 from *Clostridium thermocellum* was fused with the ZZ fragment of the staphylococcal protein A, that recognizes IgG antibodies through their Fc portion. Biotinylated DNA strands were captured by an anti-biotin IgG bound to the CBM-ZZ fusion. The subsequent hybridization of a fluorescein-labeled complementary DNA strand was then confirmed by detection of fluorescence emission (Figure 8).

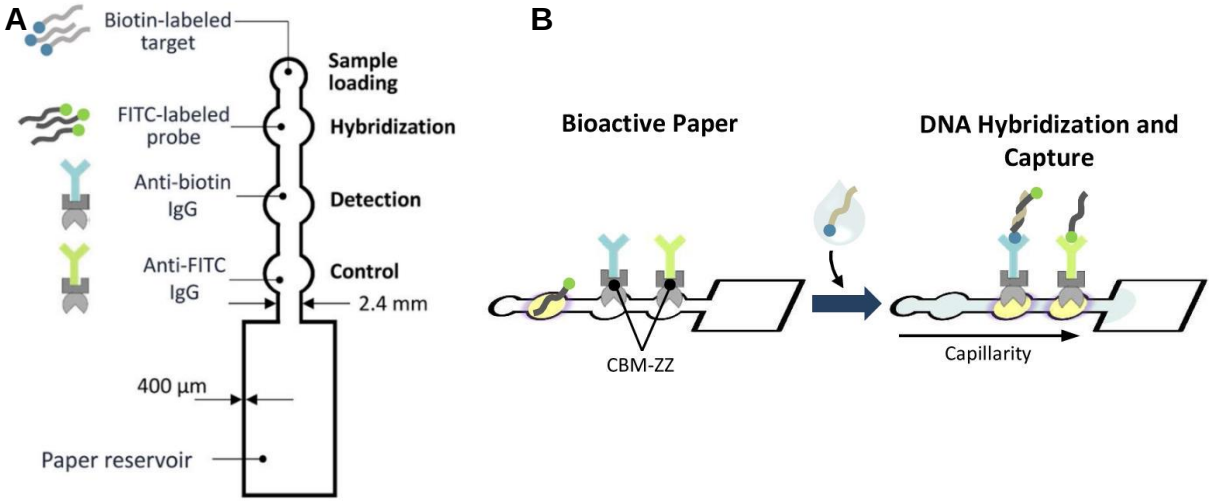

Figure 8: Layout of the DNA capture system described by Rosa et al.[48]A: Representation of the wax-printed µPAD and identification of each spot of interest, namely sample loading, where the biotin-labeled target is applied; hybridization, where the fluorescein-labeled probe is deposited; detection, where the CBM-ZZ-anti-biotin IgG conjugate is located; control, where the CBM-ZZ-anti-FITC IgG conjugate is located. B: Overall representation of the working system, before and after sample loading.

1.4.3. Electrochemical detection

µPADs capable of electrochemical detection (ePADs) are also able to select and sensitively measure several biomarkers. Glucose was successfully detected in whole blood samples by using a reusable, external screen-printed carbon electrode (SPCE) modified with Prussian Blue pigment, which has a mediator role. The device accurately separates the glucose-containing blood plasma from the whole blood and leads it into a detection region where glucose reacts with glucose oxidase. The resulting hydrogen peroxide can then be measured electrochemically using amperometry[53]. Electrochemical detection has also been shown to detect DNA in the low nanomolar range using conformational switching of an aptamer labelled with methylene blue upon binding with the analyte (Figure 9). This switch results in a location change of methylene blue away from a gold electroplated SPCE, which turns the signal “off”. The conformational change can be detected using either alternating current voltammetry or square wave voltammetry[54].

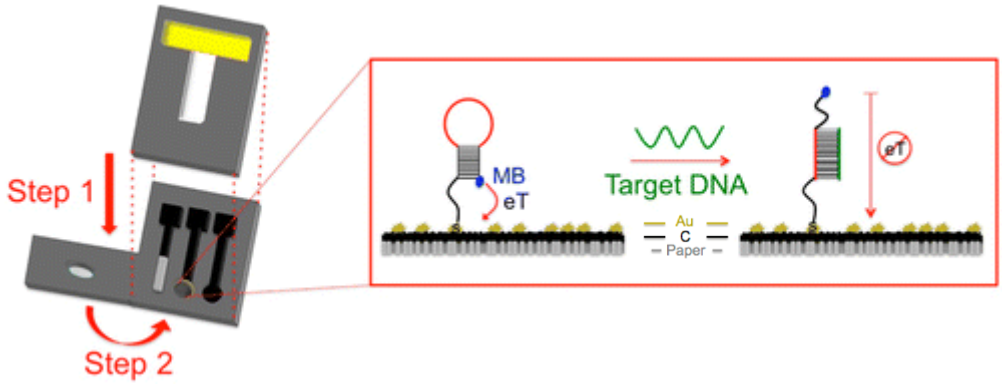

Figure 9: Layout of the DNA detection system designed by Cunningham et al.[54] Binding of the target DNA triggers conformational switching of an aptamer, which moves the electrochemical label further away from the electrode, resulting in a change in faradaic current.

In devices that detect the target analyte electrochemically, the inclusion of nanoparticles in the assays might bring several advantages. Their small size, from 1 to 100 nm, and high surface area confers them unique chemical, physical and electrical properties that should be beneficial for the design of reliable POC devices and assays.

1.2.2.1. Carbon nanomaterials

The use of carbon nanomaterials such as carbon nanotubes (CNTs) and graphene in POC tests has been under consideration for analysis of several biological analytes[55]. CNTs are used as transducers, due to their high sensitivity, specificity, speed of analysis, low cost and ease of use[28]. The use of single-walled carbon nanotubes in developing accurate and sensitive biosensors has been shown by Shen et al.[56]. These authors developed a paper-based chemiresistive biosensor that changes its electrical resistance in response to alterations in the nearby chemical environment. Through label-free immunosensing, this sensor was able to detect human serum albumin with a limit of detection of 1 pM. Graphene can also be inserted in paper-based electrochemical immune-devices successfully. Wu et al[57]. devised a µPAD that took advantage of the horseradish peroxidase–*O*-phenylenediamine–H_2O_2 electrochemical detection system, that was aided by the introduction of graphene, which modified the immune-device surface, accelerating the electron transfer. The graphene, together with silica nanoparticles, used as a tracing tag to label the signal antibodies, combined as a signal amplification strategy, allowing a successful multiplexed measurement of cancer biomarkers. An approach combining both carbon nanomaterials has been designed as a 3D ePAD cell culture device. By using carbon-paper electrodes modified with CNTs, graphene oxide and manganese oxide aerogel, this system could accurately detect hydrogen peroxide[58].

1.2.2.2. Gold nanoparticles

Out of all the nanoparticles made of metals, gold nanoparticles (AuNPs) are the most preferred for labelling, due to their excellent biocompatibility, good stability, easy functionalization with biomolecules and appropriate optoelectronic properties (e.g. surface plasmon resonance and surface enhanced Raman scattering) that can be adjusted by their size, shape and surrounding chemical environment[28]. The possible shapes for AuNPs include nanospheres, hollow spheres, nanorods, nanotriangles and

nanorings. These nanoparticles are usually synthesized by colloidal or liquid chemical synthesis by reducing a chloroauric acid ($HAuCl_4^{-1}$) solution in water. When the reducing agent is added and the solution is stirred, the Au^{3+} ions are reduced to Au^0 atoms, and the solution becomes increasingly saturated. Supersaturation results in precipitation of sub-nanometer gold particles while the remaining atoms in solution assemble onto the existing particles, thus producing size uniform particles[28]. The shape and size of AuNPs may be adjusted by tuning synthesis conditions such as the reducer used, temperature and introduction of different reaction steps.

Usage of AuNPs on biosensors via electrochemical detection has been thoroughly documented. On PADs, Ma et al. measured the differential pulse voltammetry in a device that detected simultaneously immunocaptured carcinoembryonic antigen and cancer antigen 125 on cellulose fibers previously coated with gold nanorods[59]. Cellulose fibers coated with gold and palladium alloy nanoparticles immunocaptured carcinoembryonic antigen and were immunotagged with gold-platinum nanoparticles bound with glucose oxidase and methylene blue, which resulted in the electrocatalytic detection of methylene blue and production of hydrogen peroxide when glucose is present[60]. An approach combining polyaniline coated and interconnected AuNPs immobilized on cellulose fibers and graphene oxide sheets as matrices with immobilized redox probes and antibodies successfully identified carcinoembryonic antigen and α-fetoprotein[61]. Prostate specific antigen has also been immunocaptured on nanostructured gold and manganese oxide coated cellulose fibers. The analyte was immunotagged with carbon nanospheres bound with glucose oxidase, reacting to glucose and producing the measurable hydrogen peroxide[62]. Culture of cancer cells in a 3D paper-based device containing AuNP-coated cellulose in contact with a SPCE allowed the capture of cancer cells on the electrode surface via aptamer. Said cells were labeled with aptamers conjugated with horseradish peroxidase, taking advantage of the aforementioned horseradish peroxidase–*O*-phenylenediamine–H_2O_2 electrochemical detection system[63].

1.4.4. Colorimetric detection

Colorimetric sensing, which is perhaps the simplest method of detection, relies on the production of color to confirm analyte presence. This detection is usually performed visually, making the method especially suitable for POC applications. The device developed by Demirel and Babur allowed colorimetric detection of glucose, albumin, uric acid, alkaline phosphatase and alanine aminotransferase through addition of reagents that would change color when in contact with the target analyte[64].

The use of nanomaterials might be of greater interest for colorimetric detection in cellulose and nitrocellulose-based paper platforms[21]. Nanoparticles tend to be more stable than organic reagents and have higher extinction coefficients, resulting in better sensitivity for target analytes[16]. The application of nanoparticles in immunoassays takes advantage of the high molar absorptivity of nanoparticles resulting in highly sensitive tests, with low detection limits.

1.2.2.3. Carbon nanomaterials

Biosensors with colorimetric detection have been successfully developed using carbon nanotubes by Liu et al[65]. The device they designed took advantage of the intrinsic peroxidase activity of $ZnFe_2O_4$-multiwalled carbon nanotubes, which are less labile than horseradish peroxidase. The platform of the sensor was prepared by depositing chitosan and porous gold onto filter paper, while entrapping the primary antibodies onto the layers. The secondary antibodies were assembled on the surface of the carbon nanotubes. Analyte detection was observed by a visible blue-green color change soon after primary and secondary antibody binding resulting from the oxidation of 3,3',5,5'-tetramethylbenzidine in the presence of peroxide hydroxide, catalyzed by the carbon nanotubes.

1.2.2.4. Magnetic nanoparticles

Due to the properties of magnetic nanoparticles, namely the ease of size control, low-cost production and easy manipulation with a magnetic field, they have been considered a good approach for biosensing[28]. These particles can be synthesized by different chemical and physical methods, with the most commonly used ones being iron oxides nanoparticles. They usually include a surface coating that make them hydrophilic, granting them better stability and preventing the agglomeration by magnetic attraction among particles and by van der Waals force. Different types of materials can be used to coat magnetic nanoparticles, from monomeric stabilizers like phosphates, to inorganic materials like gold and polymers like PEG[28]. For colorimetric detection purposes, several nitrocellulose-based sensors using magnetic nanoparticles have been devised. Among them are immunoassays for detection of Hepatitis B Surface Antigen, which employed carboxyl-modified magnetite nanoparticles[66], for quantitative measurements of Prostate Specific Antigen, which used a Resonant Coil Magnetometer to quantify paramagnetic particles[67], and for detection and quantification of tumor marker carbohydrate antigen 72-4, based on the use of superparamagnetic nanoparticles, which were quantified using a magnetic assay reader[68].

1.2.2.5. Gold nanoparticles

The employment of AuNPs in colorimetric paper assays gives rise to a simple and highly sensitive detection method[69]. Although at naked eye POC AuNP-based tests might merely give a qualitative analysis of the target analyte, image analysis software makes quantitative analysis possible.

Innumerable POC tests have been developed using AuNPs, aimed at detecting a whole array of analytes. As an example, dengue-specific immunoglobulins have been detected in salivary fluid using a stacking flow immunoassay and AuNPs as detection agents[70]. D-dimer has been successfully detected using a µPAD-based immunoassay. A mouse anti D-dimer antibody and a goat anti-mouse antibody are adsorbed in the test and control spots, respectively. AuNPs were functionalized with a different mouse anti D-dimer antibody and mixed with D-dimer-containing samples. After depositing the sample in the application spot and washing several times, a positive assay results in two red spots: one in the test zone, where the anti D-dimer would have recognized the D-dimer, which was itself bound to the antibodies in the AuNPs; and in the control zone, where an anti-mouse antibody would have recognized

the mouse antibody conjugated to the AuNPs[71]. For nucleic acid detection, several different approaches have been successful. Gao et al immobilized a DNA capture probe on a nitrocellulose membrane and the recognition DNA probe and horseradish peroxidase (for signal amplification) on the surface of AuNPs simultaneously, in order to detect microRNA[72]. Another sensor has been developed based on isothermal strand-displacement polymerase reaction and AuNPs to visually detect AuNPs with a detection limit of 0.01 fM[73]. Hu et al devised a strategy based on separation of DNA-functionalized AuNP aggregates throughout a nitrocellulose membrane, which would bind to the biotinylated DNA probes in the test and control zones, immobilized by streptavidin[74]. A paper-based tuberculosis diagnostic device using AuNPs has also been built, in which AuNPs modified with single-stranded DNA (ssDNA) hybridized with complementary double-stranded DNA (dsDNA) from tuberculosis-positive patients[75]. Hybridization caused a red to blue color change, whose intensity would be measured by an image analysis software. This color change stems from a property of the AuNPs. When AuNPs aggregate, the decrease of interparticle distance between them induces surface plasmon coupling, causing a red shift of the absorbance wavelength from 520 to 650 nm and a colloid color change from red to blue[76].

Immunoassay strategies involving AuNPs and CBMs have already been developed. The interaction of biotinylated AuNPs with ZZ-CBM3:anti-biotin IgG complexes immobilized in cellulose (paper and microparticles) shows that this system can be utilized in straightforward paper/cellulose-based tests[77]. The employment of this system has already been shown in cellulose microparticles for the detection of DNA strands[49]. The ZZ-CBM3:anti-biotin IgG supramolecular complex is assembled and added to an aqueous suspension of cellulose microparticles, where the CBM adsorbs. Addition of a biotinylated DNA strand and AuNPs conjugated with its complementary strand results in a change of color of the microparticles from white to red after microparticle deposition, as well as color depletion from the liquid. However, if the target is non-complementary to the strand conjugated with the AuNPs, the microparticles remain white and the liquid red.

2. Objectives

This work aims to develop tests for POC applications based on colorimetric detection with AuNPs and a new CBM3-based construct: CBM3-C. This construct contains an N-terminal hexa-histidine (His_6) tag and a C-terminal cysteine (Figure 10).

CBM3-C – *184 aa, 20.2 kDa*

MGSSHHHHHHSSGPQQGLRANTPVSGNLKVEFYNSNPSDTTNSINPQFKVTNTGSSAIDLSKLTL
RYYYTVDGQKDQTFWCDHAAIIGSNGSYNGITSNVKGTFVKMSSSTNNADTYLEISFTGGTLEPGAHV
QIQGRFAKNDWSNYTQSNDYSFKSASQFVEWDQVTAYLNGVLVWGKEPGGC

Figure 10: Amino acid sequence of the recombinant protein CBM3-C. Blue – hexa-histidine tag; Green – CBM3 from *Clostridium thermocellum*; Red – linker. The residues involved in the binding of CBM3 to cellulose are underlined and the cysteine residues are doubly underlined.

In this work, two applications will be developed based on CBM3-C to detect i) DNA strands and ii) protease activity. The first PAD will be used for detection of DNA strands. The recognition strategy will be based on the work developed by Rosa et al[48,49], who relied on conjugates of a ZZ-CBM fusion with an anti-biotin antibody to capture biotin-labeled DNA strands. However, the goal here is to avoid the use of an antibody by developing conjugates of CBM3-C with oligonucleotides strands to facilitate the anchoring of DNA probes on cellulose matrixes. The His_6 tag and the C-terminal thiol present in the cysteine of CBM3-C will be explored to directly link capture DNA strands to the CBM. This can be done on one hand by resorting to a non-covalent approach where a nitrilotriacetic acid (NTA)-modified ssDNA is used to establish a metallic complex with nickel ions together with the histidine in the N-terminal tag (Figure 11A). Alternatively, the CBM3-C can be covalently coupled to the capture DNA strand by using the heterobifunctional amine-to-sulfhydryl crosslinker sulfosuccinimidyl 4-[*N*-maleimidomethyl]cyclohexane-1-carboxylate (sSMCC), which connects amino-modified ssDNA to the C-terminal thiol of CBM3-C (Figure 11B). Detection of hybridization is signaled in both cases by the AuNPs conjugated with the complementary DNA strand (Figure 11).

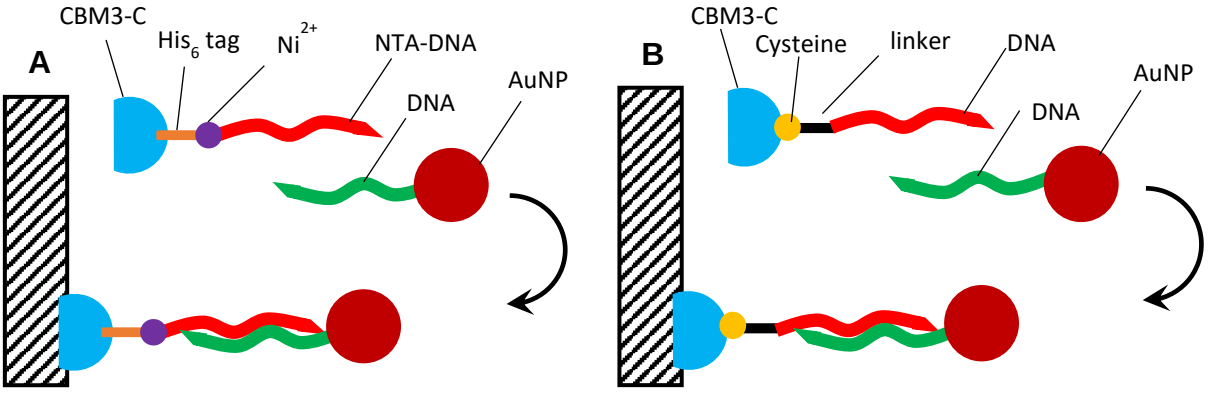

Figure 11: Schematic representation of the two approaches used to develop DNA paper-based DNA detection system. A: Non-covalent binding of DNA to CBM3-C. An NTA-modified DNA capture strand creates a complex with Ni^{2+} in which two coordination spots bind two histidines in the His_6 tag. Signal detection is achieved by AuNPs conjugated with the complementary DNA strand. **B**: Covalent binding of DNA to CBM3-C. The heterobifunctional linker sSMCC allows binding of amino-modified DNA capture strand to the thiol of the C-terminal cysteine. Detection is achieved as in **A**.

The second application is focused on the detection of proteolytic activity. Here I will take advantage of the high affinity of gold to thiol moieties such as the one present at the C-terminal of CBM3-C. The strategy involves a first incubation of the CBM3-C construct with a target protease (the non-specific protease trypsin is used here as a proof-of-concept) for a certain amount of time, and then addition of AuNPs and cellulose micro- or nanoparticles. The extent of proteolytic cleavage of the CBM3-C can then be ascertained by measuring the amount of AuNPs that are present in the liquid after deposition of cellulose particles (Figure 12).

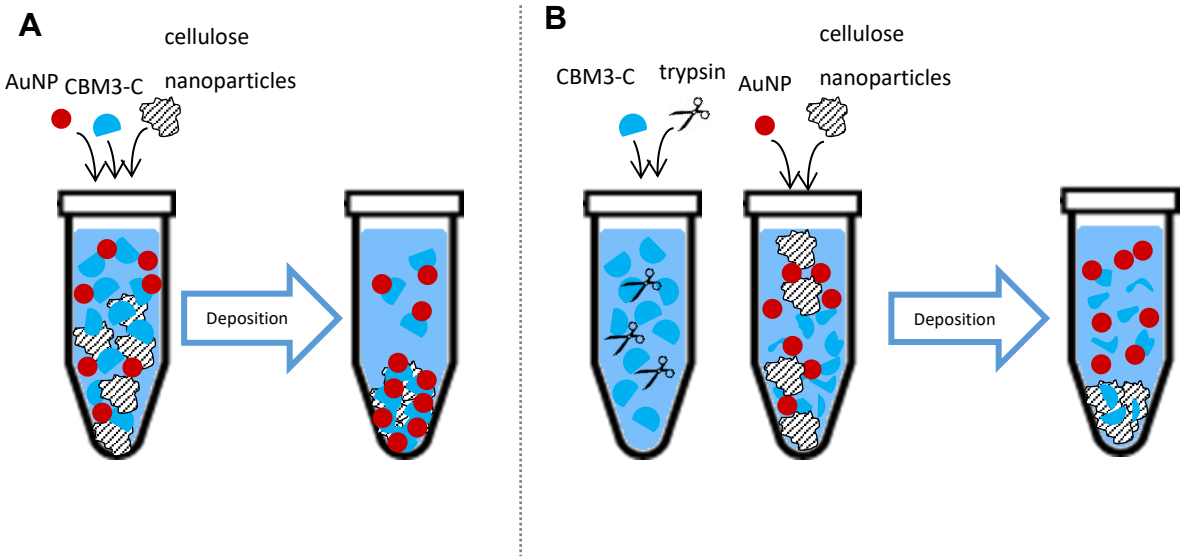

Figure 12: Schematic representation of the proposed CBM-based proteolytic activity sensor. A: Representation of the system without protease addition. The CBM moiety of the CBM3-C construct interacts with cellulose nanoparticles and the available thiol moieties interact with AuNPs. Deposition of cellulose pulls down the CBM bound AuNPs, leading to a decrease of AuNP concentration in the supernatant. **B**: Representation of the system when a protease is added. Pre-incubation of CBM with a protease (e.g., trypsin) leads to CBM proteolysis. Thus, the cellulose-binding and gold-binding moieties will no longer be in the same continuous sequence of amino acid residues. Some cleaved CBMs might still retain cellulose adsorption ability, while some may still bind gold, but after deposition of cellulose, the decrease of AuNP concentration in the supernatant should be lower than in the absence of protease.

3. Materials and methods

3.1. Device fabrication

3.1.1. Paper type

For development of the µPAD, Whatman no. 1 chromatography paper, 25 x 25 cm (catalog number: 3001-878; Whatman™, GE Healthcare©, Buckinghamshire, UK) was used. This paper is 0.18 mm thick and is hydrophilic, homogenous, biocompatible, inexpensive, readily available and does not require any pre-treatment before loading on the printer.

3.1.2. Wax printing

The patterns for the hydrophobic barriers of the µPAD were designed as black lines on a white background with the drawing software AutoCAD (Figure 13). Using the aforementioned Whatman no. 1 chromatography paper, these patterns were printed with a Xerox ColorQube 8570 color printer. This printer uses wax-based inks, dispensing melted wax on the paper surface, which immediately cools and solidifies, without any dispersion. The utilized ink contains hydrophobic carbamates, hydrocarbons and dyes with a melting point around 120 ºC.

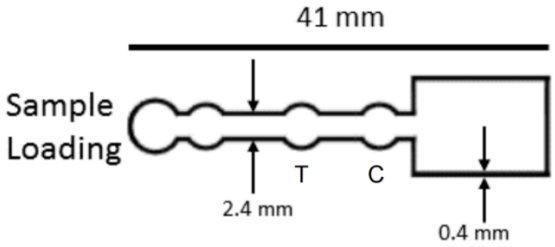

Figure 13: Design of the µPAD for detection of DNA hybridization. The areas labelled with T and C correspond to the Test and Control spots, respectively. The device is 41 mm long, with 2.4 mm wide channels and 0.4 mm thick wax lines. After wax melting and diffusion, the thickness of the wax barriers increases to 1 mm.

3.1.3. Wax melting

After printing, the paper was placed on a magnetic stirrer/heat plate (Labnet AccuPlate Hotplate Stirrer) with a temperature sensor, to melt the wax. The plate is pre-heated at 120 ºC for 10 minutes. The paper is then placed at this temperature for 2 minutes to allow complete wax melting and diffusion through the paper. After cooling at room temperature, the µPAD is ready to use.

3.1.4. Cellulose particles

For the assays performed in suspension in aqueous media, two types of cellulose particles were used: cellulose microparticles (Sigmacell 20, 20 µm) and cellulose nanoparticles (Innventia Generation 1 microfibrillated cellulose, Sweden)[78].

3.2. Oligonucleotides

All DNA oligonucleotides were purchased from STABVIDA. Excluding SA30 (derived from *Escherichia coli* 16S ribosomal RNA gene, with 10 adenines added at 5'), all oligonucleotides contain sequences present in the genome of the dengue virus (Table 2). Amino-serinol-modified oligonucleotides introduce primary amines to the DNA sequence.

Table 2: List of oligonucleotides used in this work, with corresponding sequence and modification

Oligo designation	Sequence	5' end modification
SA30	5'-AAAAAAAAAAGTAACGTCAATGAGCAAAGGTATTAACTT-3'	Thiol C6
DSH	5'-TTGAAGTCGAGGCCTGTTCTCGGAGAG-3'	Thiol C6
D3N	5'-CTCTCCGAGAACAGGCCTCGACTTCAA-3'	3x Amino-serinol
DS3	5'-CCTGTTCTCGGAGAG-3'	Thiol C6
DT3	5'-CTCTCCGAGAACAGGCCTCGACTTCAA-3'	None
D3N3	5'-TTGAAGTCGAGG-3'	3x Amino-serinol
DN3	5'-TTGAAGTCGAGG-3'	Amino-serinol

3.3. Gold nanoparticles (AuNP)

3.3.1. Synthesis of gold nanoparticles (AuNP)

The AuNPs used in this work were previously prepared according to the citrate reduction method published by Turkevich et al.[79] Twenty mL of 1 mM hydrogen tetrachloroaurate (III) ($HAuCl_4$, Fischer Scientific) solution were brought to a rolling boil in a stirring hot plate. At that point, 2 mL of 1 mL of trisodium citrate dihydrate ($Na_3C_6H_5O_7 \cdot 2H_2O$, Sigma) were quickly added. The solution is removed from the heat after it has turned deep red, approximately 10 minutes. This method is expected to generate AuNPs with a size of approximately 20 nm.

3.3.2. Functionalization of gold nanoparticles with thiol-DNA (AuNP-DNA)

In this work three different 5' thiolated DNA oligonucleotides were used to functionalize AuNPs. The SA30 oligo was used as a non-complementary probe and the dengue-specific DSH and DS3 oligos were used in two different systems, which will be thoroughly characterized later on.

3.3.2.1. Low pH method

Functionalization of AuNPs by pH challenging started with the addition of 10 µL of a solution of the reducing agent tris(2-carboxyethyl)phosphine (TCEP) 1 mM to 50 µL of DNA 10 µM, in order to break eventual disulfide bonds between oligonucleotides. Then, 100 µL of a 10 nM AuNP solution were added and allowed to incubate for 1 hour at room temperature. Next, 200 µL of a 10 mM trisodium citrate pH 3 solution were added, and the reaction mixture was incubated for 30 minutes at room temperature. The reaction mixture was then centrifuged at 6,000 g for 15 minutes, the supernatant was removed, and the

pellet washed with 10 mM trisodium citrate pH 6 solution. The conjugated AuNPs were washed three more times with this solution.

3.3.2.2. Salt aging

An AuNP-DNA solution was prepared by mixing the thiolated oligonucleotides with the AuNPs at a theoretical molar ratio of 1:200 (AuNP:DNA). In this mixture, the concentration of phosphate buffer was brought up to 10 mM and the concentration of sodium dodecyl sulfate (SDS) to 0.01% (w/v). The mixture was placed in an ultrasound bath for 10 seconds and then incubated in the dark for 30 minutes at room temperature. The NaCl concentration is then incremented to 50, 100, 200 and 300 mM using a solution of 10 mM phosphate buffer, pH 8, 1.5 M NaCl and 0.01% (w/v) SDS, with 10 seconds sonication in an ultrasound bath and 30 minutes incubation in the dark at room temperature following each increment. After the solution reaches 300 mM NaCl concentration, it is allowed to rest for ≥16 hours or overnight in the dark at room temperature. On the next day, the solution is centrifuged at 17,000g for 40 minutes at room temperature to separate AuNPs from unreacted reagents. Most of the supernatant is then removed. The pellet of AuNPs is washed twice with 10 mM phosphate buffer, pH 8, and once with 10 mM phosphate buffer, pH 8, 100 mM NaCl. After washing, the pellet is suspended in 10 mM phosphate buffer, pH 8, 100 mM NaCl.

3.3.2.3. Freezing-driven functionalization

This functionalization method was recently developed by Liu & Liu[80]. In this method, AuNPs and thiolated DNA are mixed at a theoretical molar ratio of 1:300 (100 µL of 10 nM AuNP solution and 3 µL of 100 µM DNA solution) and the concentration of sodium ions is brought up to 10 mM, with the addition of 2 µL of 500 mM sodium phosphate buffer. The mixture is then placed in a freezer at -20 ºC for at least 2 hours, up to overnight. The samples were then centrifuged at 17,000 g for 15 minutes at 20 ºC to remove unbound DNA and further washed with 5 mM HEPES buffer, pH 7.6 three times. After washing, the conjugate was dispersed in the HEPES buffer.

3.3.3. Characterization of gold nanoparticles

The AuNP suspensions were analyzed by UV-Visible spectroscopy. Spectra of the AuNPs were obtained between 480 and 600 nm. This range was chosen as approximately 20 nm-sized particles show a peak around 520 nm.

3.4. Characterization of the CBM3-C fusion protein

The recombinant protein CBM3-C (20.2 kDa) that was cloned in *E. coli* by NZYTech, Lda (Figure 12) results from the fusion of an N-terminal His_6tag and a C-terminal cysteine to a carbohydrate binding module from *Clostridium thermocellum*, CBM3 (see Annex I for further detail).

3.4.1. Binding to cellulose

Binding isotherms were determined experimentally to assess the ability of the CBM3-C construct to bind to cellulose. Experiments were performed by adding 1 mg of Sigmacell 20 microparticles to 100 µL

solutions of CBM3-C at different concentrations. In the preparation of the CBM3-C samples, Tris-Saline-Tween buffer (50 mM Tris, 150 mM NaCl, 0.05% (v/v) Tween 20, pH 7.6, TST) was used to dilute a concentrated sample of CBM3-C to the correct concentration. The protein-cellulose mixture was incubated for 10 minutes at room temperature and then centrifuged on a microcentrifuged (VWR MiniStar Silverline). The protein concentration in the supernatant was determined by the bicinchoninic acid (BCA) assay (Pierce BCA Protein Assay Kit, Thermo Scientific) and compared with the concentration in the starting solution, before particle addition. As controls, assays at individual protein concentrations were also performed with the fusion ZZ-CBM3.

3.4.2. Gold-thiol interactions

Assays to determine the interaction between AuNPs and the C-terminal thiol in CBM3-C (Figure 10) were performed using 200 µL of solutions containing different concentrations of CBM3-C and different amounts of cellulose microparticles or nanoparticles. To said solutions, 25 µL of a 10 nM suspension of AuNPs were added. After a brief (5 to 10 minutes) incubation, the cellulose particles were deposited by gentle centrifugation in a microcentrifuge and a 100 µL sample of the supernatant was removed to a 96-well microplate for spectral analysis, from 480 to 600 nm, in a microplate reader (Molecular Devices SpectraMax Plus 384). The remaining mixture was then subjected to a stronger centrifugation (10,000 g, 15 minutes) in order to deposit the remaining AuNPs present in the supernatant. For comparison purposes, these tests were repeated at discrete concentrations using Bovine Serum Albumin (BSA) and CBM3-ZZ, as well as in the absence of protein.

Analogues of these tests were repeated using AuNPs functionalized with oligonucleotides (SA30 and DSH, Table 2) to check for AuNP displacement.

The gold-thiol interaction was also assayed by running tests on the designed µPAD (Figure 13). The devices were prepared first by depositing 1 µL of CBM3-C solution (5 pmol) on the test area and 1 µL TST buffer in the control area. Volumes of the CBM3-C solution and TST buffer were applied by sequential addition of 0.25 µL. Next, 20 µL of solution containing 0.1 pmol of AuNPs were added in the sample addition area. Recurrent additions of TST buffer (20 µL) were performed in order to push the AuNPs towards the test and control areas and prevent the device from drying. A control assay was performed with 30 pmol of BSA in the test spot. The gold-thiol interaction was also observed by depositing increasing amounts of BSA (7.5 pmol to 37.5 pmol) and CBM fusions (CBM-ZZ and CBM3-C, 1.25 pmol to 6.25 pmol) in a sheet of chromatographic paper. TST buffer was also applied in the same amount of applications as the proteins, for control purposes. This paper sheet was then soaked in a dilute solution of AuNPs for five minutes and dried at room temperature.

3.4.3. Establishment of metallic complex with NTA and His_6 tag

In order to assess the capability of CBM3-C to form metal-mediated complexes with NTA, 1 mg of cellulose microparticles in a 100 µL suspension was added to a 100 µL solution of CBM3-C 5 µM. Addition of either or both 0.5 µL cobalt(II) sulfate heptahydrate 5 mM (molar ratio of cobalt to CBM3-C of 5:1) and 50 µL of hydrogen peroxide 100 mM (final concentration of 20 mM) was performed. To this

mixture, 0.5 nmol of NTA-Atto 488 fluorophore (Sigma Aldrich) was added. After incubation for 1 hour, the cellulose microparticles were deposited by centrifugation in a microcentrifuge and the fluorescence of the supernatant was measured in a fluorometer (Horiba Jobin Yvon FluoroLog-3).

3.4.4. Analysis of CBM3-C secondary structure

The secondary structure of CBM3-C was analyzed by circular dichroism in an Applied Photophysics PiStar 180 spectrophotometer. The spectrum was measured from 185 nm to 250 nm, using a 1 nm step size and a bandwidth of 8 nm. Spectrum analysis was performed using the BeStSel software[81].

3.5. Scanning electron microscopy

The chromatography paper used for design of the µPAD was observed by SEM using a Hitachi S-2400 Scanning Electron Microscope. The surface of cellulose micro- and nanoparticles modified with CBM3-C after contact with AuNPs, as well as unmodified cellulose particles were observed using a JEOL JSM7001F Field Emission Gun Scanning Electron Microscope. Prior to analysis, samples were coated with an Au/Pd layer using a Polaron E5100 coating system (Quorum Technologies).

3.6. Development of CBM3-C:DNA conjugates

3.6.1. Non-covalent approach: conjugation via His_6 tag

3.6.1.1. Synthesis of NTA-modified DNA

The method for linking the CBM3-C to DNA through nickel interactions was an adaptation of the method described by Goodman et al[82]. Oligonucleotides modified with three amine modifications (D3N and D3N3, Table 2) were dissolved in phosphate buffer (100 mM sodium phosphate, 100 mM NaCl, pH 7.3) to a final concentration of 100 µM. To 50 µL of this solution, 12.5 µL of freshly dissolved 100 mM 3,3'-dithiobis(sulfosuccinimidyl propionate) (DTSSP, ThermoFisher) were added. Following 1-hour incubation at room temperature, excess DTSSP was removed by using a size-exclusion spin column previously washed with phosphate buffer. For this and subsequent washings, Bio-Rad Micro Bio-Spin 6 columns were used for sample volumes up to 100 µL, while GE Healthcare PD SpinTrap G-25 columns were employed for larger volumes. 10% (v/v) of TCEP (Sigma Aldrich) 100 mM were then added, and the mixture left to incubate for 15 minutes. Finally, 10% (v/v) of NTA-maleimide (AAT Bioquest) 50 mg/mL (121 mM) dissolved in DMSO were added and excess NTA-maleimide was removed by transferring the sample into phosphate buffer with a spin column after 1-hour incubation at room temperature. The samples were stored at -20 ºC.

3.6.1.2. Analysis of synthesized oligonucleotides

TrisNTA-modified oligos can be separated from bis-, mono- and non-modified oligos by polyacrylamide gel electrophoresis (PAGE). In order to accurately resolve these oligos, samples were run on a two-layered, high-percentage, 7 M urea-containing denaturing gel. Resolving gel: 2.6 mL Tris 3 M pH 8.8, 8.41 g urea, 11 mL acrylamide/bis-acrylamide (19:1, 40%), 6.29 mL milli-Q H_2O, 10 µL

tetramethylethylenediamine (TEMED), 100 µL ammonium persulfate (APS) 20% (w/v). Stacking gel: 625 µL Tris 1 M pH 6.8, 2.1 g urea, 625 µL acrylamide/bis-acrylamide (19:1, 40%), 3.72 mL milli-Q H_2O, 5 µL TEMED, 25 µL APS 20% (w/v). Loading buffer: 94 µL Tris 1 M pH 6.8, 0.48 g urea, 63 µL 1% bromophenol blue, brought up to 1 mL with milli-Q H_2O. Running buffer: 2.5 mM Tris, 0.19 M glycine. Gels were cast without a well comb. Samples were combined 1:1 (v/v) with the loading buffer and heated to 95 ºC for 5 minutes. Gels were run at 150 V for approximately 10 minutes while the sample was migrating through the stacking gel and then at 300 V. DNA was stained in a 0.4 µg/mL ethidium bromide and visualized in a Stratagene Eagle Eye II cabinet.

Separation of oligonucleotides was also possible by reverse-phase liquid chromatography (RPLC). A Tricorn 5/100 column (GE Healthcare) was packed with SOURCE 15 RPC resin (GE Healthcare) with a volume (CV) of 2 mL. The column was connected to an ÄKTA 10 Purifier LC System (GE Healthcare) and a *Frac*-920 fraction collector. Two buffers were used for separation of oligonucleotides: buffer A: 0.1 M triethylammonium acetate, 5% acetonitrile; buffer B: 0.1 M triethylammonium acetate, 70% acetonitrile. Buffer mixtures were pumped through the column at a rate of 0.5 mL/min according to the following order: 100% buffer A, 0% buffer B over 2 CV; buffer B concentration was raised to 13% over 1 CV; 87% buffer A, 13% buffer B over 8 CV; buffer B concentration was raised to 16% over 30 CV; buffer B concentration was raised to 100% over 1 CV. Sample collection was done in 1 mL fractions.

3.6.1.3. Conjugation of NTA-DNA with CBM

The non-separated NTA-modified oligonucleotides were diluted to 20 µM in TN buffer (10 mM Tris, 100 mM NaCl, pH 8). Conjugation was then performed in one step by adding $NiCl_2$ (Sigma Aldrich) in molar excess (15% to 100% excess were tested) and CBM, so that [CBM]/[DNA] ≈ ⅔. Conjugates were prepared with both CBM3-C and CBM64 (NZYTech). Samples were stored at -20 ºC.

3.6.2. Covalent approach: conjugation via C-terminal cysteine

3.6.2.1. Synthesis of maleimide-modified DNA

In order to introduce a maleimide moiety in the oligonucleotide, mono-aminated DNA (DN3) was dissolved in phosphate buffer (100 mM sodium phosphate, 100 mM NaCl, pH 7.3) to a final concentration of 100 µM. To 50 µL of DNA solution, sSMCC 10 mM was added in 50-fold molar excess. The reaction mixture was allowed to incubate for 30 minutes at room temperature, and the excess crosslinker was removed with a spin column equilibrated with phosphate buffer. Samples were stored at -20 ºC.

3.6.2.2. Conjugation of maleimide-DNA with CBM3-C

The modified oligonucleotides were then combined with CBM3-C, so that [CBM]/[DNA] ≈ ⅔. The mixture was incubated for 30 minutes up to overnight at room temperature. Samples were stored at -20 ºC.

3.6.3. Chromatographic analysis of CBM:DNA conjugates

Samples of the oligonucleotides, CBM protein and CBM::DNA conjugates were analyzed by size-exclusion liquid chromatography (SEC). The analyzed samples were previously diluted to give final concentrations of DNA and CBM of ≈ 3 μM and ≈ 2 μM, respectively. 100 μL of this solution was analyzed by SEC. SEC was performed on a Phenomenex BioSep-SEC-S3000 column connected to an ÄKTA 10 Purifier LC system (GE Healthcare). The mobile phase was TN buffer, run at a flow rate of 0.5 mL/min.

3.7. Capture systems for DNA recognition

Capture and detection of complementary DNA by the CBM:DNA conjugates was evaluated using the standard μPAD (Figure 13) and following the overall method used in assaying gold-thiol interactions (section 3.5.2).

3.7.1. 2-oligonucleotide system

One of the systems studied was based on two oligonucleotides and only CBM:DNA conjugates formed through non-covalent interactions were studied. In this system, the immobilized oligo (D3N) is fully complementary to the DNA probe on AuNP surface (DSH). The CBM:DNA conjugate was immobilized in the test area of the μPAD in 0.25 μL steps. CBM3-C:DNA and CBM64:DNA conjugates were tested. In the control area TST buffer was added in an equal number of 0.25 μL steps. Between each application of conjugate/buffer, the test and control areas were air dried at room temperature. In the second leftmost area of the μPAD 10 μL of the DNA-functionalized AuNP solution was added. Tests were run with DSH-functionalized AuNPs, while negative controls were run with AuNP carrying SA30, oligonucleotide, which is non-complementary to D3N. Immediately after, TST buffer was added in steps of 10 μL to the leftmost spot of the μPAD, in order to prevent drying before the AuNP completed the circuit of the μPAD. Application of TST was usually done 2 to 3 times per test. Later on, some tests were repeated in this manner, but with an increasing amount of CBM:DNA conjugate in the control spot.

3.7.2. 3-oligonucleotide system

The other system that was studied was comprised of three oligonucleotides. In this system, the DNA conjugated with the CBM (D3N3/DN3) is not complementary to the DNA in the AuNP surface (DS3), but both are complementary to a target strand of DNA (DT3). The conjugates tested in this system were all based on CBM3-C, but non-covalently and covalently linked conjugated were tested (using D3N3 and DN3 oligonucleotides, respectively). The method for detection using this system is analogous to the 2-oligonucleotide system. Differences are in the oligonucleotides used in conjugation with CBM and functionalization of AuNP, as well as in the first addition of TST, which is substituted by addition of 10 μL of a solution of 10 μM DT3 DNA.

3.7.3. Spot analysis

All μPADs mentioned above were digitalized using a Canon Pixma MG3500 series scanner. Images were processed using the public domain imaging processing software ImageJ (National Institutes of

Health). Images were converted to 8-bit grey scale, the colors were inverted and the mean and max grey intensities of the test region were measured.

3.8. Proteolytic activity sensor

The methodology behind the development of the CBM-based proteolytic activity sensor is similar to the one used to assay the binding of CBM3-C to AuNPs in solution (section 3.5.2). Firstly, 1 mg of cellulose nanoparticles was added to 50 µL of 10 nM AuNPs. Mixture was brought up to 250 µL with TST buffer and 50 µL trypsin from bovine pancreas (Sigma) was added so that the final concentration ranges from 10 nM to 1 µM. After a brief incubation and a centrifugation in a microcentrifuge for deposition of cellulose, the 150 µL of the supernatant were removed and added to a 96-well plate. The samples in this plate were measured in a plate reader, where their spectrum, between 480 and 600 nm, was taken.

After assaying the effect of trypsin concentration on the gold nanoparticles, 150 µL of CBM3-C were incubated with 50 µL of trypsin for different amounts of time (5 minutes up to 1 hour). After the established incubation time, 50 µL of cellulose nanoparticles (containing 1 mg of cellulose) and 50 µL of 10 nM AuNP solution. Initial CBM3-C and trypsin concentration were such so that final concentrations were 10 µM and 10 nM, respectively. After cellulose nanoparticle deposition, 150 µL of the supernatant were extracted to a 96-well plate and the spectra of the samples was taken in a plate reader.

4. Results and discussion

The aim of this work is to develop new PADs for POC applications based on colorimetric detection with AuNPs and a new CBM3-based construct: CBM3-C. In the first section (4.1) of this chapter, CBM3-C is characterized in terms of its ability to bind cellulose, interact with AuNPs and form complexes with metal ions via its His tag. Details about the secondary structure of the protein are also presented. Section 4.2 presents and describes SEM images of cellulose matrices that were modified with AuNPs by exploring the dual ability of CBM3-C to bind cellulose and gold. The formation of conjugates of CBM3-C and oligonucleotides and their use in µPADs to capture cDNA is described in sections 4.3 (conjugation via nickel complexation) and 4.4 (conjugation via covalent binding with terminal cysteine). The final section (4.5) describes the setting up of a system for detection of proteolytic activity that is based on the combination of CBM3-C and cellulose particles.

4.1. Characterization of the CBM3-C fusion protein

The CBM3-C construct was prepared by cloning a His_6 tag and a cysteine residue in the N-terminal and C-terminal of a family 3 CBM from *C. thermocellum*, respectively (see Figure 10 and Annex I for further details). This CBM3 was chosen as the basis for this construct because of its very good binding to cellulose[83]. Following production and purification (Annex I), the construct was tested in order to confirm that it retained the ability to bind to cellulose and that the other characteristics conferred by the His_6 and cysteine moieties were present.

4.1.1. Binding to cellulose

In order to evaluate the ability of the CBM3-C construct to bind to cellulose, an assay based on measuring protein concentration before and after contacting 100 µL solutions of CBM3-C with cellulose microparticles (1 mg of Sigmacell 20) was performed. If the construct's binding ability is retained, deposition of the cellulose microparticles was expected to pull-down CBM3-C molecules alongside, depleting the supernatant solution. By varying the initial concentration of CBM3-C, it was possible to plot a binding isotherm of the construct (Figure 14).

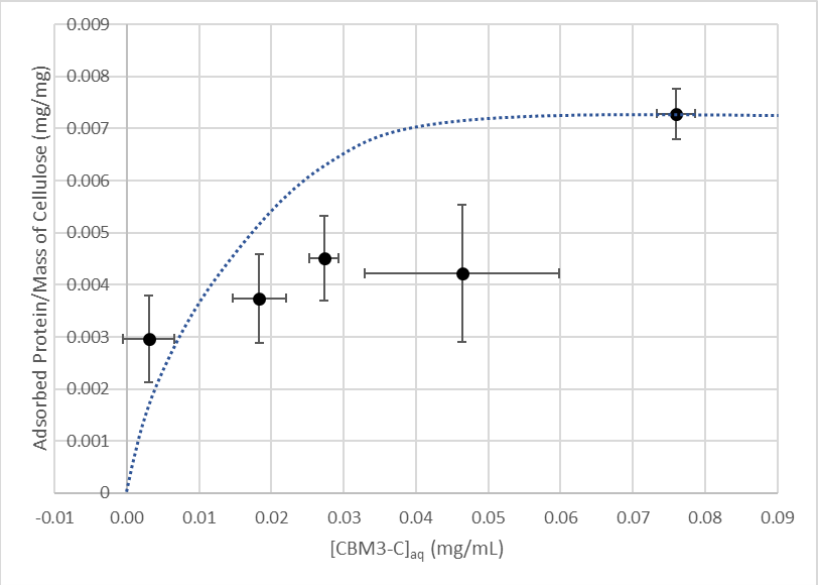

Figure 14: Binding of the CBM3-C construct to cellulose microparticles. The binding isotherm was determined by incubating 100 µL samples of CBM3-C with Sigmacell 20 microparticles (1 mg). The concentration of CBM3 in the liquid phase at equilibrium was determined using the BCA assay and the concentration of CBM3-C in the solid phase was calculated by performing a mass balance. Error bars were obtained from the standard deviations of three measurements. The dotted line represents the expected behavior of the binding isotherm curve.

The binding isotherm represented in Figure 14 did not follow the traditional logarithmic-like curve of the Langmuir model. Instead, a more linear model is shown. However, the error propagation of this data does not allow significant conclusions to be drawn. Experiments using higher concentrations of CBM might be necessary to understand if the curve eventually begins to plateau, as it is expected when the Langmuir model provides a good fit. Despite this, the experiments unambiguously confirm that the CBM3-C construct retains its cellulose-binding ability.

4.1.2. Gold-thiol interactions

To confirm the presence of the C-terminal cysteine in the CBM3-C construct, the strong interaction established between gold and sulfur was exploited. Since the CBM3-C construct was shown to be able to bind to cellulose, the assay described in section 4.1.1. was emulated, but using 200 µL of protein solution and adding 25 µL of a 10 nM suspension of AuNPs. Deposition of cellulose microparticles is now expected to pull-down CBM3-C and, consequently, AuNPs, thus lowering AuNP concentration in the supernatant (Figure 15).

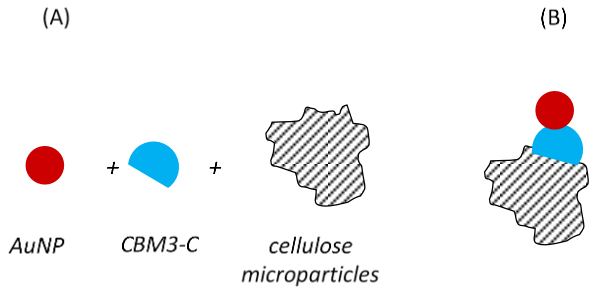

Figure 15: Schematic representation of the cellulose microparticle pull-down assays used to probe for gold-thiol interactions between AuNPs and CBM3-C. The molecular components are depicted schematically in blue (CBM3-C) and red (AuNP).

The distinct red color of AuNPs makes the monitoring of this assay very simple. If CBM3-C successfully binds AuNPs and cellulose, the pellet of cellulose microparticles formed after deposition by gentle centrifugation will display a red hue, while the supernatant will become colorless. On the other hand, if the protein does not bind either to cellulose or AuNPs, the pellet will display a white or light pink hue, while the supernatant retains all the AuNP characteristic red color (Figure 16, top row). If the samples are further subjected to a stronger centrifugation, unbound AuNPs will pellet into a single spot, whereas bound AuNPs will remain dispersed in the cellulose pellet (Figure 16, bottom row). Prior to this centrifugation the absorption spectrum of the supernatant was measured in order to more accurately quantify the binding of AuNP (Figure 17). This assay was also performed in the absence of any protein, with BSA and with the ZZ-CBM3 construct for comparison of results.

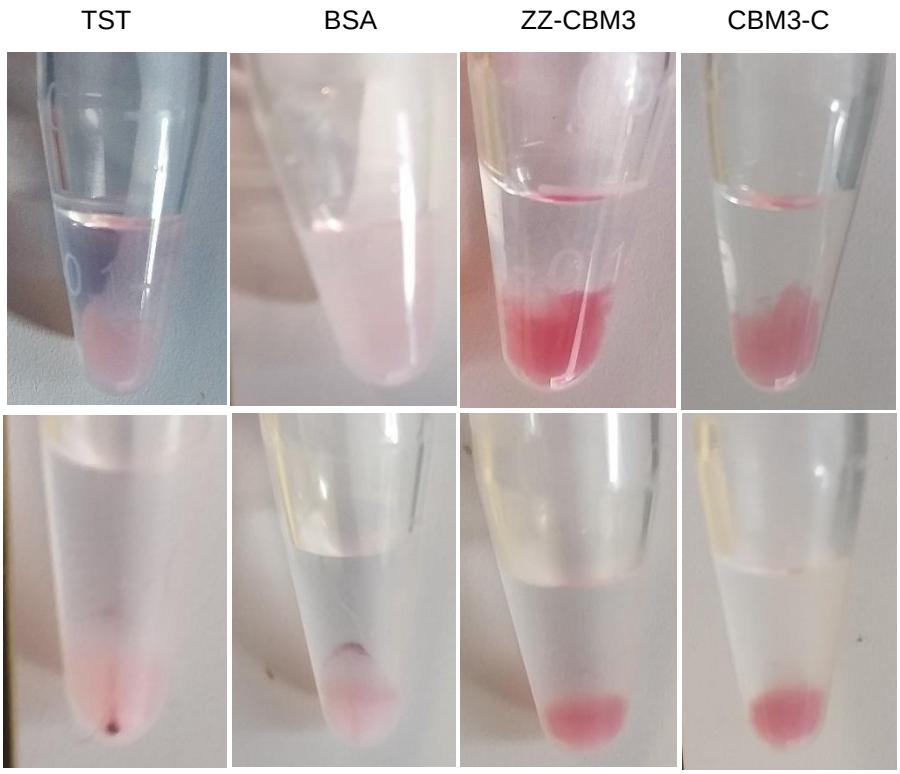

Figure 16: Probing for gold-thiol interactions between AuNPs and CBM3 constructs using pull-down assays with cellulose microparticles. Experiments were performed by mixing 20 µm cellulose particles, AuNPs and TST buffer (blank), BSA, ZZ-CBM3 and CBM3-C. **Top row**: Photographs of tubes after gentle centrifugation on a microcentrifuge. The AuNP presence in the cellulose sediment is most significant in the samples with CBM3 fusions. Control samples with TST and BSA display a light pink pellet and a redder supernatant, indicating a higher concentration of AuNPs in the supernatant. **Bottom row:** Photographs of tubes after centrifugation at 10,000 g for 15 minutes. The free AuNPs deposit as a single spot in the bottom or side of the tube, as observed in the samples with TST and BSA. The samples in which the AuNPs were bound to cellulose via CBM3 fusion displayed no significant changes after centrifugation. One mg Sigmacell cellulose, 200 µL of 5 µM protein solution and 25 µL of a 10 nM suspension of AuNPs were used in these assays.

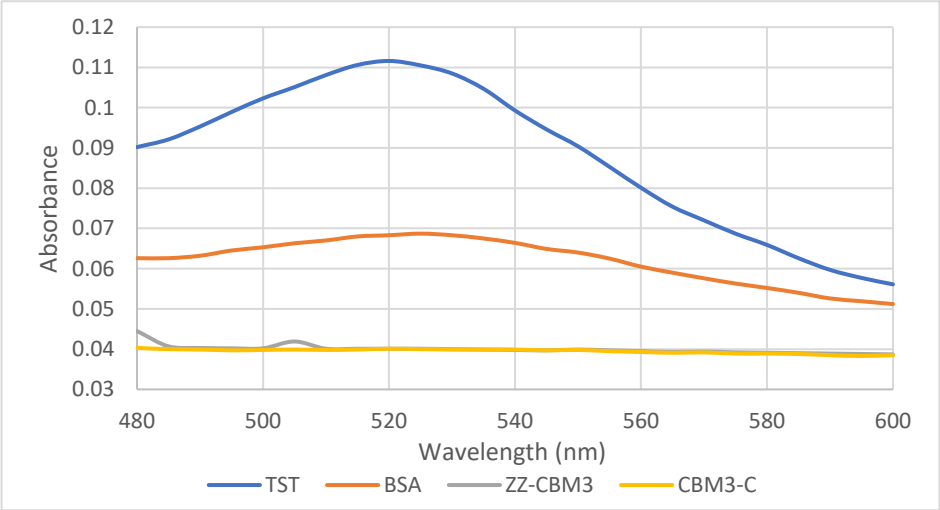

Figure 17: Spectrophotometric analysis of supernatants obtained after settling of cellulose microparticles by gentle centrifugation. Spectra are shown for supernatants obtained after performing pull-down assays with cellulose microparticles and AuNPs and i. TST, ii. BSA, iii. ZZ-CBM3 and iv. CBM3-C. One mg Sigmacell cellulose, 200 µL of 5 µM protein solution and 25 µL of a 10 nM suspension of AuNPs were used in these assays.

As expected, when the pull-down assays were performed in the absence of protein (the volume of protein solution was replaced by the same volume of TST buffer), no AuNPs were carried over when cellulose microparticles were deposited by gentle centrifugation. This presence of AuNPs in the supernatant is confirmed by the corresponding spectrum, which displays a characteristic absorption

peak around 526 nm. These suspended AuNPs could be sedimented by a stronger centrifugation, as evidenced by the presence of a red pellet within the midst of white microparticles (see bottom left photo in Figure 16). In the assays with BSA, the concentration of AuNPs in the supernatant was lower as can be inferred by the decrease in the intensity of the absorbance peak in the spectrum of the supernatant. This suggests that some AuNPs may have interacted with the several thiol groups present in BSA, and that BSA adhered non-specifically to cellulose. Nevertheless, a fraction of the AuNPs remained unbound, which could be deposited as a spot in the side of the tube after vigorous centrifugation.

The supernatants of the ZZ-CBM3 and CBM3-C constructs displayed similar spectra. CBM3 possesses a cysteine near a cellulose binding site (Figure 10), which is thought to be less stereochemically available than the linker-separated C-terminal cysteine. As there is no cysteine in the Z domains, there are one and two cysteines in the ZZ-CBM3 and CBM3-C fusions, respectively (see amino acid sequence of ZZ-CBM3 shown in Annex I). Thus, it was expected for the CBM3-C to capture more AuNPs. However, both were similarly effective in capturing AuNPs. Additionally, the binding of AuNP to the two constructs did not disrupt their ability to bind cellulose.

Additional pull-down assays were performed by changing some of the parameters. Firstly, the cellulose microparticles were replaced by microfibrillated cellulose nanoparticles. The absorption peaks at 526 nm of the supernatants obtained after gentle centrifugation are shown in Figure 18.

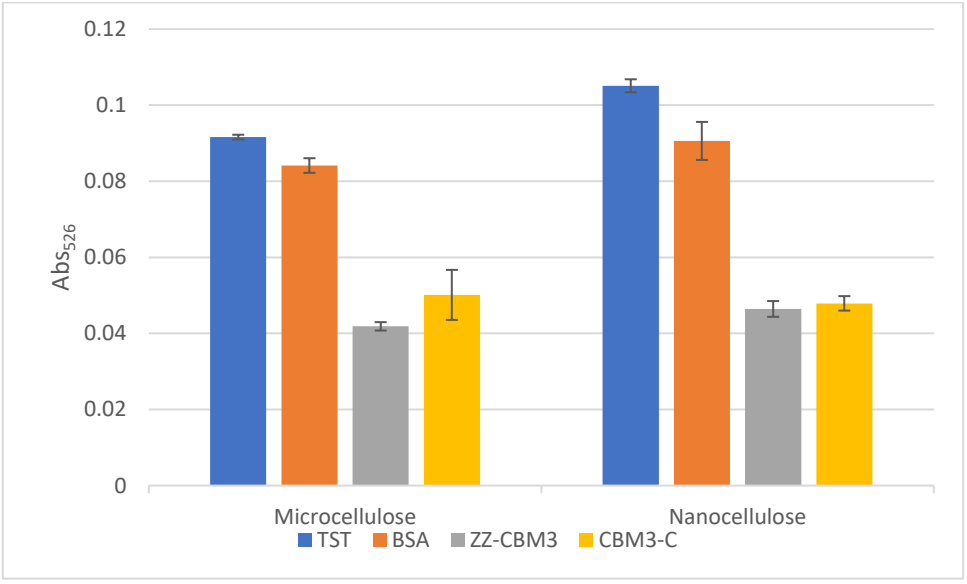

Figure 18: Effect of different type of cellulose particles on the ability of CBM3 fusions to bind cellulose and AuNPs. The peak absorption at 526 nm is shown for supernatants obtained after performing pull-down assays with cellulose particles and AuNPs and i. TST, ii. BSA, iii. ZZ-CBM3 and iv. CBM3-C. Data are reported as mean ± standard deviation (n=3). One mg of cellulose, 200 µL of 5 µM protein solution and 25 µL of a 10 nM suspension of AuNPs were used in these assays.

The data shows that the size and type of cellulose particles used had little impact in the outcome of the pull-down assays. Hence, from this point on, further tests were performed using the cellulose nanoparticles instead of the cellulose Sigmacell microparticles.

Secondly, the amount of cellulose particles used in the assays was varied. Instead of adding 1 mg of cellulose nanoparticles, only 0.25 mg were added (Figure 19A). Finally, the concentration of CBM3-C was modified, ranging from 2.5 to 10 µM (Figure 19B).

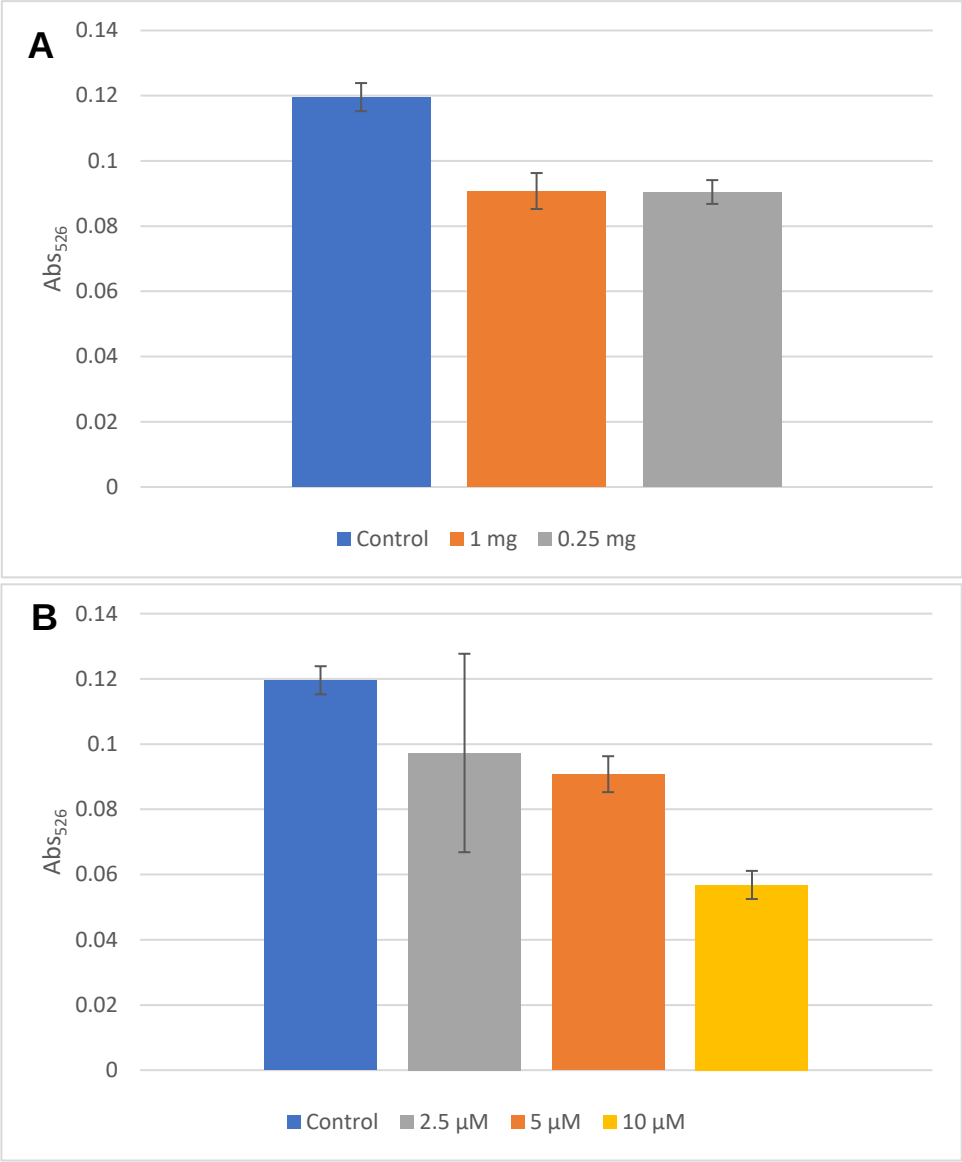

Figure 19: Effect of nanocellulose amount and CBM3-C concentration on the cellulose/AuNP pull-down assays used to probe for gold-thiol interactions. A – Effect of the cellulose amount. Tests were performed with either 1 mg or 0.25 mg of cellulose nanoparticles and with 200 µL of a 5 µM CBM3-C solution and 25 µL of a 10 nM suspension of AuNPs. **B** – Effect of the concentration of CBM3-C. Tests were performed with 2.5 µM, 5 µM or 10 µM of a CBM3-C solution and with 1 mg of nanocellulose and 25 µL of a 10 nM suspension of AuNPs. Controls were done in the absence of protein, with its volume replaced by TST buffer. Data are reported as mean ± standard deviation (n=3).

The reduction of cellulose quantity in the assay did not produce any changes in the absorption spectra of supernatants. In both cases, the presence of CBM3-C produced a similiar reduction in the intensity of the absorption peak at 526 nm (Figure 19A), which is consistent with the protein mediated pull-down of AuNPs by cellulose. This indicates that 0.25 mg of cellulose nanoparticles are sufficient to bind all the CBM3-C used in the assay (1 nmol). However, 1 mg of cellulose was still used in the following assays since it produces larger pellets that are easier to observe. Variation of the CBM3-C concentration in the assay displayed the expected results. Lower concentrations of CBM3-C resulted in more AuNPs in the supernatant, that diminished as CBM3-C concentration increased. This correlation supports the notion that the CBM3-C construct acts as a bifunction molecule that bridges AuNPs and cellulose.

A set of experiments was performed next in paralell using a CBM3 from *C. thermocellum* (1 cysteine), a CBM64 from *S. thermophila* (no cysteine) and the two CBM3 fusions CBM3-C (2 cysteines)

and ZZ-CBM3 (1 cysteine). The goal of this experiment was to clarify the role of cysteines in the binding of AuNPs. The results are shown in Figure 20.

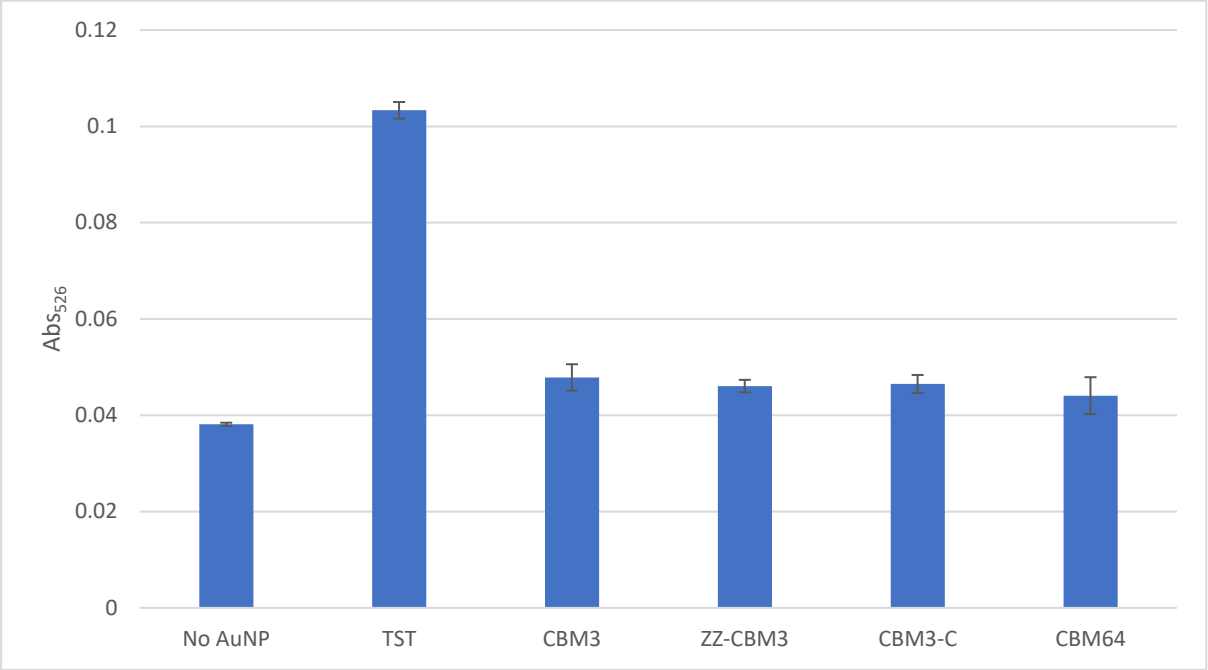

Figure 20: Probing for gold-thiol interactions between AuNPs and different CBM and CBM fusions using pull-down assays with cellulose microparticles. The peak absorption at 526 nm is shown for supernatants obtained after performing pull-down assays with cellulose particles, AuNPs and the indicated proteins. One mg of nanocellulose, 200 µL of 5 µM protein solution and 25 µL of a 10 nM suspension of AuNPs were used in these assays.. Data are reported as mean ± standard deviation (n=3).

As expected, supernatants obtained when pull down assays were performed with CBM3 displayed a peak at 526 nm of similar intensity to those obtained with ZZ-CBM3 and CBM3-C. These peaks were lower than the ones obtained in the control assay performed with TST, confirming that the three proteins mediate the pull-down of AuNPs by cellulose. However, CBM64 was also able to mediate the pull-down of AuNPs, as evidenced by the similar intensity of the absorption peak of the corresponding supernatant. This result was unexpected, since the CBM64 from *Spirochaeta thermophila* used here does not contain any cysteine in its amino acid sequence. A possible explanation is that AuNPs can still establish interactions with nitrogen atoms in the CBM64 protein, though weaker than gold-sulfur interactions[84].

In order to clarify this issue, similar assays were performed but using AuNPs functionalized with thiolated DNA strands via gold-sulfur interactions. The presence of this DNA coat should hinder the binding of cysteine-containing proteins, and hence the pull-down of AuNPs to cellulose. Nevertheless, since the gold-sulfur interaction is labile, cysteine containing proteins could displace the surface DNA[85], and thus promote the pull-down of some AuNPs to the cellulosic pellet. On the other hand, this displacement should not occur when using proteins with no cysteines like CBM64 – in this case the majority of AuNPs should maintain the integrity of their DNA coat and thus remain in solution.

As a first approach, citrate-capped AuNPs where functionalized with the 39-nucleotide long SA30 oligonucleotide (Table 2) using the low pH method[86]. The reaction is done at a low pH in order to overcome the kinetic barrier of DNA attachment, since both DNA and the citrate capping of AuNP are negatively charged[87]. The spectrum of these newly functionalized particles was measured and

compared with citrate-capped AuNPs (Figure 21). The functionalization of AuNPs with the SA30 DNA strand resulted in a broadening and redshift of the plasmon band, since the exchange of citrate for DNA strands on the particle's surface results in a local variation of the refractive index. However, when these functionalized AuNPs were put in contact with CBM3-C or CBM64 solutions, AuNP aggregation was observed as signaled by the change of color from red to blue/purple, which is characteristic of AuNP aggregation[88] (data not shown).

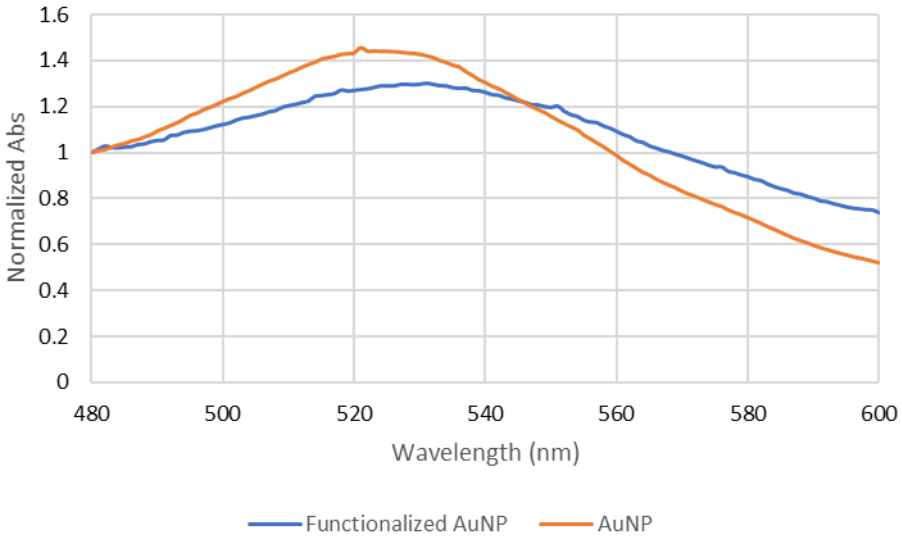

Figure 21: Spectra of AuNP and SA30-functionalized AuNP from 480 to 600 nm. Results are presented as normalized absorbance, to account for different concentrations of AuNP solutions. For normalization, all absorbance measures were divided by the absorbance at 480 nm of each corresponding sample.

Further attempts were pursued by modifying AuNPs with a different and smaller (27-nucleotides) oligonucleotide (DSH, Table 2) via a salt aging procedure. In this method, salt is introduced in the solution stepwise in order to overcome the long-ranged electrostatic repulsion between DNA and AuNPs. The stepwise addition of salt is done to retain the stability of AuNPs, which would otherwise aggregate if a high concentration of salt was immediately introduced[87]. Following the preparation of DSH-functionalized AuNP via salt aging, pull-down assays were performed using the CBM3, CBM3-C and CBM64 proteins (Figure 22).

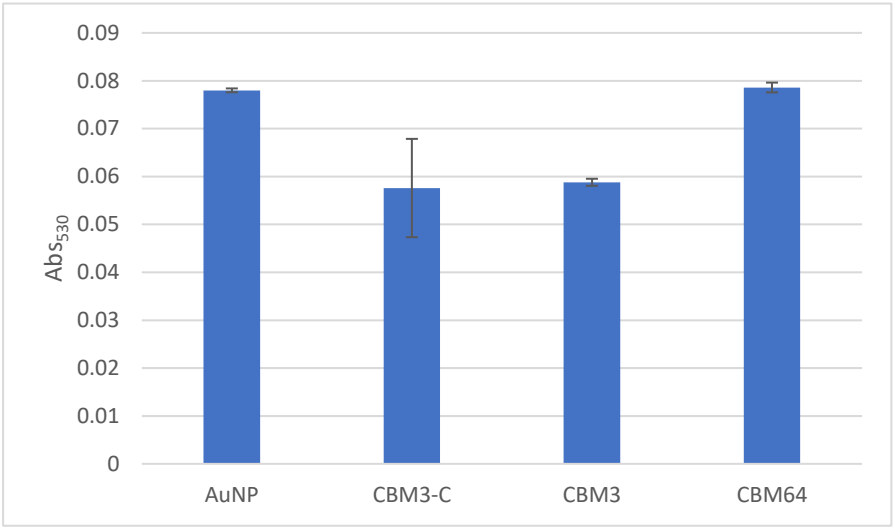

Figure 22: Peak (530 nm) absorbance of supernatants obtained after cellulose/AuNP pull-down assays using salt-aged DNA-functionalized AuNP. The absorbance was measured at 530 nm due to the redshift of the spectrum of functionalized DNA. One mg of nanocellulose, 200 µL of 5 µM protein solution and 25 µL of a 10 nM suspension of AuNPs were used in these assays. Data are reported as mean ± standard deviation (n=3).

With the new particles, the tests yielded the expected results. Displacement of AuNPs to settled cellulose occurred in tests performed with CBM3-C and CBM3, as observed by the decrease in the absorbance peak of the corresponding supernatants as compared to the control. In the test performed with CBM64, however, no displacement occurred, as the intensity of the absorbance at 530 nm is similar to that of a solution of DSH-functionalized AuNPs. Therefore, it is safe to assume that the previously observed interaction between citrate-capped AuNPs and CBM64 was unspecific (caused by nitrogen), while interaction with CBM3 and CBM3-C is mainly caused by the sulfur in the cysteines.

4.1.2.1. Paper-based assays

Gold-thiol interactions between CBM3 fusions and AuNPs were also studied using chromatographic paper by two different methods. The first method was performed using wax-printed µPADs (Figure 13) as described next. Two µPADs were prepared by depositing either 5 pmol CBM3-C (Figure 23A, bottom) or 30 pmol BSA (Figure 23A, top) in the test areas (marked T) of the devices. TST was applied to the control areas (marked C) of both PADs. Next, 20 µL of a solution containing 0.1 pmol of AuNPs were added to the sample addition area (marked S), followed by recurrent additions of TST buffer (20 µL) to push the AuNPs towards the test and control areas and prevent the device from drying.

In the second method, increasing amounts of BSA, ZZ-CBM3 and CBM3-C were deposited at discrete points in a rectangular piece of chromatographic paper, in a way that in each column the same volume of sample (0.25 to 1.25 µL) was applied. Controls were performed by adding a row in which only TST buffer was added. The chromatographic paper was then soaked in a dilute solution of AuNPs for a brief incubation and then air-dried (Figure 23B).

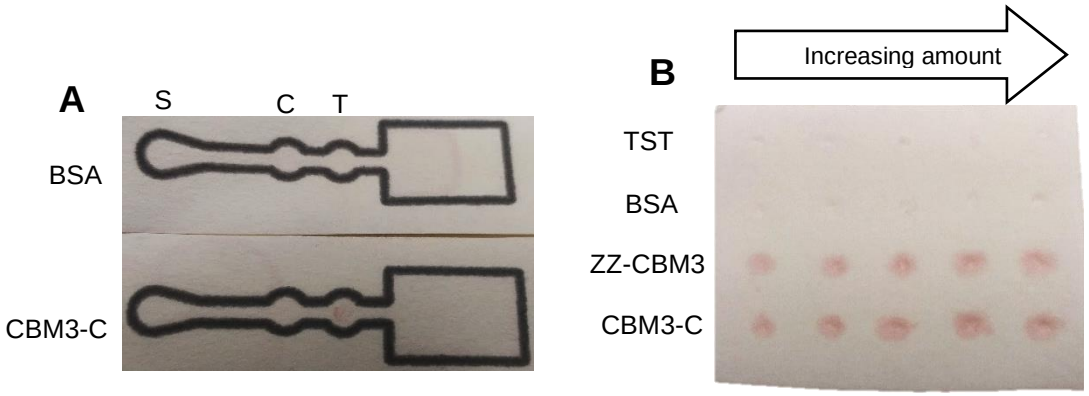

Figure 23: Probing for gold-thiol interactions between AuNPs and CBM3 constructs using paper-based capture assays. A - µPAD tests were performed with BSA (top) and CBM3-C (bottom). The sample addition (S), control (C) and test (T) areas are pinpointed on the upper µPAD. **B** – AuNP capture test performed with increasing volumes of TST, BSA, ZZ-CBM3 and CBM3-C. Amounts of BSA range from 7.5 pmol to 37.5 pmol (7.5 pmol increments), while amounts of CBM3 fusions range from 1.25 pmol to 6.25 pmol (1.25 pmol increments).

In Figure 23A it is possible to observe a red spot in the test area of the µPAD prepared with CBM3-C (bottom), which contrasts with the blank test area observed in the BSA µPAD (top). In the BSA case it is also apparent that most AuNPs flowed past the test area, as judged by the light red wave front that can be discerned halfway through the rectangular reservoir. Figure 23B confirm the ability of both ZZ-CBM3 and CBM3-C to bind and bridge AuNPs to paper, since there was no major difference in the intensity of the spots obtained. As expected, the spots prepared with TST buffer and BSA did not bind any AuNPs and the increasing amount of ZZ-CBM3 and CBM3-C resulted in an increased area of the AuNP spots.

4.1.3. Establishment of metallic complexes through the His_6 tag

The establishment of interactions between histidines and nickel is already well studied[89]. In fact, a significant number of immobilized metal affinity chromatography (IMAC) applications are based on these interactions. In many IMAC resins, nickel is immobilized by using the chelator NTA in such a way that passing His-tagged proteins will form a coordination compound with the nickel ion. As the CBM3-C fusion was successfully purified by IMAC with a resin containing nickel (further details in Annex I), this interaction is very much proven. In the following test, CBM3-C was assayed for its ability to form coordination compounds with another metal, cobalt. A study by Wegner and Spatz showed that complexes with Co^{3+} are more stable and inert than a Ni^{2+} complex with same coordination environments[90]. To form such complexes, a Co^{2+} complex is first formed, which is then oxidized with H_2O_2 to Co^{3+}, because the direct formation of complexes with trivalent cobalt is very slow.

To test the establishment of Co^{3+} complexes with CBM3-C an NTA-atto 488 fluorophore was used. Since this fluorophore was purchased in the form of a nickel complex, cobalt was added in molar excess to stimulate ligand exchange. CBM3-C (5 µM, 100 µL) was first immobilized in cellulose nanoparticles (1 mg, 100 µL) followed by the addition of cobalt(II) sulfate heptahydrate (5 mM, 0.5 µL), hydrogen peroxide (100 mM, 50 µL) and NTA-atto 488 (0.5 nmol), in that order, resulting in a final concentration of NTA-atto 488 of ~2 µM. After 1 h incubation, the mixture was subjected to gentle centrifugation to

promote cellulose nanoparticle deposition and the fluorescence of the supernatant was measured. The controls for this experiment are shown in Figure 24.

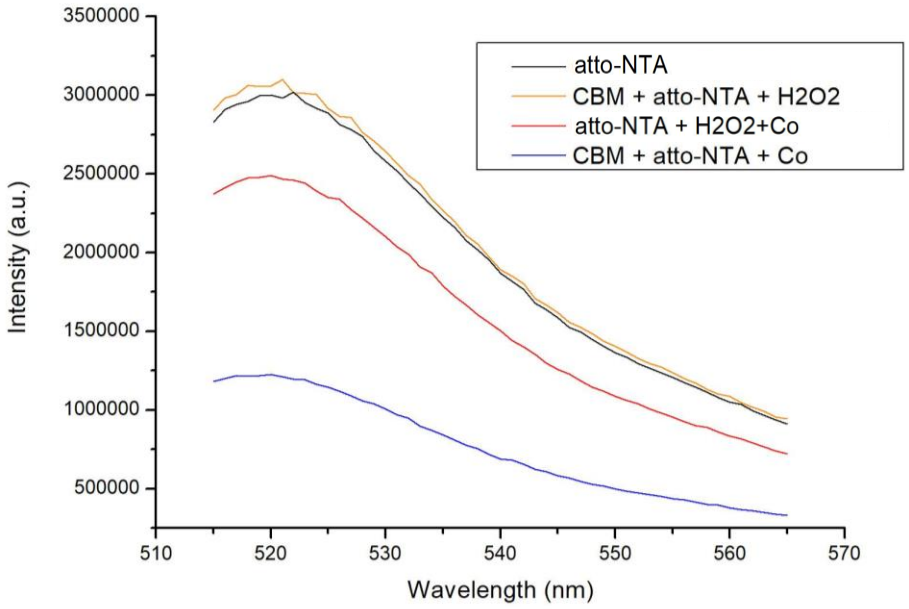

Figure 24: Study of the cobalt-mediated complexation of the fluorophore NTA-atto 488 with His tagged CBM3-C anchored on nanocellulose. The fluorescence spectra of supernatants obtained after sedimentation of nanocellulose are shown for tests performed under different conditions.

Preliminary tests were first performed, in which the fluorescence of the fluorophore alone (black spectrum) and in the presence of cobalt and hydrogen peroxide (red spectrum) was measured. Results show that the addition of cobalt and hydrogen peroxide causes a reduction in the fluorescence of the fluorophore. Right off the bat, this result indicates that the experiment would have to be adapted to overcome this loss of fluorescence, which probably results from the oxidation of the fluorophore.

An experiment was then performed without the addition of hydrogen peroxide (blue spectrum). The fluorophore was successful captured by the CBM3-C construct and pulled-down from solution by the nanocellulose, as observed by the significant reduction of fluorescence in the supernatant. From these results it is possible to conclude that divalent cobalt complexes between CBM3-C and NTA-atto 488 are most likely formed (although some interactions might still be mediated by residual nickel ions). Experiments performed without the addition of cobalt and with the addition of hydrogen peroxide, fluorescence (orange spectrum) produce results similar to those obtained with the NTA-atto 488 fluorophore alone (black spectrum). Thus, the incubation of CBM3-C with hydrogen peroxide resulted in no capture of fluorophore by the protein. In fact, some other tests in µPADs resulted in loss of AuNP signal when the CBM3-C was previously incubated with hydrogen peroxide and circular dichroism analysis showed that incubation with hydrogen peroxide resulted in loss of structure for CBM3-C (data not shown). Overall, it seems that hydrogen peroxide denatured the CBM3-C, preventing it from binding to the cellulose and interacting with the fluorophore.

4.1.4. Secondary structure analysis

The overall structure of the CBM3-C fusion protein was analyzed by circular dichroism analysis. By submitting the measured data to the BeStSel online software[81], it is possible to estimate the secondary structure content of CBM3-C. The secondary structure of CBM3 was also analyzed for comparison purposes (Figure 25).

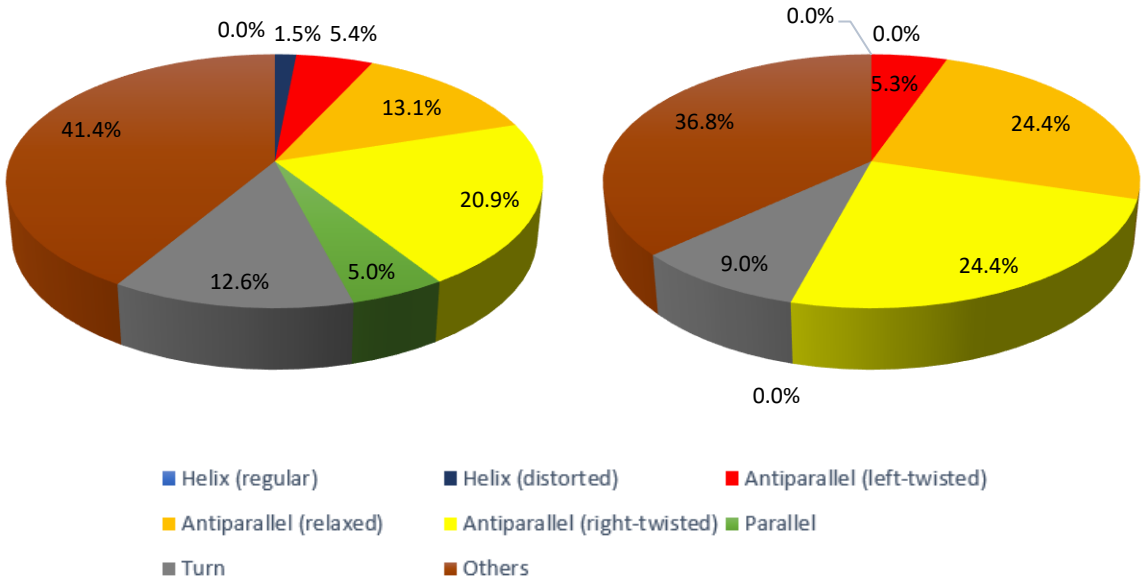

Figure 25: Secondary structure analysis of CBM3-C (left) and CBM3 from *Clostridium thermocellum* (right, PDB ID 1NBC)[42]. Data from CBM3-C obtained by circular dichroism and processed by the BeStSel software[81].

Although there are some differences between CBM3 and CBM3-C in what secondary structure is concerned, the prevalence of antiparallel structure is maintained in both proteins. The class, architecture, and topology of these proteins was also classified, according to the CATH Protein Structure Classification database[91], shown on Table 3.

Table 3: Classification of CBM3 and CBM3-C concerning class, architecture and topology, according to the CATH Protein Structure Classification database.

	CBM3	*CBM3-C*
Classification	Mainly Beta	Mainly Beta
Architecture	Sandwich	Sandwich
Topology	Immunoglobulin-like	Immunoglobulin-like

This analysis confirms the structure similarities between CBM3 and CBM3-C, as well as the classification of CBM3 into the first fold family of CBMs, which all form a β-sandwich (Table 3).

4.2. Scanning electron microscopy

To better observe how the CBM3-C binds AuNPs on different cellulosic supports, SEM analysis was performed. This analysis was also useful to perceive the architecture of each support. In this analysis, a focused beam of electrons scans the surface of a sample by interacting with its atoms, collecting information about the surface topography and composition of the sample. SEM analysis was performed on cellulose microparticles and nanoparticles, with and without CBM3-C and AuNPs bound to them. Figure 26 shows images of these samples at 30,000 x magnification. Images obtained at other magnifications are shown in Annex II.

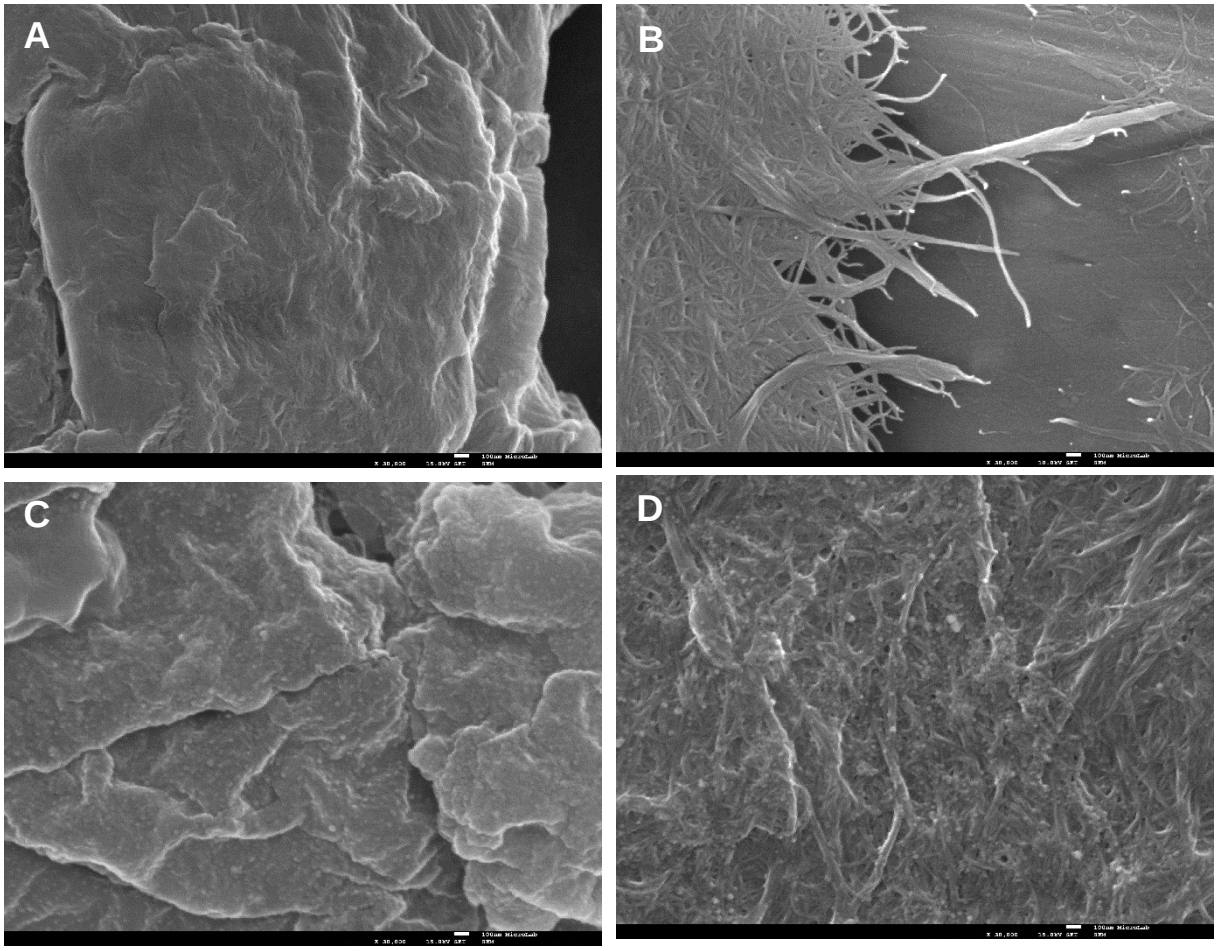

Figure 26: SEM images containing cellulose microparticles and nanoparticles (A and B), and AuNPs bound to these supports via CBM3-C (C and D), respectively. All images were obtained at 30,000x magnification with a SEI (Secondary Electron Imaging) detector (100 nm scale).

In Figure 26A, it is possible to observe part of one of the 20 µm cellulose microparticles. At other magnifications, individualized microparticles were observed that similarly presented a relatively smooth surface. When CBM3-C and AuNP were added to these particles, the surface became notably more rugged and granular, due the binding of AuNPs (Figure 26C). In the case of the microfibrillated cellulose nanoparticles, no individualized particles were observed at the different magnifications covered (see Figure 26B and Annex II). Instead, a network of interwoven cellulose microfibrils is observed (Figure 26B). Addition of CBM3-C and AuNP also turned the surface more granulated (Figure 26D), thus confirming the successful binding of CBM3-C and AuNP to both types of cellulosic surfaces.

4.3. DNA recognition system: non-covalent formation of CBM3-C:DNA conjugate

The DNA recognition biosensor envisaged calls for the immobilization of a capture oligonucleotide on a µPAD via the CBM3-C construct (Figure 11). CBM3-C:DNA conjugates can be formed by exploiting several chemistries. As a first approach, the formation of nickel complexes through the His_6 tag in CBM3-C was explored (Figure 11A). In order to do so, capture oligonucleotides were pre-modified with NTA moieties to enable them to establish interactions with nickel ions. While formation of complexes is still possible with a single NTA modification, three NTA modifications result in a stronger link between the oligonucleotide and CBM3-C. This nickel coordination complex will adopt an octahedral conformation, with six coordination spots. Four of these spots are occupied by three carboxylic oxygens and the nitrogen in the tertiary amine of NTA, while the remaining two spots by the organic nitrogen of the imidazole moiety of two histidines. As there are a total of six histidines in the histidine tag, modifying the DNA with three NTA moieties allows the establishment of three complexes, with all the histidines in the tag interacting with nickel ions.

4.3.1. Synthesis of trisNTA-modified oligonucleotides

The starting point for the synthesis of trisNTA-modified oligonucleotides was the D3N capture oligonucleotide (Table 1). This ssDNA contains three amino-serinol moieties at the 5´end, providing it with three primary amines, which can be readily modified. The process for this synthesis involves two crosslinkers, DTSSP and NTA-maleimide (Figure 27A), and a reducing agent, TCEP.

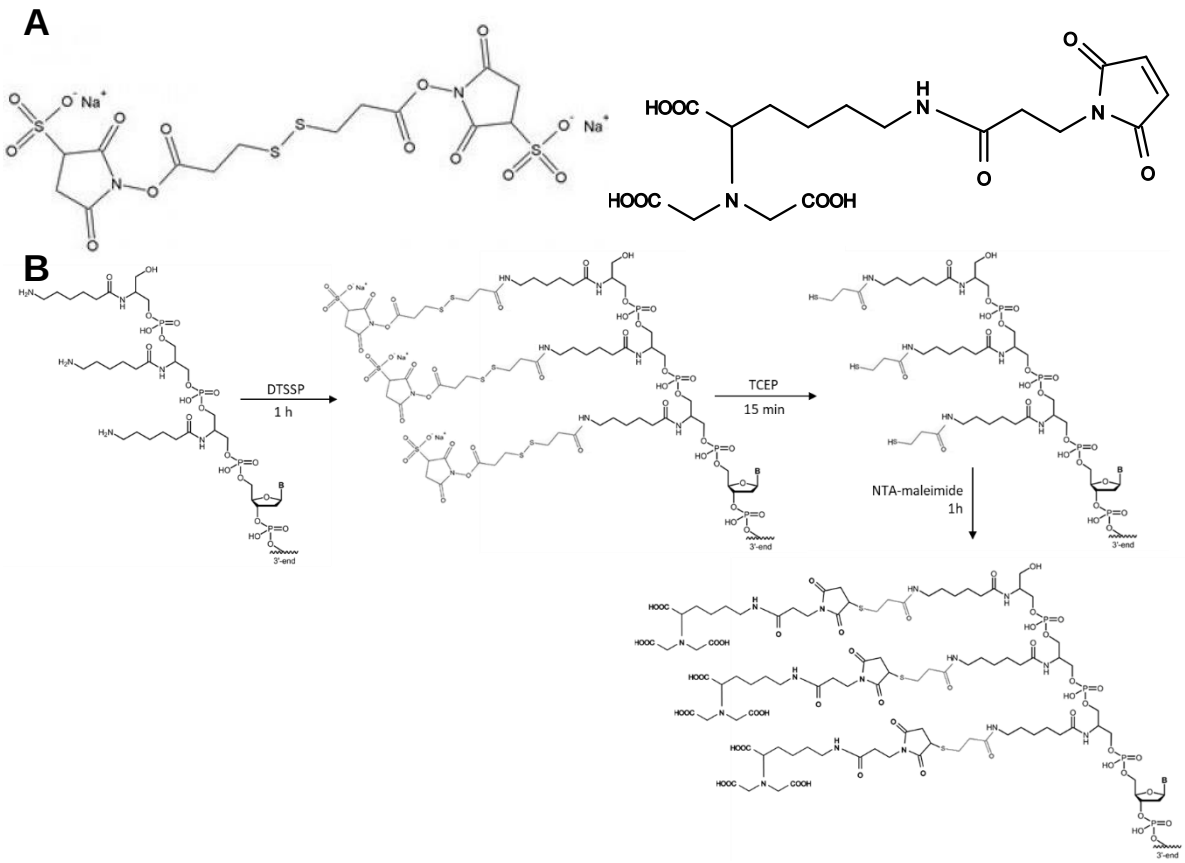

Figure 27: Chemical structures of the two crosslinkers employed in the synthesis of NTA-modified oligonucleotides (A) and the schematic representation of the reactions for synthesis of DNA oligonucleotides functionalized with three NTA groups (B). A: Left – DTSSP; Right – NTA-maleimide.

The first step in the synthesis involves the reaction of the oligonucleotide with the water-soluble crosslinker DTSSP (Figure 27A, left). This compound has amine-reactive *N*-hydroxysulfosuccinimide (sulfo-NHS) ester moieties at both ends that can form stable amide bonds with primary amines. The reaction, which must be done in a non-aminated buffer such as phosphate buffer, is allowed to proceed for one hour. As DTSSP molecules can react with amines through both ends, DNA dimers can be created if one molecule reacts with the primary amines on two different oligonucleotides. However, this is unraveled by the addition of TCEP, a chemical that cleaves the central disulfide bond of DTSSP. At this point, the D3N oligonucleotide should be modified with three thiol moieties at its 5´end (Figure 27B). Then, the addition of NTA-maleimide results in interaction of the maleimide moiety of the crosslinker with the thiol groups, resulting in trisNTA-modified oligonucleotides with a molecular weight that has increased by 1491 g/mol when compared with the original oligonucleotide (Figure 27B).

Samples of the reaction mixture were subjected to urea denaturing PAGE, in order to resolve the trisNTA-modified oligonucleotides from possible bis- or monoNTA-modified oligonucleotides. A section of the gel after staining with ethidium bromide is shown on Figure 28.

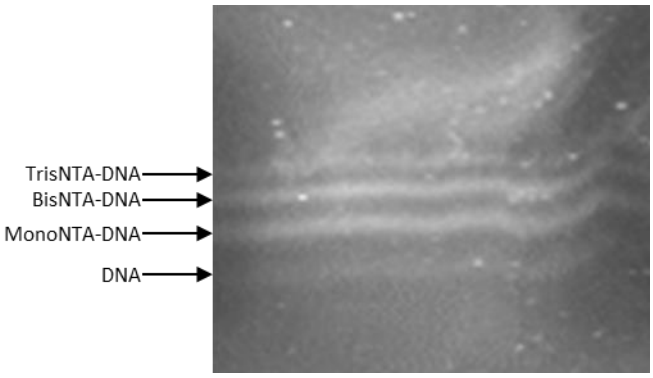

Figure 28: Separation of fully and partially NTA-modified D3N oligonucleotides by urea denaturing gel. The gel was stained with ethidium bromide. Four distinct bands can be seen that likely correspond to tris-, bis-, mono- and non NTA-modified DNA, from top to bottom, respectively.

This image clearly shows four bands of DNA. The fainter bottom band most likely corresponds to unreacted DNA. The middle two bands are the strongest, indicating that most DNA in the mixture is in the form of mono- and bisNTA-modified oligonucleotides. However, some of the DNA is in the form of trisNTA-modified oligonucleotides, as indicated by the presence of the topmost band. These results indicate that the synthesis method might require some modifications in order to increase the yield of trisNTA-modified oligonucleotides. An analysis of the reaction mixture was also performed by RPLC as described by Goodman et al[82], but results were inconclusive. Although some absorbance peaks at 260 nm were observed, somewhat random spikes of absorbance occurred throughout the chromatography process, probably due to an entrapment of an air bubble in the mechanism, resulting in interference in the resulting chromatogram (data not shown).

4.3.2. Formation of CBM3-C:DNA conjugate

The CBM3-C:DNA conjugate was formed simply by mixing the NTA-modified DNA and the CBM3-C together in the presence of a small excess of nickel ions. At first, an excess of 15% was used. The

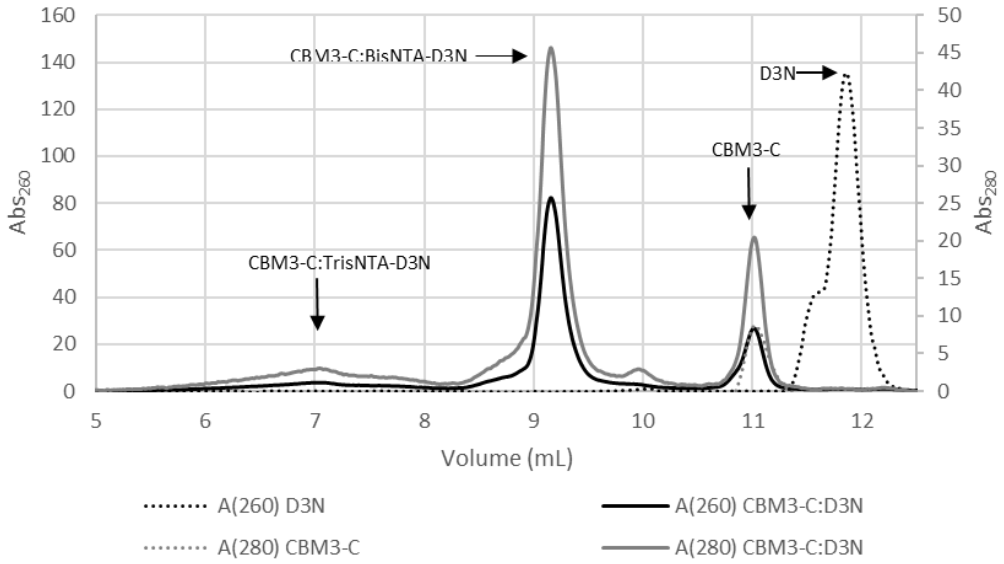

Figure 29: Size exclusion chromatography analysis of the D3N oligonucleotide, CBM3-C and CBM3-C:D3N conjugate. The black and grey dotted lines correspond to the absorption at 260 nm for the D3N oligonucleotide and at 280 nm for CBM3-C, respectively. The black and grey full lines represent the absorption of the CBM3-C:D3N conjugate at 260 nm and 280 nm, respectively.

ratio of DNA to CBM in the mixture was not 1:1 but rather 3:2 to make sure that indeed all the CBM3-C molecules were in the conjugate form. After conjugation, a sample was analyzed by size exclusion chromatography (SEC) and compared to samples containing only the oligonucleotide and CBM3-C (Figure 29). The chromatogram shows that the D3N oligonucleotide elutes just before 12 mL, while CBM3-C elutes at 11 mL. Looking at the difference in molecular weights between D3N and CBM3-C (10.5 kDa *versus* 20.2 kDa), a larger difference in elution volume would be expected, since size is the main driving force behind separation in a SEC process. The results of the analysis of the CBM3-C:D3N conjugate mixture show that there is still some unconjugated CBM3-C, as confirmed by the presence of a peak at 280 nm at 11 mL. Additionally, a tall peak is observed at around 9 mL and a small peak is observed at 7 mL. These should correspond to conjugates of CBM3-C with bisNTA-modified D3N and tris-modified D3N, respectively, as indicated by the relative concentrations of the two oligos in Figure 28, backed by some preliminary studies showing that the interaction between monoNTA-modified D3N and CBM3-C is notoriously weak, being unable to form any conjugates (results not shown).

4.3.3. DNA detection in µPADs

The ability of the CBM3-C:DNA conjugate to capture complementary DNA was tested on the designed µPADs (Figure 13). At first, the objective was to capture the fully complementary DSH DNA strand (Table 2), which was functionalized onto AuNPs. The CBM3-C:DNA conjugate was compared to a similar conjugate prepared with the CBM64 construct. TST buffer was applied in the control areas of

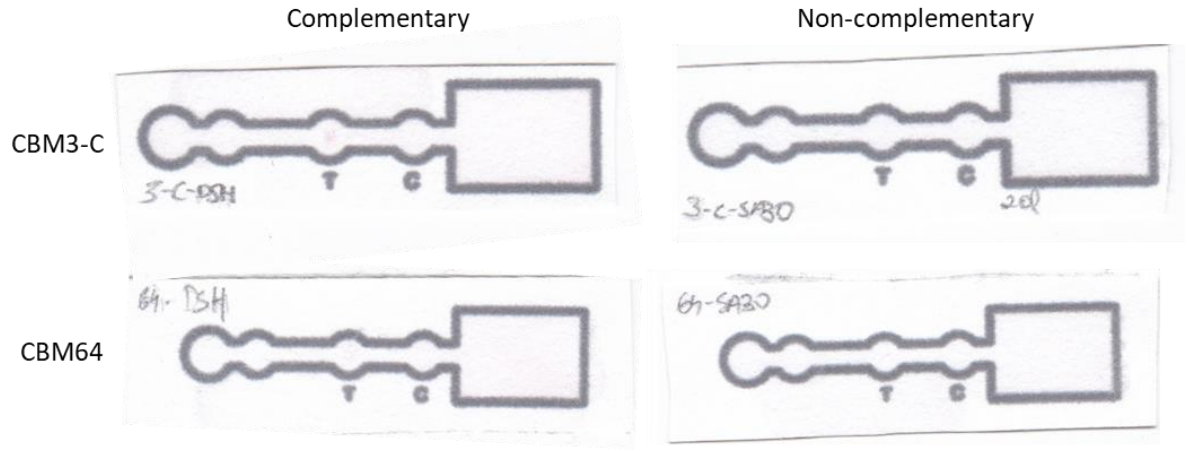

Figure 30: Capture of target DNA strands using µPADs modified with CBM3-C:D3N and CBM64:DNA conjugates. Tests were performed using with AuNPs functionalized with complementary and non-complementary DNA strands**.** Clockwise starting from top left: CBM3-C:D3N tested with AuNPs functionalized with the complementary DNA strand DSH; CBM3-C:D3N tested with AuNPs functionalized with the non-complementary DNA strand SA30; CBM64:D3N tested with AuNPs functionalized with the non-complementary DNA strand SA30; CBM64:D3N tested with AuNPs functionalized with the complementary DNA strand DSH. In all tests pictured above only TST was deposited in the control spot. 5 pmol of each conjugate were deposited in the test spot.

the µPADs, with the same volume as CBM3-C:DNA/CBM64:DNA was applied on the test spot. A control experiment was performed with AuNPs functionalized with non-complementary DNA strands (the SA30 oligonucleotide was used). The images of the µPADs are shown in Figure 30.

Capture of the DSH strand was observed in the µPAD modified with the CBM3-C conjugate and tested with the functionalized AuNPs, as signaled by the red color in the test area (Figure 30, top left). On the contrary, no color was observed in the µPAD that was tested with AuNPs functionalized with the

non-complementary SA30 strand. Thus, it is possible to conclude that this system of nickel-mediated complex between NTA-modified oligonucleotides and CBM3-C can accurately capture complementary DNA strands on a paper support. The µPAD modified with the CBM64 conjugate also produced a signal when tested with the DSH-functionalized AuNPs, but this was fainter and thus is barely perceptible in the figure above (bottom left).

In order to quantify the capture signals produced, the images of all tested µPADs were analyzed with the ImageJ software, and the mean grey intensity and maximum grey intensity of the test zone areas was measured, that is, the mean and maximum amount of grey pixels in a defined area of an 8-bit-transformed image of the µPADs were counted. While the mean grey intensity should give an overall idea of the AuNP intensity a given spot it can be somewhat erroneous. For example, if there is a non-specific accumulation of AuNPs in a test spot, it presents an overall red color. However, DNA capture cannot be assumed as the color is widespread in the spot, with a low maximum intensity. Due to that, the maximum intensity was also measured, to make sure that the mean grey intensity results do correspond to an accurate capture, which will present higher maximum intensity. The mean and maximum grey intensities for the µPADs in Figure 30 are shown in Figure 31.

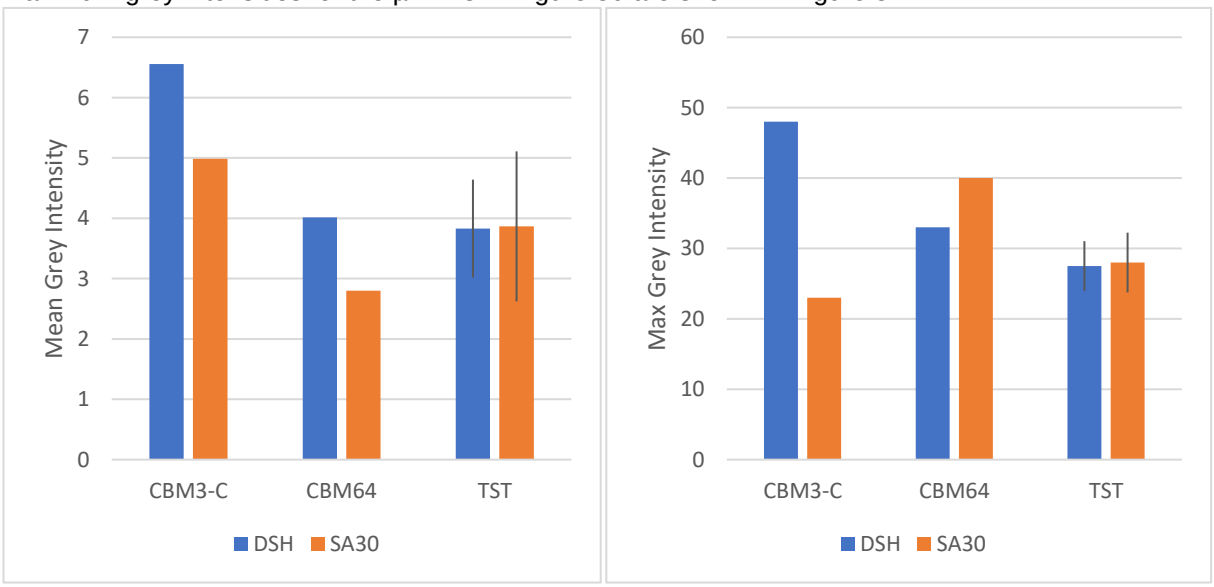

Figure 31: Quantification of the capture of target DNA strands using µPADs modified with CBM3-C:D3N and CBM64:DNA conjugates. The figures show the mean (left) and maximum (right) grey intensities of the test and control spots of the µPADs shown in Figure 30.

Figure 31 shows the importance of showing both mean and maximum grey intensities. Capture of cDNA by CBM3-C conjugates is observed by the notorious increase is both mean and max grey intensity in the test area. However, capture with CBM64 conjugates is not so obvious. Although mean grey intensity values are similar to the controls with TST, max grey intensity values are larger, which may indicate some capture. In the naked eye, a faint signal can be detected in the CBM64 tests, when compared to TST controls. As expected, the tests with SA30-functionalized AuNPs had intensity results similar or lower to those obtained in the TST control areas. The test with CBM64 conjugate and SA30-functionalized AuNPs did indeed show a higher maximum intensity, but a very much lower mean grey intensity. Results obtained in subsequent µPAD tests presented in this thesis are presented as mean and maximum grey intensities. The images of µPADs not shown here are present in Annex II.

4.3.3.1. Salt-aged AuNPs *versus* freezing-functionalized AuNPs

A recent method developed by Liu and Liu describes an easier and quicker way to functionalize AuNPs with thiolated oligonucleotides[80]. Functionalization occurs by freezing a mixture of AuNPs, DNA and sodium phosphate buffer. Freezing causes the formation of ice crystals, which are mainly composed of pure water. The salt, DNA and AuNPs are pushed to the gaps between the ice crystals, thus becoming more concentrated. Freezing also stretches the DNA oligonucleotides, which are then easily adsorbed via the terminal thiol. This method also prevents an issue of salt-aging functionalization, which is the adsorption of DNA to AuNPs via DNA bases. If DNA is adsorbed that way, hybridization of DNA is inactivated since DNA-gold interactions are stronger than the hybridization energy with the complementary DNA. The gradual increase of salt concentration brings more DNA to be adsorbed, which must displace the adsorbed bases with their thiol groups to force an upright conformation of the DNA. These displacement reactions are the reason of the long time that this functionalization requires. On the other hand, since freezing forces DNA molecules in the upright conformation, no displacement of DNA base by thiol is necessary, resulting in a much faster process. After a preliminary test that showed that the capture of complementary DNA (cDNA) is effective using freezing-functionalized AuNPs, the effect of one method of functionalization *versus* the other in the detection of complementary DNA was studied on µPADs. The mean and max grey intensities of the test areas obtained in those µPADs are shown in Figure 32 (images of the corresponding µPADs are shown in Figure 6 of Annex II). As it had already be proven that the CBM3-C:D3N conjugate accurately captures AuNPs functionalized with the target cDNA, the test and control spots were used to examine the effect of amount of conjugate in the capture of AuNPs. Specifically, 2.8 pmol and 6.6 pmol of the CBM3-C:D3N conjugate were deposited in the test and control spots.

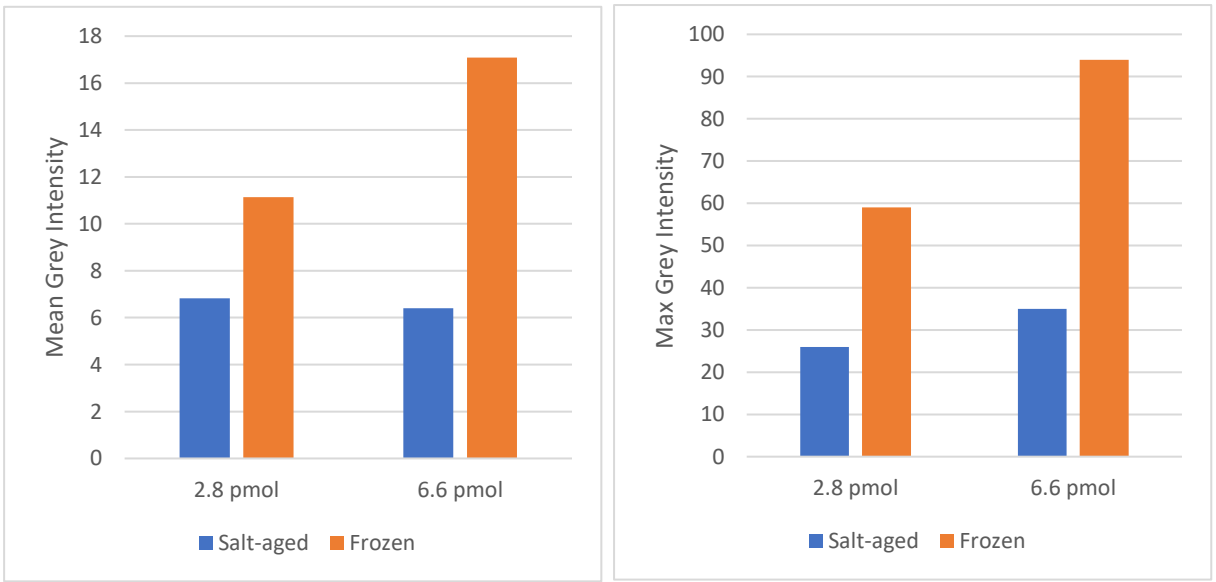

Figure 32: Quantification of the capture of target DNA strands immobilized in AuNPs by salt-aging and freezing using µPADs modified with CBM3-C:D3N conjugates. The figures show the mean (left) and max (right) grey intensities of test and control spots of µPAD tests. The CBM3-C:D3N conjugate was deposited both in the test (2.8 pmol) and control (6.6 pmol) areas of the µPADs.

The positive signals resulting from the tests performed with freezing-functionalized AuNPs were clearly more easily detectable with the naked eye than the signals from the tests with salt-aged AuNPs

(see Figure 6, Annex II). Possibly the higher DNA density[80] in each freezing-functionalized AuNP makes cDNA capture easier. Besides, the much faster time required for freezing-driven functionalization (2 hours plus washings *versus* 16+ hours plus washings for salt-aging) makes it a much more interesting technique to be applied. Therefore, all further tests were performed with freezing-functionalized AuNPs.

4.3.3.2. Optimizing nickel excess

The report describing the method used for the nickel-mediated conjugation of CBM3-C with NTA-modified oligonucleotides refers that conjugation should be done under a small excess of nickel[82]. However, the correct definition of “small excess” is not quite clear. Thus, conjugation reactions were performed under nickel excess percentages of 15% (used in the initial conjugates), 25%, 50% and 100% and PAD capture experiments were performed and compared. Like in the tests in section 4.3.3.1., the control are of the PADs was also used but with an increased amount of CBM3-C:D3N conjugate. However, the number of moles of conjugate in each test/control area was not the same for the different conjugates. As the volume of nickel solution added to the reaction mixture was adjusted to match the final concentration required, the conjugate solutions wound up with different volumes and thus different concentrations of CBM3-C:D3N. In the tests with 15%, 25%, 50% and 100% nickel excess, 3.03 pmol, 2.94 pmol, 2.76 pmol and 2.4 pmol of the conjugate were added to the test spot while 7.56 pmol, 7.35 pmol, 6.89 pmol and 6.11 pmol were added to the control spot, respectively. Nonetheless, results are presented as mean/max grey intensity, as the chief concern of this assay is to obtain easily observable positive signals. The images of the µPADs and quantification of the signals are shown in Figure 33. From the analysis of Figure 33 it is clear that both the mean and max grey intensities are lower in the test spot, where less conjugate was added. In other words, the tests respond accordingly to an increase of deposited conjugate. As to the best conditions for conjugation of this complex, since this test is meant to be observed in the naked eye, the chosen conditions were the ones that showed a clearer positive signal in the µPADs. Thus, the 25% nickel excess was chosen as the best conjugation condition.

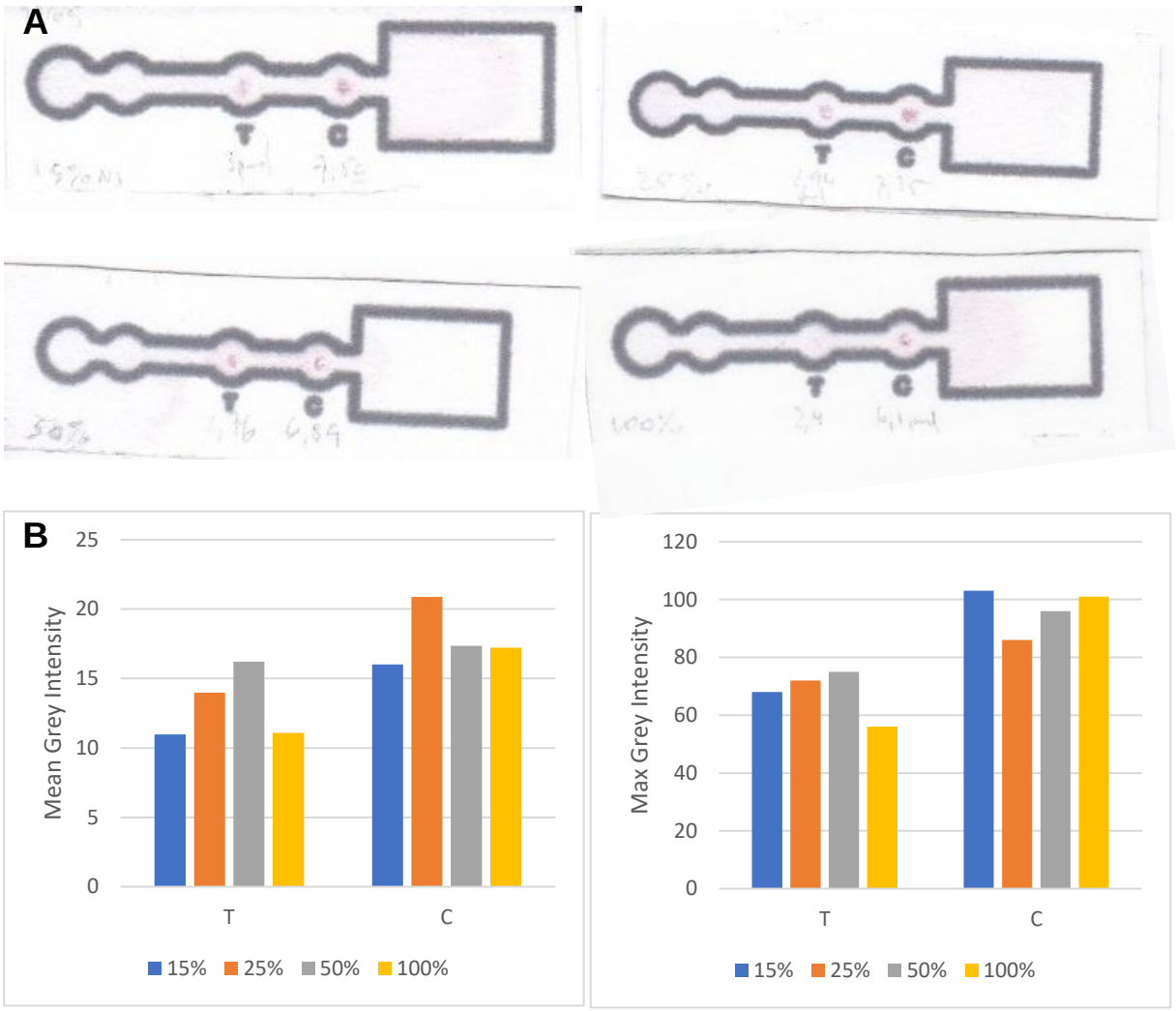

Figure 33: Capture of target DNA strands using µPADs modified with CBM3-C:D3N conjugates prepared with different nickel excesses. A – Images of the µPAD tests for optimization of Ni excess. Top left: test with conjugate resulting from 15% Ni excess; top right: test with conjugate resulting from 25% Ni excess; bottom left: test with conjugate resulting from 50% Ni excess; bottom right: test with conjugate resulting from 100% Ni excess. On the test spot (T) 0.5 µL of the CBM3-C:D3N conjugate solution were deposited while 1.25 µL of the conjugate solution were deposited in the control spot (C). Tests were run with DSH freeze-functionalized-AuNPs. B – Quantification of the signals emitted by the tests in Figure 33A, in the form of the mean (left) and max (right) grey intensities of test and control areas of µPAD tests.

4.3.3.3. Storage of CBM3-C:DNA conjugate

Lastly, some studies were performed regarding the best method of storage of the CBM3-C:DNA conjugate. Storage of the conjugate at 4 ºC resulted in a rapid (few days) and complete loss of its ability to recognize cDNA (data not shown). However, the recognition capacity of the conjugate was retained when storage was performed at -20 ºC. Figure 34 shows the images of the µPADs and the quantification of the emitted signals as mean and max grey intensities of two tests with the conjugate created with 25% excess nickel (2.94 pmol and 7.35 pmol of conjugate in the test and control spots, respectively) that were performed 36 days apart, having the conjugate being stored at -20 ºC in the time being.

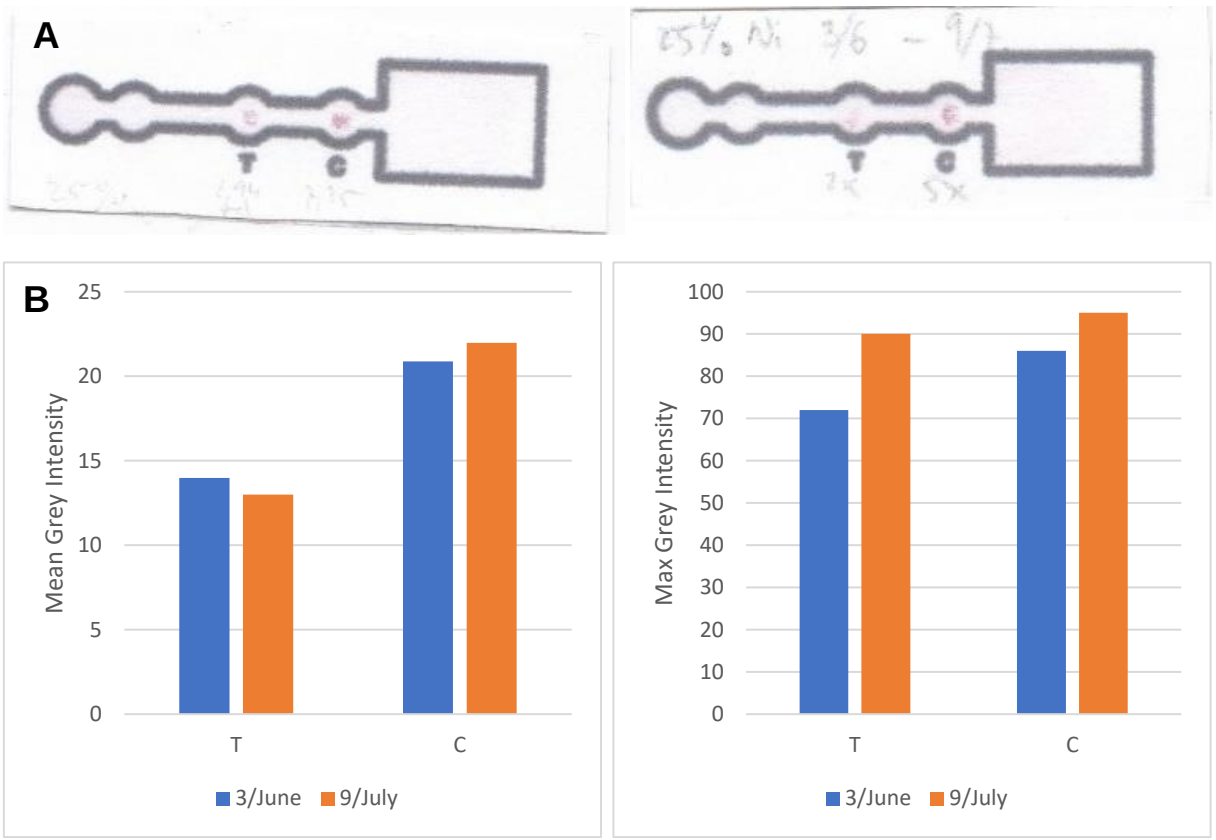

Figure 34: Capture of target DNA strands using µPADs modified with CBM3-C:D3N conjugates stored at -20 ºC for different time periods. A – Images of the µPADs for assessment of conjugate stability at -20 ºC storage. Left: test with conjugate resulting from 25% Ni excess performed on June 3rd. Right: test with conjugate resulting from 25% Ni excess performed on July 9th. On the test spot (T) 0.5 µL of the CBM3-C:D3N conjugate solution were deposited while 1.25 µL of the conjugate solution were deposited in the control spot (C). Tests were run with DSH freeze-functionalized-AuNPs. B – Quantification of the signals emitted by the tests in Figure 34A, in the form of the mean (left) and max (right) grey intensities of test and control areas of µPAD tests.

As observed in Figure 34, the 36 day-long storage had no impact on the cDNA recognition ability of the conjugate. In fact, the later test resulted in higher max grey intensities in both test and control spots, and higher mean grey intensity in the control spot. To the naked eye, no discernible difference was found between the two tests. Therefore, storage of the conjugate at -20 ºC seems suitable.

4.4. DNA recognition system: covalent formation of CBM3-C:DNA conjugate

4.4.1. Synthesis of maleimide-modified oligonucleotides and formation of CBM3-C:DNA conjugates

An alternative conjugation method was tested for the development of a DNA recognition biosensor, which explores the C-terminal cysteine instead of the N-terminal histidine tag (Figure 11A). Aminated oligonucleotides with one (DN3, Table 2) primary amine introduced at the 5´ end of oligonucleotide during synthesis are used as a starting point. These oligos are first modified with sSMCC, a heterobifunctional, water-soluble, non-cleavable crosslinker. sSMCC has a sulfo-NHS ester group that reacts with primary amines, granting the oligonucleotide with a sulfhydryl-reactive maleimide group.

Crosslinking reactions between the oligos and sSMCC need to be undertaken in an amine- and thiol-free buffer, like phosphate, to avoid interactions with buffer components. This modification translates to an increase of 219 g/mol in the molecular weight of the starting oligonucleotide. After modification, oligonucleotides were combined with CBM3-C at a 3:2 ratio as used earlier in the nickel-mediated formation of conjugates.

4.4.2. 3-oligonucleotide capture system

A 3-oligonucleotide capture system was used here to test the CBM3-C:DNA conjugates that is slightly different from the 2-oligonucleotide system used with the nickel-based conjugate. In this system, a smaller oligonucleotide (DN3, Table 2) is immobilized in a CBM3-C conjugate. This oligonucleotide is quite smaller (12 nucleotides) than the D3N oligonucleotide (27 nucleotides) used in the 2-oligonucleotide strategy. The construct is then used to recognize a longer, unmodified cDNA strand, the DT3 oligonucleotide (Table 2), forming a double strand with roughly half of the DT3 strand. The other half of the DT3 strand is then hybridized with a smaller DNA that was functionalized onto AuNPs (DS3, Table 2). A schematic representation of this system is shown in Figure 35. The 3-oligonucleotide strategy is more adequate for eventual practical applications, since it does not require the immobilization of DNA target onto AuNPs. This system was also tested in parallel using nickel-based conjugates prepared as explained in sections. 4.3.1. and 4.3.2, but now using the D3N3 oligonucleotide (Table 2), which has the exact same sequence of nucleotides as the DN3 oligonucleotides, but possesses two further amine modifications, for the stronger conjugation with CBM3-C. The ability of the conjugates CBM3-C:DN3 (prepared by covalent coupling) and CBM3-C:D3N3 (prepared by nickel conjugation) to capture the complementary oligonucleotide DT3 was then tested in µPADs using AuNPs functionalized with the complementary oligonucleotide DS3 for detection. Control experiments were also performed by running µPADs i) with AuNPs functionalized with the non-complementary oligonucleotide SA30 and ii) without addition of the DT3 target. Photographs of the µPADs are shown in Figure 7 of Annex II. Results of mean and max grey intensity of the capture areas in the µPADs are represented in Figure 36.

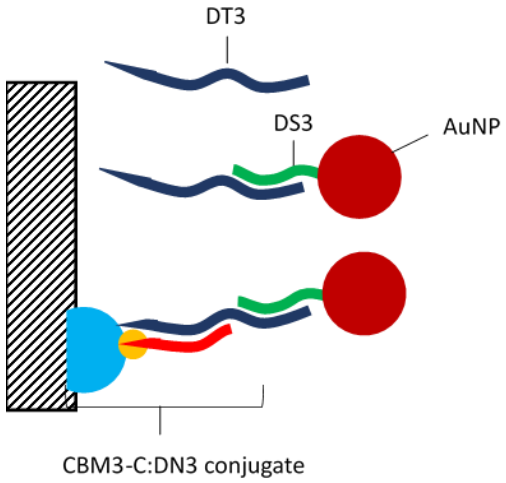

Figure 35: Schematic representation of the 3-oligonucleotide cDNA recognition system. An unmodified DNA strand, DT3, is added to the µPAD, which hybridizes with the smaller, complementary DS3 strand, functionalized onto AuNPs. The DN3 strand conjugated via covalent coupling with CBM3-C recognizes the DT3 target strand by hybridization with the remaining sequence of DT3 that did not hybridize with DS3. So, DN3 will be the capture strand, DT3 the target strand and DS3 the detection strand. A scheme for a 3-oligonucleotide cDNA recognition system based on a CBM3-C conjugated prepared via nickel complexation would be similar, only switching the DN3 oligonucleotide for the D3N3 oligonucleotide.

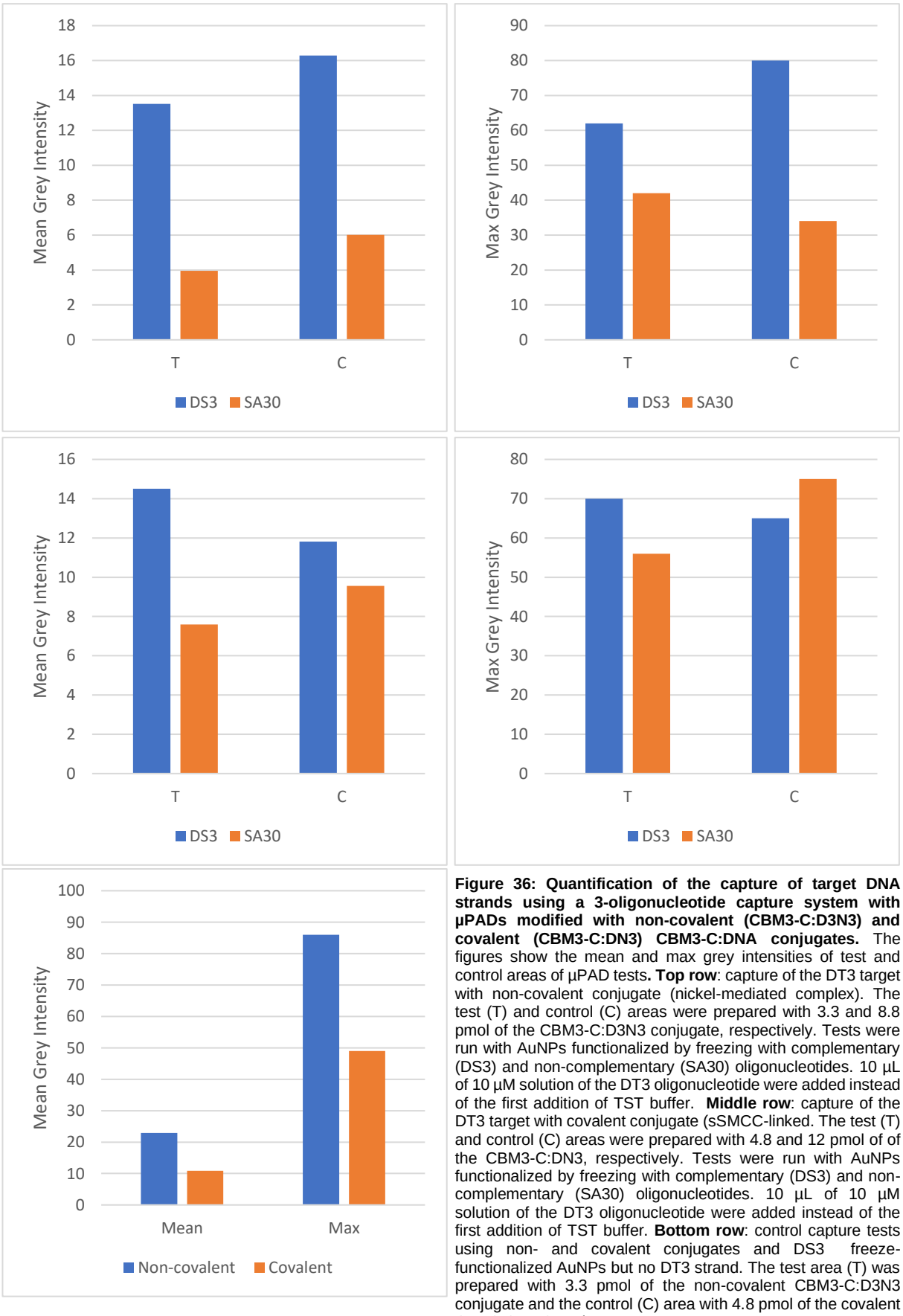

Figure 36: Quantification of the capture of target DNA strands using a 3-oligonucleotide capture system with µPADs modified with non-covalent (CBM3-C:D3N3) and covalent (CBM3-C:DN3) CBM3-C:DNA conjugates. The figures show the mean and max grey intensities of test and control areas of µPAD tests**. Top row**: capture of the DT3 target with non-covalent conjugate (nickel-mediated complex). The test (T) and control (C) areas were prepared with 3.3 and 8.8 pmol of the CBM3-C:D3N3 conjugate, respectively. Tests were run with AuNPs functionalized by freezing with complementary (DS3) and non-complementary (SA30) oligonucleotides. 10 µL of 10 µM solution of the DT3 oligonucleotide were added instead of the first addition of TST buffer. **Middle row**: capture of the DT3 target with covalent conjugate (sSMCC-linked. The test (T) and control (C) areas were prepared with 4.8 and 12 pmol of of the CBM3-C:DN3, respectively. Tests were run with AuNPs functionalized by freezing with complementary (DS3) and non-complementary (SA30) oligonucleotides. 10 µL of 10 µM solution of the DT3 oligonucleotide were added instead of the first addition of TST buffer. **Bottom row**: control capture tests using non- and covalent conjugates and DS3 freeze-functionalized AuNPs but no DT3 strand. The test area (T) was prepared with 3.3 pmol of the non-covalent CBM3-C:D3N3 conjugate and the control (C) area with 4.8 pmol of the covalent CBM3-C:DN3 conjugate.

The top row of Figure 36 presents the results obtained when using the conjugate prepared by nickel-mediated complexation. As expected, both mean and max grey intensities values are higher when using AuNPs are functionalized with a complementary DNA strand (DS3) as opposed to a non-complementary strand (SA30). This indicates that unspecific interactions between the SA30-AuNPs and the molecular components of the system are absent. Results with the sSMCC-linked conjugate also point to capture of DNA, although not as definitively as the previous conjugate. An increase in immobilized conjugate led to a decrease in both mean and max grey intensities for tests with DS3-functionalized AuNPs. Differences in intensities between tests with complementary and non-complementary DNA are also not as pronounced as the ones with the former conjugate. The high mean and max grey intensities of the covalent conjugate in the tests with SA30-functionalized AuNPs when compared to the non-covalent conjugate indicate that binding is not discriminatory in sSMCC-linked conjugates, as SA30-functionalized particles also bind to a large extent. Lastly, the bottom chart of Figure 36 shows the results of a test in which there was no addition of target DNA strand, DT3. It was expected that the results of mean and max grey intensities would be similar to those with SA30-functionalized AuNPs, since the system would not be complete without the DT3 oligonucleotide. However, detection occurred, as intensity values were similar to the ones measured with the complete system, in the case of the covalent conjugate, and even being greater than the complete system with the non-covalent conjugate (Figure 36, top row). This can be explained due to some complementarity between the DS3 and D3N3/DN3 oligonucleotides (Figure 37).

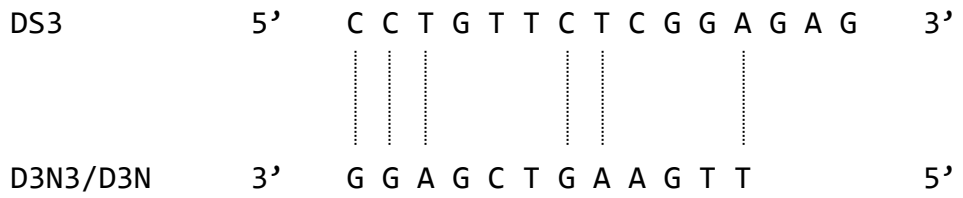

Figure 37: Complementarity between DS3 and D3N3/DN3 oligonucleotides. Lines represent Watson-Crick base pairing.

As 50% of the DN3N/DN3 oligonucleotide is complementary to the DS3 oligonucleotide, direct interaction between the capture and the detection strand is possible. As there is no target strand, this system became a 2-oligonucleotide system, in which non-fully complementary DNA strands are also captured and detected.

4.4.2.1. Wash with low salt buffer

In order to check if the partial hybridization between the capture and the detection strand described above (Figure 37) could be avoided, the tests were repeated with an added step of washing the µPAD after deposition of conjugates. Washing was performed five times with 20 µL of a low salt buffer (20 µM phosphate buffer, pH 7.6). The mean and max grey intensities of the DNA recognition assays after washing are presented in Figure 38.

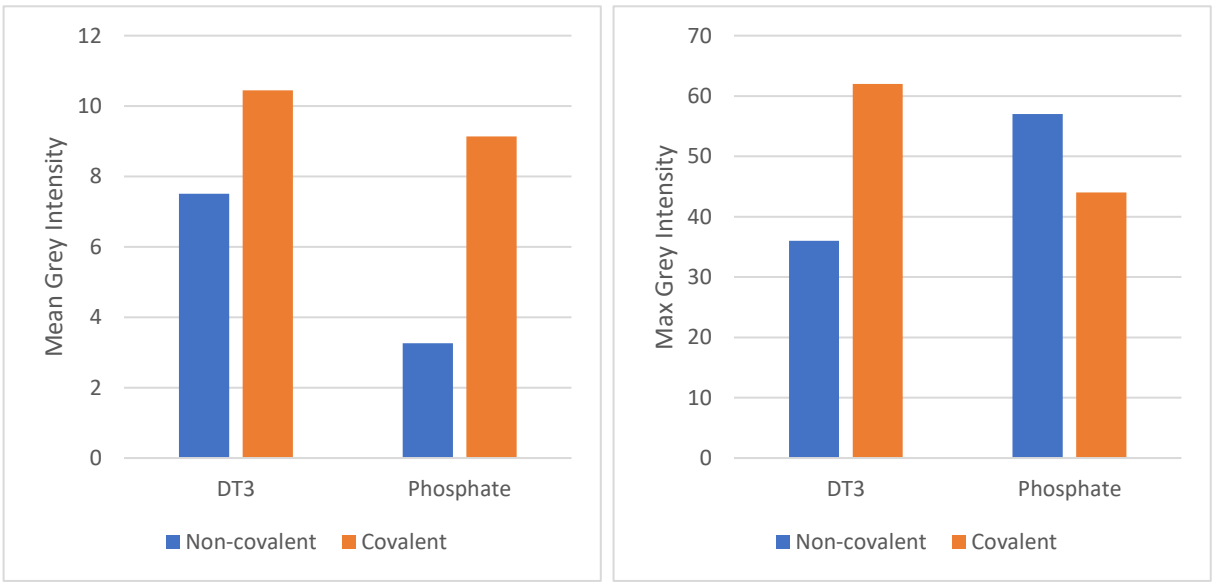

Figure 38: Mean (left) and max (right) grey intensities of test and control spots of µPAD tests assaying the effect of washing after conjugate deposition in the capture of cDNA using CBM3-C:DN3N (non-covalent) and CBM3-C:DN3 (covalent) conjugates. 0.5 µL of CBM3-C:DNA conjugate solution were deposited, amounting to 3.3 and 4.8 pmol of conjugate, respectively. Tests were run with DS3 freeze-functionalized-AuNPs. Assays were done either with addition of DT3 or with addition of the same volume of 20 µM phosphate buffer.

Comparing the results presented in the middle row of Figure 36 with the ones shown in Figure 38, it is possible to see that the washing reduced the mean and max grey intensity resulting from the assays with the covalently-linked conjugate in which the 3-oligonucleotide system is complete. However, no notorious decrease was observed in the assays without DT3. The assays using the nickel-complexed conjugate showed a notorious decrease, whether the system was complete or not. To the naked eye, no color was easily perceptible in these assays, meaning that the washings removed the recognition ability of the non-covalent conjugate (images in Annex II). So, washing the µPAD with a low salt buffer after deposition of conjugate was not successful is aiding the system in the discrimination between fully complementary and non-complementary DNA.

4.5. Proteolytic activity sensor

As discussed in Section 2 and represented schematically in Figure 12, a proteolytic activity sensor based on CBM3-C was designed, using the non-specific protease trypsin as proof-of-concept. The strategy involves a first incubation of the CBM3-C construct (150 µL, 20 µM) with the protease (50 µL) for a certain amount of time and then addition of AuNPs (50 µL, 10 nM) and cellulose micro- or nanoparticles (1 mg in 50 µL) (Figure 12B). The initial trypsin concentration was such so that final concentrations of 10, 100 or 1000 nM were obtained. The extent of the CBM3-C cleavage by trypsin during the initial incubation should affect the ability of CBM3-C to simultaneously adsorb to cellulose and bind AuNPs, leading to an increase of AuNPs in the supernatant after gentle centrifugation for deposition of cellulose nanoparticles, which can be quantified by measuring the supernatant's spectrum.

4.5.1. Influence of trypsin concentration in AuNP spectrum

In order to assess the influence of trypsin in the spectrum of AuNPs, assays were performed first without CBM3-C and with increasing concentrations of trypsin, namely 10 nM, 100 nM and 1000 nM. After deposition of the cellulose nanoparticles, the spectra of the supernatant were measured (Figure 39).

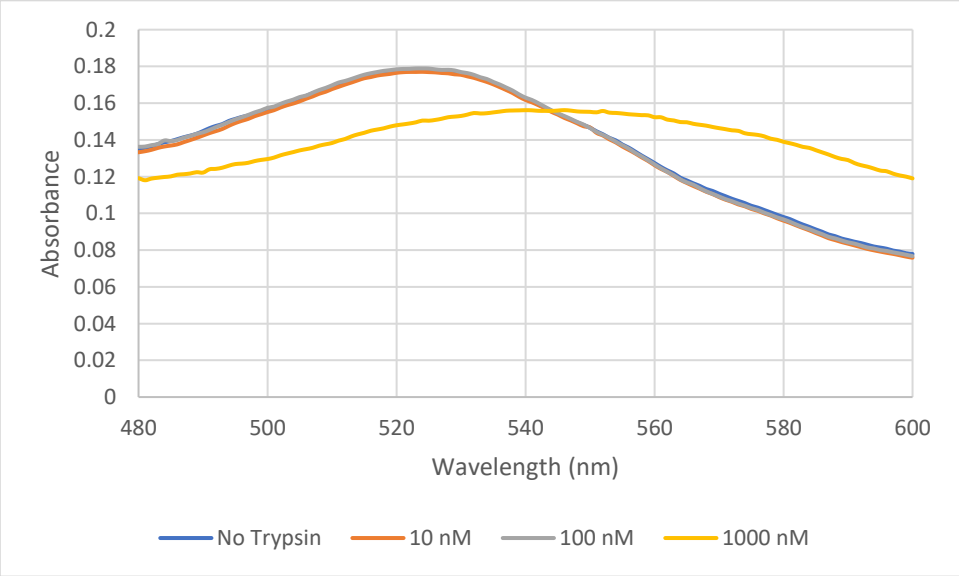

Figure 39: Effect of trypsin concentration on the spectra of AuNP-containing supernatants. Spectra shown are the mean of three separate measurements.

No variations in the spectra obtained with 10 and 100 nM of trypsin were detected when compared with a control spectra obtained with no trypsin. This indicates that trypsin has no effect on the AuNP spectrum when used at a concentration of 10 and 100 nM. However, 1000 nM of trypsin produced a redshift of the absorption band from around 525 nm to around 546 nm. This is most likely due to interactions of AuNPs with thiol groups of cysteines present in trypsin, which leads to a spectrum similar to the one obtained when the SA30 oligonucleotide was functionalized onto AuNPs (Figure 21). Thus, the sensor design is not suitable for sensing proteolytic activity of trypsin at concentrations as high as 1000 nM, as the trypsin itself interacts with the AuNPs.

4.5.2. Sensing proteolytic activity at different incubation times with trypsin

As preliminary tests showed the same results for assays with 10 nM and 100 nM, the following tests were performed with a final trypsin concentration of 10 nM, as it was thought to give better sensitivity to the sensor. CBM3-C was incubated with trypsin for different time intervals, from 5 minutes up to 4 hours. After this incubation, cellulose nanoparticles and AuNPs were added, the cellulose was deposited by gentle centrifugation and the supernatant was collected for spectrum measurement. The spectra of the assays with 5, 15, 30 and 60-minute-long incubation are shown in Figure 40.

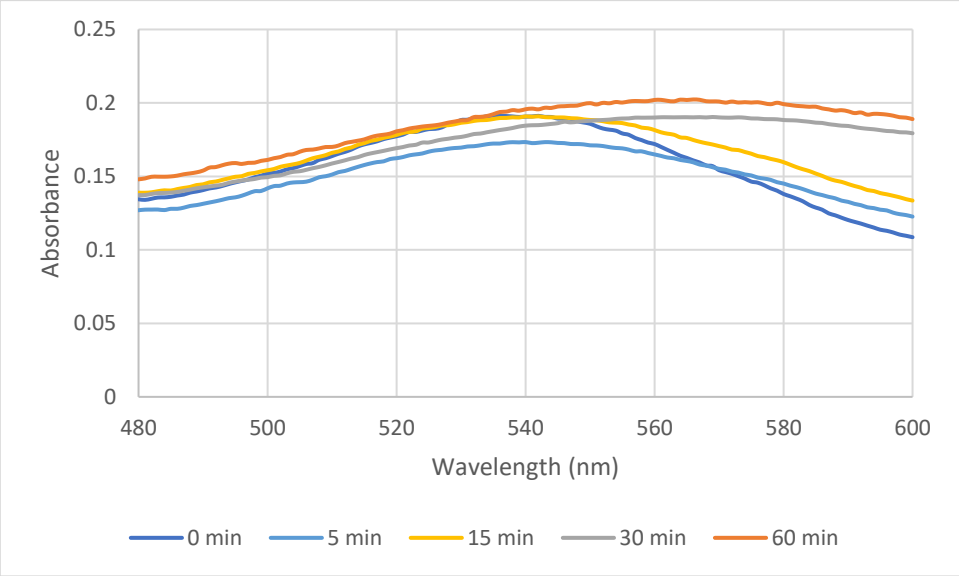

Figure 40: Effect of time of CBM3-C incubation with trypsin on the spectrum of supernatants. Spectra shown are the mean of three separate measurements. Control with 0 min incubation was done without trypsin. Spectra from assays with 2, 3 and 4-hour-long incubations are similar to the spectra of 30 and 60-minute-long incubation, and thus are not shown for increased readability.

One thing of note to take from Figure 40 is that in the spectrum of the assays without trypsin a redshift to 540 nm is also observed. Further tests showed that this redshift is caused by the addition of CBM3-C. Thus, non-adsorbed CBM3-C interacts with AuNPs via thiol-gold interactions, giving rise to this redshift. The assays with 5 and 15-minute-long incubations have similarly shaped spectra to the control, with their absorbance peaks around 540 nm. However, a difference in intensity is observed. The assay with 15-minute-long incubation has an absorbance value similar to the no incubation control, so no particles should be adsorbed via CBM3-C to the cellulose phase. On the other hand, an incubation for 5 minutes displays lower absorbance, meaning that some AuNPs are in the cellulose phase. As the incubation time was lower, fewer CBM3-C were cleaved by trypsin, allowing some deposition of AuNPs together with the cellulose nanoparticles. Spectra from assays with 30-minute or longer incubations show a considerable redshift due to aggregation of AuNPs, which was also observed to the naked eye thanks to a change of color of the supernatant from red to purple. The increased incubation time leads to a more extensive digestion of CBM3-C and autolysis of trypsin, creating smaller peptides. The more diminutive size of these peptides should allow a bigger number of interactions with AuNPs, since they do not occupy as much space around AuNPs as the native proteins, eventually causing aggregation.

The choice for performing these tests with 10 nM trypsin proved to be sensible, since an increased concentration of trypsin would most likely require shorter incubations to observe similar results.

5. Conclusions

As our world rushes relentlessly towards globalization, an increasing number of global health issues starts to emerge. To counteract these issues, diagnostic methods that are more affordable and easier to manage need to be designed for POC application. A ubiquitous material like paper is a good choice for such devices, lowering the cost of production and simplifying transportation and disposal. As a way to bioactivate paper, a protein with affinity towards cellulose such as CBM can be used. Additionally, fusions of CBMs with other moieties may introduce reactive elements that can be explored for conjugation with other biomolecules. One possible fusion is CBM3-C, in which the CBM from *Clostridium thermocellum* was fused to a N-terminal His_6 tag and a C-terminal cysteine. The objectives of this work were to develop paper-based biosensors using this CBM3-C fusion protein.

Firstly, this fusion protein was characterized in regard to its cellulose binding, establishment of gold-thiol interactions with AuNPs, formation of metallic complexes via His6 tag and overall secondary structure. CBM3-C maintained the capability of CBM3 to bind to cellulose, successfully bound both citrate-capped and DNA functionalized AuNPs, formed complexes with Ni^{2+} and Co^{2+} and displayed a similar secondary structure to an unmodified *C. thermocellum* CBM3.

Cellulose micro- and nanoparticles that could be used for the biosensors were observed by scanning electron microscopy (SEM), both by themselves and with AuNPs adsorbed via CBM3-C, confirming that CBM3-C did bind to both cellulose and AuNPs.

CBM3-C was then incorporated into a paper-based biosensor designed for cDNA recognition. First, conjugates of CBM3-C with DNA capture strands were assembled by either exploring the presence of the His_6 tag or of the terminal cysteine. Through the His_6 tag, a nickel complex was established with trisNTA-modified oligonucleotides, while the C-terminal cysteine was covalently bond to maleimide-modified oligonucleotides. Thus, different strategies with different chemistries were tested, the first through non-covalent interactions and the latter through the establishment of a covalent bond. Detection systems were then conceived to test the ability of the DNA strand in the CBM3-C:DNA conjugates to capture complementary target DNA strands in wax-printed µPADs. In a first instance, the nickel complex conjugate was immobilized in the µPAD and used to capture AuNPs functionalized with thiolated DNA strands. Positive signals were obtained when AuNPs were functionalized with complementary DNA strands, while no signal was observed with non-complementary strands. The effect of the AuNP functionalization method, amount of nickel excess in the conjugation reaction and temperature of storage on the performance of the sensor was further investigated.

A 3-oligonucleotide system was also designed that required no modification of the target DNA. Here, detection was performed using AuNPs functionalized with a smaller complementary DNA strand. µPAD tests using this system resulted in more dubious results. Although the nickel complex conjugate accurately detected the target strand when AuNPs were functionalized with complementary strands, producing no signal when AuNPs were functionalized with non-complementary strands, the tests resulted in a positive signal when the target strand was not included. Similar results were observed when using the covalent conjugate, although this seemed to be less discriminatory than the former

conjugate, yielding a positive signal even when AuNPs are functionalized with non-complementary DNA. Washing of the sensors resulted in a complete loss of capture ability by the nickel complex conjugate, while no considerable difference was observed for the covalent conjugate. In the future, this system should be tested using different oligonucleotides that are less complementary, as the complementary strand bound to AuNPs did possess some complementarity to the capture strand conjugated to CBM3-C. Furthermore, the 3-oligonucleotide system would be more similar to what could eventually be used in POC applications, as it uses an unmodified DNA target.

A second biosensor was used to measure proteolytic activity. As CBM3-C simultaneously bound to cellulose (via CBM) and AuNPs (via thiol moiety), the introduction of a non-specific protease should break this cellulose-CBM-AuNP chain. This was measured in a suspension of cellulose nanoparticles, to which AuNPs and CBM3-C that was previously incubated with trypsin were added. Analysis of the spectra of the supernatant measured after deposition of cellulose should give a clue to the extent of proteolytic activity, as a more extensive reaction results in a larger concentration of AuNPs in the supernatant, leading to AuNP aggregation in the long run. This device was meant to be a proof-of-concept and, as such, it was successful. In the future, a similar assay can be performed for drug design against a specific protease, as a target amino acid sequence can be introduced as a linker between CBM and a signal molecule, providing a simple assay for testing drug inhibition of proteases.

6. References

1. Commission on a Global Health Risk Framework for the Future & National Academy of Medicine, S. *The Neglected Dimension of Global Security*. (National Academies Press (US), 2016). doi:10.17226/21891

2. Gates, B. The Next Epidemic - Lessons from Ebola. *N. Engl. J. Med.* **372**, 1381–1384 (2015).

3. Kosack, C. S., Page, A.-L. & Klatser, P. R. A guide to aid the selection of diagnostic tests. *Bull World Heal. Organ* **95**, 639–645 (2017).

4. Grand View Research. *Point of Care Diagnostics/Testing Market Size, Share & Trends Analysis Report by Product (Glucose, Blood Gas/Electrolytes, Cancer Marker), By End Use (Clinic, Hospital), and Segment Forecasts, 2019-2025*. (2019).

5. Kiechle, F. L. & Main, R. I. Blood Glucose: Measurement in the Point-of-Care Setting. *Lab. Med.* **31**, 276–282 (2000).

6. Ehrenkranz, J. R. L. Home and Point-of-Care Pregnancy Tests: A Review of the Technology. *Epidemiology* **13**, s15–s18 (2002).

7. Tolonen, U. *et al.* A handheld nerve conduction measuring device in carpal tunnel syndrome. *Acta Neurol. Scand.* **115**, 390–397 (2007).

8. Body, R. *et al.* Diagnostic accuracy of the T-MACS decision aid with a contemporary point-of-care troponin assay. *Heart* **105**, 768–774 (2019).

9. Sebba, D. *et al.* A point-of-care diagnostic for differentiating Ebola from endemic febrile diseases. *Sci. Transl. Med.* **10**, eaat0944 (2018).

10. Mastrovitch, T. A., Bithoney, W. G., DeBari, V. A. & Gold, N. A. Point-of-care testing for drugs of abuse in an urban emergency department. *Ann. Clin. Lab. Sci.* **32**, 383–386 (2002).

11. Choi, C. J., Wu, H. Y., George, S., Weyhenmeyer, J. & Cunningham, B. T. Biochemical sensor tubing for point-of-care monitoring of intravenous drugs and metabolites. *Lab Chip* **12**, 574–581 (2012).

12. Gao, H. *et al.* A portable electrochemical immunosensor for highly sensitive point-of-care testing of genetically modified crops. *Biosens. Bioelectron.* 111504 (2019). doi:10.1016/j.bios.2019.111504

13. Martins, S. A. *et al.* Biosensors for on-farm diagnosis of mastitis. *Front. Bioeng. Biotechnol.* **7**, 186 (2019).

14. Harrison, D. J., Manz, A., Lüdi, H., Widmer, H. M. & Fan, Z. Capillary Electrophoresis and Sample Injection Systems Integrated on a Planar Glass Chip. *Anal. Chem.* **64**, 1926–1932 (1992).

15. Bilitewski, U., Genrich, M., Kadow, S. & Mersal, G. Biochemical analysis with microfluidic

systems. *Anal. Bioanal. Chem.* **377**, 556–569 (2003).

16. Cate, D. M., Adkins, J. A., Mettakoonpitak, J. & Henry, C. S. Recent Developments in Paper-Based Microfluidic Devices. *Anal. Chem.* **87**, 19–41 (2015).

17. Nilghaz, A., Ballerini, D. R. & Shen, W. Exploration of microfluidic devices based on multi-filament threads and textiles: A review. *Biomicrofluidics* **7**, (2013).

18. West, P. W. A Selective Spot Test for Copper. *Ind. Eng. Chem. - Anal. Ed.* **17**, 740–741 (1945).

19. Comer, J. P. Semiquantitative Specific Test Paper for Glucose in Urine. *Anal. Chem.* **28**, 1748–1750 (1956).

20. Park, J., Shin, J. H. & Park, J. K. Pressed Paper-Based Dipstick for Detection of Foodborne Pathogens with Multistep Reactions. *Anal. Chem.* **88**, 3781–3788 (2016).

21. Posthuma-Trumpie, G. A., Korf, J. & Van Amerongen, A. Lateral flow (immuno)assay: Its strengths, weaknesses, opportunities and threats. A literature survey. *Anal. Bioanal. Chem.* **393**, 569–582 (2009).

22. Martinez, A. W., Phillips, S. T., Butte, M. J. & Whitesides, G. M. Patterned paper as a platform for inexpensive, low-volume, portable bioassays. *Angew. Chemie - Int. Ed.* **46**, 1318–1320 (2007).

23. Consden, R., Gordon, A. H. & Martin, A. J. P. Qualitative analysis of proteins: a partition chromatographic method using paper. *Biochem. J.* **38**, 224 LP – 232 (1944).

24. Carrilho, E., Martinez, A. W. & Whitesides, G. M. Understanding wax printing: A simple micropatterning process for paper-based microfluidics. *Anal. Chem.* **81**, 7091–7095 (2009).

25. Zhang, Y. *et al.* Equipment-free quantitative measurement for microfluidic paper-based analytical devices fabricated using the principles of movable-type printing. *Anal. Chem.* **86**, 2005–2012 (2014).

26. Renault, C., Koehne, J., Ricco, A. J. & Crooks, R. M. 3D wax patterning of paper fluidic devices. *Langmuir* **30**, 7030–6 (2014).

27. Li, X. & Liu, X. Fabrication of three-dimensional microfluidic channels in a single layer of cellulose paper. *Microfluid. Nanofluidics* **16**, 819–827 (2014).

28. Syedmoradi, L. *et al.* Point of care testing: The impact of nanotechnology. *Biosens. Bioelectron.* **87**, 373–387 (2017).

29. Boraston, A. B., Bolam, D. N., Gilbert, H. J. & Davies, G. J. Carbohydrate-binding modules: fine-tuning polysaccharide recognition. *Biochem. J.* **382**, 769–781 (2004).

30. Shoseyov, O., Shani, Z. & Levy, I. Carbohydrate Binding Modules: Biochemical Properties and Novel Applications. *Microbiol. Mol. Biol. Rev.* **70**, 283–295 (2006).

31. Armenta, S., Moreno-Mendieta, S., Sánchez-Cuapio, Z., Sánchez, S. & Rodríguez-Sanoja, R. Advances in molecular engineering of carbohydrate-binding modules. *Proteins Struct. Funct. Bioinforma.* **85**, 1602–1617 (2017).

32. Ficko-Blean, E. & Boraston, A. B. Insights into the recognition of the human glycome by microbial carbohydrate-binding modules. *Curr. Opin. Struct. Biol.* **22**, 570–577 (2012).

33. Van Tilbeurgh, H., Tomme, P., Claeyssens, M., Bhikhabhai, R. & Pettersson, G. Limited proteolysis of the cellobiohydrolase I from Trichoderma reesei. Separation of functional domains. *FEBS Lett.* **204**, 223–227 (1986).

34. Gilkes, N. R., Warren, R. A., Miller, R. C. & Kilburn, D. G. Precise excision of the cellulose binding domains from two Cellulomonas fimi cellulases by a homologous protease and the effect on catalysis. *J. Biol. Chem.* **263**, 10401–10407 (1988).

35. Reese, E. T., Siu, R. G. H. & Levinson, H. S. The Biological Degradation of Soluble Cellulose Derivates and Its Relationship to the Mechanism of Cellulose Hydrolysis. *J. Bacteriol.* **59**, 485–497 (1950).

36. Svensson, B., Jespersen, H., Sierks, M. R. & MacGregor, E. A. Sequence homology between putative raw-starch binding domains from different starch-degrading enzymes. *Biochem. J. Lett.* **264**, 309–11 (1989).

37. Lombard, V., Golaconda Ramulu, H., Drula, E., Coutinho, P. M. & Henrissat, B. The carbohydrate-active enzymes database (CAZy) in 2013. *Nucleic Acids Res.* **42**, 490–495 (2014).

38. Boraston, A. B., Revett, T. J., Boraston, C. M., Nurizzo, D. & Davies, G. J. Structural and thermodynamic dissection of specific mannan recognition by a carbohydrate binding module, TmCBM27. *Structure* **11**, 665–675 (2003).

39. Boraston, A. B. *et al.* Structure and ligand binding of carbohydrate-binding module CsCBM6-3 reveals similarities with fucose-specific lectins and 'galactose-binding' domains. *J. Mol. Biol.* **327**, 659–669 (2003).

40. van Bueren, A. L. & Ficko-Blean, E. Carbohydrate-Binding Modules. (2018). Available at: http://www.cazypedia.org/index.php/Carbohydrate-binding_modules. (Accessed: 2nd January 2019)

41. Oliveira, C., Carvalho, V., Domingues, L. & Gama, F. M. Recombinant CBM-fusion technology - Applications overview. *Biotechnol. Adv.* **33**, 358–369 (2015).

42. Tormo, J. *et al.* Crystal structure of a bacterial family-III cellulose-binding domain: a general mechanism for attachment to cellulose. *EMBO J.* **15**, 5739–5751 (1996).

43. Phelps, M. R., Hobbs, J. B., Kilburn, D. G. & Turner, R. F. B. An autoclavable glucose biosensor for microbial fermentation monitoring and control. *Biotechnol. Bioeng.* **46**, 514–524 (1995).

44. Phelps, M. R., Hobbs, J. B., Kilburn, D. G. & Turner, R. F. B. Technology for regenerable biosensor probes based on enzyme-cellulose binding domain conjugates. *Biotechnol. Prog.* **10**, 433–440 (1994).

45. Tolba, M. *et al.* Oriented Immobilization of Bacteriophages for Biosensor Applications. *Appl. Environ. Microbiol.* **76**, 528–535 (2010).

46. Hinkley, T. C. *et al.* Reporter bacteriophage T7NLC utilizes a novel NanoLuc::CBM fusion for the ultrasensitive detection of: Escherichia coli in water. *Analyst* **143**, 4074–4082 (2018).

47. Hussack, G. *et al.* Multivalent anchoring and oriented display of single-domain antibodies on cellulose. *Sensors* **9**, 5351–5367 (2009).

48. Rosa, A. M. M. *et al.* Capture and Detection of DNA Hybrids on Paper via the Anchoring of Antibodies with Fusions of Carbohydrate Binding Modules and ZZ-Domains. *Anal. Chem.* **86**, 4340–4347 (2014).

49. Rosa, A. M., Nazaré, M. R. & Prazeres, D. M. Colorimetric detection of DNA strands on cellulose microparticles using ZZ-CBM fusions and gold nanoparticles. *Biotechnol. J.* **1800590**, 1800590 (2019).

50. Janegitz, B. C., Cancino, J. & Zucolotto, V. Disposable Biosensors for Clinical Diagnosis. *J. Nanosci. Nanotechnol.* **14**, 378–389 (2014).

51. Zhou, F., Noor, M. O. & Krull, U. J. Luminescence Resonance Energy Transfer-Based Nucleic Acid Hybridization Assay on Cellulose Paper with Upconverting Phosphor as Donors. *Anal. Chem.* **86**, 2719–2726 (2014).

52. Delaney, J. L., Doeven, E. H., Harsant, A. J. & Hogan, C. F. Use of a mobile phone for potentiostatic control with low cost paper-based microfluidic sensors. *Anal. Chim. Acta* **803**, 123–127 (2013).

53. Noiphung, J. *et al.* Electrochemical detection of glucose from whole blood using paper-based microfluidic devices. *Anal. Chim. Acta* **788**, 39–45 (2013).

54. Cunningham, J. C., Brenes, N. J. & Crooks, R. M. Paper electrochemical device for detection of DNA and thrombin by target-induced conformational switching. *Anal. Chem.* **86**, 6166–6170 (2014).

55. Justino, C. I. L., Rocha-Santos, T. A. P. & Duarte, A. C. Advances in point-of-care technologies with biosensors based on carbon nanotubes. *TrAC - Trends Anal. Chem.* **45**, 24–36 (2013).

56. Shen, Y., Tran, T.-T., Modha, S., Tsutsui, H. & Mulchandani, A. A paper-based chemiresistive biosensor employing single-walled carbon nanotubes for low-cost, point-of-care detection. *Biosens. Bioelectron.* **130**, 367–373 (2018).

57. Wu, Y., Xue, P., Kang, Y. & Hui, K. M. Paper-Based Micro fluidic Electrochemical Immunodevice

Integrated with Nanobioprobes onto Graphene Film for Ultrasensitive Multiplexed Detection of Cancer Biomarkers. *Anal. Chem.* **125**, 8661–8668 (2013).

58. Shi, Z., Wu, X., Gao, L., Tian, Y. & Yu, L. Electrodes/paper sandwich devices for in situ sensing of hydrogen peroxide secretion from cells growing in gels-in-paper 3-dimensional matrix. *Anal. Methods* **6**, 4446–4454 (2014).

59. Ma, C. *et al.* 3D origami electrochemical immunodevice for sensitive point-of-care testing based on dual-signal amplification strategy. *Biosens. Bioelectron.* **63**, 7–13 (2015).

60. Li, L. *et al.* A 3D origami electrochemical immunodevice based on a Au@Pd alloy nanoparticle-paper electrode for the detection of carcinoembryonic antigen. *J. Mater. Chem. B* **20**, 6669–6674 (2014).

61. Li, L. *et al.* Sensitive origami dual-analyte electrochemical immunodevice based on polyaniline/Au-paper electrode and multi-labeled 3D graphene sheets. *Electrochim. Acta* **120**, 102–109 (2014).

62. Li, L. *et al.* Growth of gold-manganese oxide nanostructures on a 3D origami device for glucose-oxidase label based electrochemical immunosensor. *Biosens. Bioelectron.* **61**, 76–82 (2014).

63. Su, M. *et al.* Paper-based electrochemical cyto-device for sensitive detection of cancer cells and in situ anticancer drug screening. *Anal. Chim. Acta* **847**, 1–9 (2014).

64. Demirel, G. & Babur, E. Vapor-phase deposition of polymers as a simple and versatile technique to generate paper-based microfluidic platforms for bioassay applications. *Analyst* **139**, 2326–2331 (2014).

65. Liu, W. *et al.* Paper-based colorimetric immunosensor for visual detection of carcinoembryonic antigen based on the high peroxidase-like catalytic performance of ZnFe 2 O 4 -multiwalled carbon nanotubes. *Analyst* **139**, 251–258 (2014).

66. Oh, K. *et al.* Immunochromatographic assay of hepatitis b surface antigen using magnetic nanoparticles as signal materials. *IEEE Trans. Magn.* **50**, 4–7 (2014).

67. Barnett, J. M. *et al.* An inexpensive, fast and sensitive quantitative lateral flow magneto-immunoassay for total prostate specific antigen. *Biosensors* **4**, 204–220 (2014).

68. Chen, Y. *et al.* Rapid detection and quantification of tumor marker carbohydrate antigen 72-4 (CA72-4) using a superparamagnetic immunochromatographic strip. *Anal. Bioanal. Chem.* **408**, 2319–2327 (2016).

69. Zhou, W., Gao, X., Liu, D. & Chen, X. Gold Nanoparticles for In Vitro Diagnostics. *Chem. Rev.* **115**, 10575–10636 (2015).

70. Zhang, Y., Bai, J. & Ying, J. Y. A stacking flow immunoassay for the detection of dengue-specific immunoglobulins in salivary fluid. *Lab Chip* **15**, 1465–1471 (2015).

71. Ruivo, S., Azevedo, A. M. & Prazeres, D. M. F. Colorimetric detection of D-dimer in a paper-based immunodetection device. *Anal. Biochem.* **538**, 5–12 (2017).

72. Gao, X. *et al.* An enzyme-amplified lateral flow strip biosensor for visual detection of MicroRNA-224. *Talanta* **146**, 648–654 (2016).

73. Lie, P., Liu, J., Fang, Z., Dun, B. & Zeng, L. A lateral flow biosensor for detection of nucleic acids with high sensitivity and selectivity. *Chem. Commun.* **48**, 236–238 (2012).

74. Hu, J. *et al.* Oligonucleotide-linked gold nanoparticle aggregates for enhanced sensitivity in lateral flow assays. *Lab Chip* **13**, 4352–4357 (2013).

75. Tsai, T. T., Shen, S. W., Cheng, C. M. & Chen, C. F. Paper-based tuberculosis diagnostic devices with colorimetric gold nanoparticles. *Sci. Technol. Adv. Mater.* **14**, (2013).

76. Zhao, W., Brook, M. A. & Li, Y. Design of gold nanoparticle-based colorimetric biosensing assays. *ChemBioChem* **9**, 2363–2371 (2008).

77. Almeida, A., Rosa, A. M. M., Azevedo, A. M. & Prazeres, D. M. F. A biomolecular recognition approach for the functionalization of cellulose with gold nanoparticles. *J. Mol. Recognit.* **30**, e2634 (2017).

78. Ström, G., Öhgren, C. & Ankerfors, M. *Nanocellulose as an additive in foodstuff*. *Innventia* (2013).

79. Turkevich, J., Stevenson, P. C. & Hillier, J. A study of the nucleation and growth process in the synthesis of colloidal gold. *Discuss. Faraday Soc.* **55**, 55–75 (1951).

80. Liu, B. & Liu, J. Freezing Driven DNA Adsorption on Gold Nanoparticles: Tolerating Extremely Low Salt Concentration but Requiring High DNA Concentration. *Langmuir* acs.langmuir.9b00746 (2019). doi:10.1021/acs.langmuir.9b00746

81. Micsonai, A. *et al.* BeStSel: A web server for accurate protein secondary structure prediction and fold recognition from the circular dichroism spectra. *Nucleic Acids Res.* **46**, W315–W322 (2018).

82. Goodman, R. P. *et al.* A Facile Method for Reversibly Linking a Recombinant Protein to DNA. *ChemBioChem* **10**, 1551–1557 (2009).

83. Pires, V. M. R. R. *et al.* Stability and Ligand Promiscuity of Type A Carbohydrate- binding Modules Are Illustrated by the Structure of Spirochaeta thermophila St CBM64C. *J. Biol. Chem.* **292**, 4847–4860 (2017).

84. Mollenhauer, D. Nitrogen- and phosphine-binding ligands in interaction with gold atoms, clusters, nanoparticles and surfaces. in *Chemical Modelling* **12**, 293–350 (2016).

85. Bürgi, T. Properties of the gold-sulphur interface: from self-assembled monolayers to clusters. *Nanoscale* **7**, 15553–15567 (2015).

86. Zhang, X., Servos, M. R. & Liu, J. Instantaneous and quantitative functionalization of gold nanoparticles with thiolated DNA using a pH-assisted and surfactant-free route. *J. Am. Chem. Soc.* **134**, 7266–7269 (2012).

87. Liu, B. & Liu, J. Methods for preparing DNA-functionalized gold nanoparticles, a key reagent of bioanalytical chemistry. *Anal. Methods* **9**, 2633–2643 (2017).

88. Storhoff, J. J. *et al.* What Controls the Melting Properties of DNA-Linked Gold Nanoparticle Assemblies? *J. Am. Chem. Soc.* **122**, 4640–4650 (2000).

89. Valenti, L. E., De Pauli, C. P. & Giacomelli, C. E. The binding of Ni(II) ions to hexahistidine as a model system of the interaction between nickel and His-tagged proteins. *J. Inorg. Biochem.* **100**, 192–200 (2006).

90. Wegner, S. V & Spatz, J. P. Cobalt(III) as a stable and inert mediator ion between NTA and His6-tagged proteins. *Angew. Chemie - Int. Ed.* **52**, 7593–7596 (2013).

91. Orengo, C. *et al.* CATH – a hierarchic classification of protein domain structures. *Structure* **5**, 1093–1109 (2004).

Annex I

Production of CBM3-C and ZZ-CBM3

Materials and Methods

The recombinant proteins CBM3-C (20.2 kDa) and ZZ-CBM3 (31.9 kDa) were cloned in *E. coli* by NZYTech, Lda. The first protein results from the fusion of a C-terminal cysteine and an N-terminal histidine tag to a carbohydrate binding module from *Clostridium thermocellum* (GenBank: AEI55081.1[77]), CBM3. The second protein corresponds to a fusion of the same CBM with an N-terminal double Z-domain of protein A from *Staphylococcus aureus*. An insert totaling 552 base pairs was cloned into the NdeI-XhoI sites of a pET28a expression vector in the case of CBM3-C, while cloning of ZZ-CBM3 demanded the insertion of an 861 bp insert in the same sites of a pET21a expression vector.

CBM3-C – *184 aa, 20.2 kDa*

MGSSHHHHHHSSGPQQGLRANTPVSGNLKVEFYNSNPSDTTNSINPQFKVTNTGSSAIDLSK
LTLRYYYTVDGQKDQTFWCDHAAIIGSNGSYNGITSNVKGTFVKMSSSTNNADTYLEISFTGGTLE
PGAHVQIQGRFAKNDWSNYTQSNDYSFKSASQFVEWDQVTAYLNGVLVWGKEPGGC

ZZ-CBM3– *286 aa, 31.9 kDa*

MDNKFNKEQQNAFYEILHLPNLNEEQRNAFIQSLKDDPSQSANLLAEAKKLNDAQAPKVDNKF
NKEQQNAFYEILHLPNLNEEQRNAFIQSLKDDPSQSANLLAEAKKLNDAQAPKVSSGLVPRGSTPV
SGNLKVEFYNSNPSDTTNSINPQFKVTNTGSSAIDLSKLTLRYYYTVDGQKDQTFWCDHAAIIGSN
GSYNGITSNVKGTFVKMSSSTNNADTYLEISFTGGTLEPGAHVQIQGRFAKNDWSNYTQSNDYSF
KSASQFVEWDQVTAYLNGVLVWGKEP

Both plasmids (pET-CBM3C-28a, 5.8 kb and pET-ZZCBM3-21a, 6.2 kb) were used to transform *E. coli* DE3 strain BL32 cells. The amino acid sequences of the two recombinant proteins is shown in Figure I-1.

Figure I-1: Amino acid sequence of the recombinant proteins CBM3-C (top) and ZZ-CBM3 (bottom). Blue – hexa-Histidine tag; Green – CBM3 from Clostridium thermocellum; Red – linker; Yellow – ZZ domain derived from the staphylococcal protein A. The residues involved in the binding of CBM3 to cellulose are underlined and the cysteine residues are doubly underlined.

Previously transformed *E. coli* DE3 strain BL21 cells were available when work was started. The cells were grown at 37 ºC with a shaking rate of 260 rotations per minute (rpm) in LB media, complemented with the necessary selection marker (30 ug/ml kanamycin for pET-CBM3C-28a and 100 ug/ml ampicillin for pET-ZZCBM3-21a) at an initial OD_{600} of 0.1. Expression of the recombinant proteins was induced with 1 mM of isopropyl β-D-1-thiogalactopyranoside (IPTG, Fisher Scientific BPΔ 755-10) when $OD_{600} \approx 0.6$. Maintaining the same temperature and shaking rate, expression was carried out for 3 hours.

Following the 3-hour-long incubation, the cell culture was centrifuged for 15 minutes at 6,000 g and 24 ºC (Serial RCB, rotor SLC 3000). The supernatant was discarded and the cell pellet resuspended in a minimal volume of TST buffer or in a buffer containing 10 mM imidazole, 50 mM NaHEPES, 1 M NaCl, 5 mM $CaCl_2$, pH 7.5, for ZZ-CBM3-containing cells and CBM3-C-containing cells, respectively. The resuspended cells were disrupted by sonication (Bandelin Sonoplus) using a MS72 probe for 6 x 30 seconds pulses with a power of 30 W, with 30 second intervals between pulses. During sonication, cells were kept on ice. The resulting suspension was centrifuged at 12,000 g for 25 minutes at 4 ºC, and the supernatant was collected.

Extraction, digestion and analysis of the pET-CBM3C-28a plasmid

Uninduced 5 mL cultures of *E. coli* DE3 strain BL21 cells transformed with the pET-CBM3C-28a plasmid were used in order to extract their plasmid. The NZYTech NZYMiniprep kit was used for plasmid extraction, and final plasmid concentration was measured using a GE Healthcare NanoVue Plus spectrophotometer. The purified plasmid was digested with restriction enzymes (*Eco*RV, *Xho*I (ThermoFisher) and *Age*I (Promega)) to confirm its identity. The digested samples were resolved using electrophoresis in a 1% agarose gel, stained with ethidium bromide and observed in a Stratagene Eagle Eye II cabinet. NZYTech NZYDNA Ladder III was used as a molecular weight marker.

Purification of ZZ-CBM3

Purification of ZZ-CBM3 was achieved by affinity chromatography using a 1 mL column packed with IgG Sepharose 6 Fast Flow (GE Healthcare) resin connected to an ÄKTA 10 Purifier LC System (GE Healthcare). The column was equilibrated with 5 column volumes (CV) of TST and then loaded with the supernatant containing ZZ-CBM3, previously filtered through 0.47 µm filters. Unbound proteins were washed away using 10 CV of TST. The bound ZZ-CBM3 was then eluted with 0.5 M acetic acid, pH 2.8. The flow rate was maintained constant throughout the purification process at 1 mL/min. The absorbance of the eluate was continuously monitored at 280 nm. After fraction collection, the pH is immediately neutralized with 3.2 M Tris buffer, pH 11. The purified ZZ-CBM3 were stored at -20 ºC before use.

Purification of CBM3-C

Purification of CBM3-C was achieved by Immobilized Metal Affinity Chromatography (IMAC) using a 1 mL nickel-containing HisTrap FF column (GE Healthcare) connected to an ÄKTA 10 Purifier LC System (GE Healthcare). Equilibration of the column was done with 5 CV of 10 mM resuspension buffer (10 mM imidazole, 50 mM NaHEPES, 1 M NaCl, 5 mM $CaCl_2$, pH 7.5). The supernatant containing CBM3-C was filtered with 0.47 µm filters and loaded into the column. Unbound proteins were washed away with 15 CV of the equilibration buffer. Imidazole concentration was increased to 35 mM for 10 CV for further washing. Elution of CBM3-C was performede by bringing the imidazole concentration up to 300 mM for 8 CV. The flow rate was maintained constant throughout the purification process, at 1 mL/min. The absorbance of the eluate was continuously monitored at 280 nm. The purified CBM3-C were stored at -20 ºC before use.

SDS-PAGE and Protein Quantification

The purity of CBM3-ZZ and CBM3-C was determined by sodium dodecyl sulfate polyacrylamide gel electrophoresis (SDS-PAGE). The SDS-PAGE analysis was done on polyacrylamide gels with 12% T (total monomer concentration), 3.3% C (weight percentage of crosslinker) for the resolving layer and 4% T, 3.3% C for the stacking layer. 20 µL of purified protein were added to 25 µL of 2x Laemmli Sample buffer (Bio-Rad) and denatured by addition of 5 µL of dithiothreitol (DTT, 1M, Sigma). The samples were then heated in a water bath at 100 ºC for 10 minutes. The protein samples and the NZYTech Low Molecular Weight (LMW) Protein Marker were then loaded into the gel. Commercially available CBM samples of confirmed molecular weight were also run on the gel (CBM3, CBM64, GFP-CBM3, GFP-CBM64, purchased from NZYTech). Electrophoresis was conducted at 90 V, with the gels submerged in running buffer (250 mM Tris-HCl, 1.92 M glycine, 1% SDS, pH 8.3). Staining was performed with Coomassie Brilliant Blue. Images of the gel were obtained with a GS-800 Calibrated Densitometer (Bio-Rad). Protein concentration was determined using the BCA assay (Pierce BCA Protein Assay Kit, Thermo Scientific), according to manufacturer's instructions. CBM3-C protein samples were buffer exchanged to TST using Amicon® Ultra-15 3k Centrifugal Filter Units (Merck), before protein concentration determination, in order to remove excess imidazole.

Results

The image of the gel resultant from the agarose gel electrophoresis of the digestions of the pET-CBM3C-28a plasmid is shown in Figure I-2. Single digestion with *Eco*RV or *Age*I is expected to yield a single DNA fragment - *Eco*RV has a single restriction site in the backbone of the pET28a, while the insert introduced an *Age*I restriction site. Double digestion with *Eco*RV and *Xho*I is expected to result in two bands, as both restriction enzymes have one restriction site each present on the pET-CBM3-28a plasmid. In, the stronger bands identified with white arrows correspond to the expected sizes that the bands resulting from each corresponding digestion should have. However, other bands are identified, mainly in sample digested with *Age*I. These bands are thought to correspond to a pLysS/pLysE plasmid.

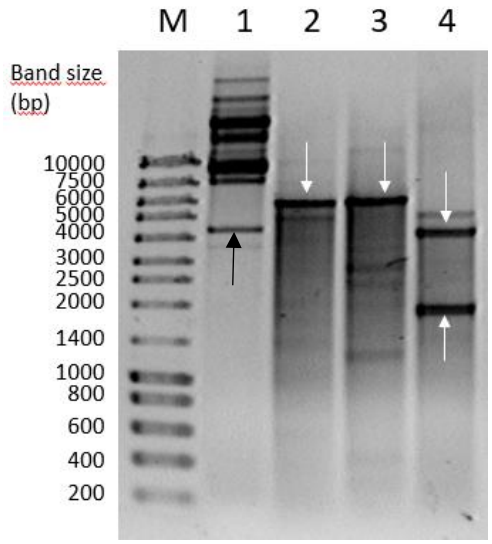

Figure I-2: Agarose gel electrophoresis of the restriction enzyme-digested purified pET-CBM3C-28a plasmid. M – NZYDNA Ladder III marker; 1 – undigested plasmid; 2 – EcoRV digested plasmid; 3 – AgeI digested plasmid; 4 – EcoRV and XhoI double digested plasmid. EcoRV is expected to cut the plasmid in one site in the expression vector; AgeI is expected to cut the plasmid in one site in the insert; XhoI is expected to cut the plasmid in one site in the multiple cloning site. The undigested supercoiled plasmid is identified with a black arrow. Bands of fragments corresponding to the pET-CBM3C-28a plasmid are identified with white arrows. All plasmid fragments migrated according to their expected size. The remaining bands are suspected to correspond to a possible pLysS or pLysE plasmid.

This plasmid codes for T7 lysozyme and its presence causes cell lysis after a freeze-thaw cycle[1], which was, in fact, observed in the cells transformed with the pET-CBM3C-28a plasmid.

The purification of both ZZ-CBM3 and CBM3-C was successful. Chromatograms corresponding to purification runs of ZZ-CBM3 and CBM3-C are shown in Figure I-3. Protein concentration was monitored throughout the purification process by measuring the absorbance at 280 nm at the column outlet.

[1] pET System Manual, 8th edition, Novagen.

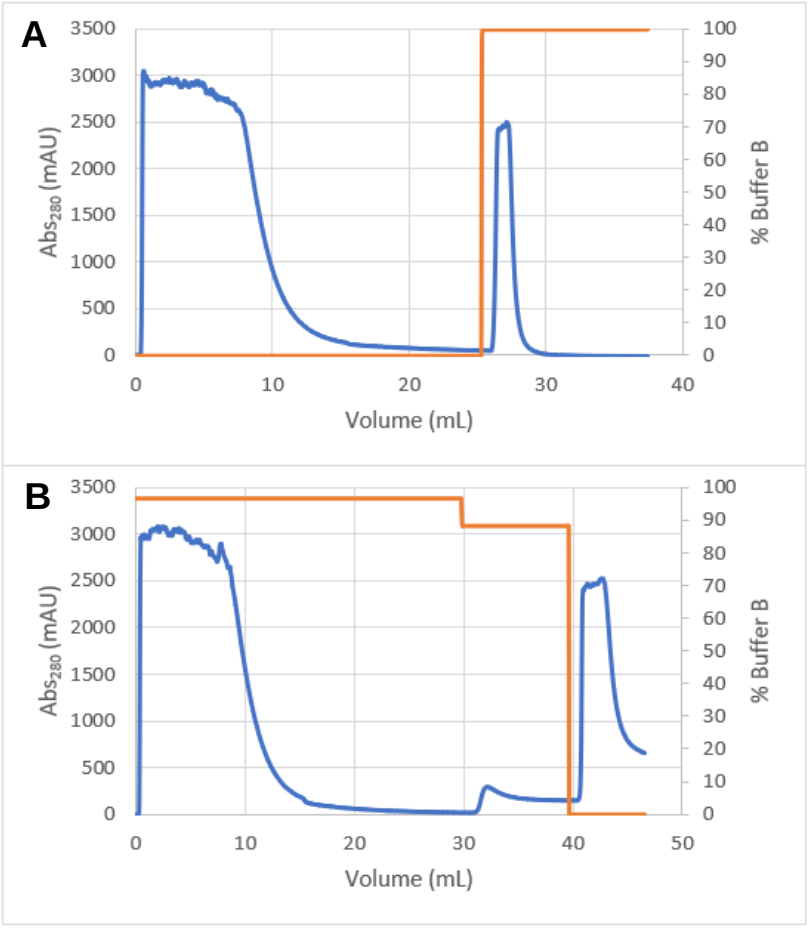

Figure I-3: Chromatograms corresponding to the purification of (a) ZZ-CBM3 with an IgG Sepharose affinity column and (b) CBM3-C with a nickel-containing HisTrap column. Blue lines represent protein concentration, measured by absorbance at 280 nm, and orange lines represent variations in the buffer used during the chromatography. In A, loading and washing of unbound proteins was performed in one step, using TST buffer (Buffer A). The bound ZZ-CBM3 protein was eluted with 0.5 M acetic acid, pH 2.8 (buffer B). After elution, the pH of the proteins in the collected fraction was neutralized with 3.2 M Tris buffer, pH 11. In B, unbound proteins were washed out with 10 mM imidazole, 50 mM NaHEPES, 1 M NaCl, 5 mM $CaCl_2$ pH 7.5. A second wash-out step was included, by increasing imidazole concentration to 35 mM. The bound CBM3-C protein was eluted by increasing the imidazole concentration in the buffer to 300 mM.

Purification of ZZ-CBM3 relies on the binding of the double Z-domain of the fusion to the IgG antibodies present on the resin. Elution is then possible by lowering the pH of the mobile phase passing through the column, which disrupts binding between the ZZ-CBM3 and the IgG antibodies. In Figure 3A, it is possible to observe that the majority of proteins did not bind the column and were washed out with TST. However, when the mobile phase was switched to 0.5 M acetic acid, pH 2.8, a single peak of protein corresponding to ZZ-CBM3 was eluted.

Purification of CBM3-C was possible due to the presence of the N-terminal histidine tag, which interacts with the nickel ions in the resin. Elution is done by increasing the concentration of imidazole, a competitor for nickel interaction. In Figure I-3B, 3 peaks in absorbance at 280 nm were observed. The first peak corresponds to unbound proteins that were washed away. The second, smaller peak is observed when imidazole concentration is increased to 35 mM. This peak may correspond to some metalloproteins that established weaker interactions with the nickel in the resin. The third peak, which corresponds to the elution of CBM3-C, is observed when imidazole concentration was brought up to 300 mM.

Following purification, the eluted recombinant proteins were run on an SDS-PAGE gel (Figure I-4), with the objective of assessing presence and purity of said proteins. The first and last lanes, labeled M, correspond to the NZYTech Low Molecular Weight Protein Marker, with proteins ranging from 18.5 to 96 kDa. Lane 1 contains commercial CBM3, with a molecular weight of 19.6 kDa; Lanes 2 and 3 correspond to the purified CBM3-C and ZZ-CBM3 samples, respectively. Lane 4 shows the GFP-CBM3 construct (63.2 kDa). Lanes 5 and 6 contain CBM64 (11.9 kDa) and its fusion with GFP (39.1 kDa), respectively. Only a single band is observed in the lanes with the purified proteins, which attests to their high purity. All CBM proteins, purified and purchased, show an accurate migration in the gel, according to the molecular weight marker. Thus, it is safe to assume that the production of CBM3-C and ZZ-CBM3 was successful.

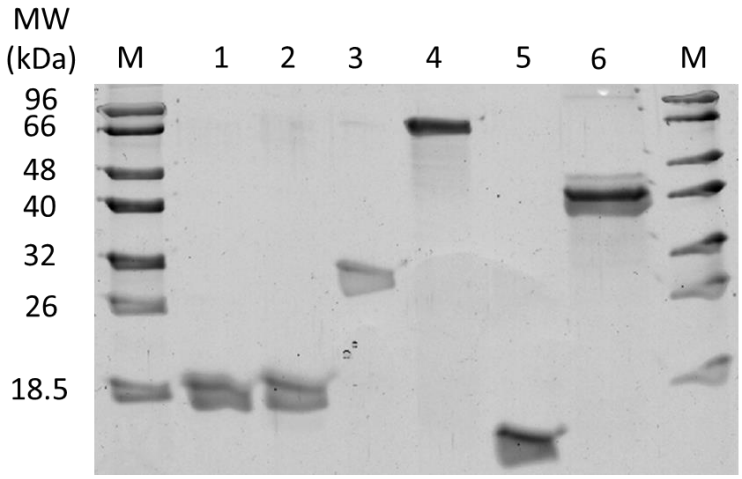

Figure I-4: SDS-PAGE analysis of CBM proteins and fusions, whether purified or commercially purchased. M – NZYTech Low Molecular Weight (LMW) Protein Marker; 1 – CBM3 (19.6 kDa); 2 – CBM3-C (20.2 kDa); 3 – ZZ-CBM3 (31.9 kDa); 4 – GFP-CBM3 (63.2 kDa); 5 – CBM64 (11.9 kDa); 6 – GFP-CBM64 (39.1 kDa). Purified samples correspond to lanes 2 and 3. Lanes 1 and 4-6 correspond to commercially purchased protein samples.

The high concentration of imidazole in the CBM3-C protein sample was removed by exchanging buffers to TST using Amicon® Ultra-15 3k Centrifugal Filter Units (Merck). Then, the protein concentration was determined using the BCA Protein Assay. Following the manufacturer's instructions, a calibration curve was built with known concentrations of BSA solutions to determine the concentration of CBM3-C and ZZ-CBM3. In the end, the obtained solution of ZZ-CBM3 had a protein concentration of 114 µM, while the CBM3-C solution presented 194 µM of protein concentration.

References

1. Commission on a Global Health Risk Framework for the Future & National Academy of Medicine, S. *The Neglected Dimension of Global Security*. (National Academies Press (US), 2016). doi:10.17226/21891

2. Gates, B. The Next Epidemic - Lessons from Ebola. *N. Engl. J. Med.* **372**, 1381–1384 (2015).

3. Kosack, C. S., Page, A.-L. & Klatser, P. R. A guide to aid the selection of diagnostic tests. *Bull World Heal. Organ* **95**, 639–645 (2017).

4. Grand View Research. *Point of Care Diagnostics/Testing Market Size, Share & Trends Analysis Report by Product (Glucose, Blood Gas/Electrolytes, Cancer Marker), By End Use (Clinic, Hospital), and Segment Forecasts, 2019-2025*. (2019).

5. Kiechle, F. L. & Main, R. I. Blood Glucose: Measurement in the Point-of-Care Setting. *Lab. Med.* **31**, 276–282 (2000).

6. Ehrenkranz, J. R. L. Home and Point-of-Care Pregnancy Tests: A Review of the Technology. *Epidemiology* **13**, s15–s18 (2002).

7. Tolonen, U. *et al.* A handheld nerve conduction measuring device in carpal tunnel syndrome. *Acta Neurol. Scand.* **115**, 390–397 (2007).

8. Body, R. *et al.* Diagnostic accuracy of the T-MACS decision aid with a contemporary point-of-care troponin assay. *Heart* **105**, 768–774 (2019).

9. Sebba, D. *et al.* A point-of-care diagnostic for differentiating Ebola from endemic febrile diseases. *Sci. Transl. Med.* **10**, eaat0944 (2018).

10. Mastrovitch, T. A., Bithoney, W. G., DeBari, V. A. & Gold, N. A. Point-of-care testing for drugs of abuse in an urban emergency department. *Ann. Clin. Lab. Sci.* **32**, 383–386 (2002).

11. Choi, C. J., Wu, H. Y., George, S., Weyhenmeyer, J. & Cunningham, B. T. Biochemical sensor tubing for point-of-care monitoring of intravenous drugs and metabolites. *Lab Chip* **12**, 574–581 (2012).

12. Gao, H. *et al.* A portable electrochemical immunosensor for highly sensitive point-of-care testing of genetically modified crops. *Biosens. Bioelectron.* 111504 (2019). doi:10.1016/j.bios.2019.111504

13. Martins, S. A. *et al.* Biosensors for on-farm diagnosis of mastitis. *Front. Bioeng. Biotechnol.* **7**, 186 (2019).

14. Harrison, D. J., Manz, A., Lüdi, H., Widmer, H. M. & Fan, Z. Capillary Electrophoresis and Sample Injection Systems Integrated on a Planar Glass Chip. *Anal. Chem.* **64**, 1926–1932 (1992).

15. Bilitewski, U., Genrich, M., Kadow, S. & Mersal, G. Biochemical analysis with microfluidic systems. *Anal. Bioanal. Chem.* **377**, 556–569 (2003).

16. Cate, D. M., Adkins, J. A., Mettakoonpitak, J. & Henry, C. S. Recent Developments in Paper-Based Microfluidic Devices. *Anal. Chem.* **87**, 19–41 (2015).

17. Nilghaz, A., Ballerini, D. R. & Shen, W. Exploration of microfluidic devices based on multi-filament threads and textiles: A review. *Biomicrofluidics* **7**, (2013).

18. West, P. W. A Selective Spot Test for Copper. *Ind. Eng. Chem. - Anal. Ed.* **17**, 740–741 (1945).

19. Comer, J. P. Semiquantitative Specific Test Paper for Glucose in Urine. *Anal. Chem.* **28**, 1748–

1750 (1956).

20. Park, J., Shin, J. H. & Park, J. K. Pressed Paper-Based Dipstick for Detection of Foodborne Pathogens with Multistep Reactions. *Anal. Chem.* **88**, 3781–3788 (2016).

21. Posthuma-Trumpie, G. A., Korf, J. & Van Amerongen, A. Lateral flow (immuno)assay: Its strengths, weaknesses, opportunities and threats. A literature survey. *Anal. Bioanal. Chem.* **393**, 569–582 (2009).

22. Martinez, A. W., Phillips, S. T., Butte, M. J. & Whitesides, G. M. Patterned paper as a platform for inexpensive, low-volume, portable bioassays. *Angew. Chemie - Int. Ed.* **46**, 1318–1320 (2007).

23. Consden, R., Gordon, A. H. & Martin, A. J. P. Qualitative analysis of proteins: a partition chromatographic method using paper. *Biochem. J.* **38**, 224 LP – 232 (1944).

24. Carrilho, E., Martinez, A. W. & Whitesides, G. M. Understanding wax printing: A simple micropatterning process for paper-based microfluidics. *Anal. Chem.* **81**, 7091–7095 (2009).

25. Zhang, Y. *et al.* Equipment-free quantitative measurement for microfluidic paper-based analytical devices fabricated using the principles of movable-type printing. *Anal. Chem.* **86**, 2005–2012 (2014).

26. Renault, C., Koehne, J., Ricco, A. J. & Crooks, R. M. 3D wax patterning of paper fluidic devices. *Langmuir* **30**, 7030–6 (2014).

27. Li, X. & Liu, X. Fabrication of three-dimensional microfluidic channels in a single layer of cellulose paper. *Microfluid. Nanofluidics* **16**, 819–827 (2014).

28. Syedmoradi, L. *et al.* Point of care testing: The impact of nanotechnology. *Biosens. Bioelectron.* **87**, 373–387 (2017).

29. Boraston, A. B., Bolam, D. N., Gilbert, H. J. & Davies, G. J. Carbohydrate-binding modules: fine-tuning polysaccharide recognition. *Biochem. J.* **382**, 769–781 (2004).

30. Shoseyov, O., Shani, Z. & Levy, I. Carbohydrate Binding Modules: Biochemical Properties and Novel Applications. *Microbiol. Mol. Biol. Rev.* **70**, 283–295 (2006).

31. Armenta, S., Moreno-Mendieta, S., Sánchez-Cuapio, Z., Sánchez, S. & Rodríguez-Sanoja, R. Advances in molecular engineering of carbohydrate-binding modules. *Proteins Struct. Funct. Bioinforma.* **85**, 1602–1617 (2017).

32. Ficko-Blean, E. & Boraston, A. B. Insights into the recognition of the human glycome by microbial carbohydrate-binding modules. *Curr. Opin. Struct. Biol.* **22**, 570–577 (2012).

33. Van Tilbeurgh, H., Tomme, P., Claeyssens, M., Bhikhabhai, R. & Pettersson, G. Limited proteolysis of the cellobiohydrolase I from Trichoderma reesei. Separation of functional domains. *FEBS Lett.* **204**, 223–227 (1986).

34. Gilkes, N. R., Warren, R. A., Miller, R. C. & Kilburn, D. G. Precise excision of the cellulose binding domains from two Cellulomonas fimi cellulases by a homologous protease and the effect on catalysis. *J. Biol. Chem.* **263**, 10401–10407 (1988).

35. Reese, E. T., Siu, R. G. H. & Levinson, H. S. The Biological Degradation of Soluble Cellulose Derivates and Its Relationship to the Mechanism of Cellulose Hydrolysis. *J. Bacteriol.* **59**, 485–497 (1950).

36. Svensson, B., Jespersen, H., Sierks, M. R. & MacGregor, E. A. Sequence homology between putative raw-starch binding domains from different starch-degrading enzymes. *Biochem. J. Lett.* **264**, 309–11 (1989).

37. Lombard, V., Golaconda Ramulu, H., Drula, E., Coutinho, P. M. & Henrissat, B. The carbohydrate-active enzymes database (CAZy) in 2013. *Nucleic Acids Res.* **42**, 490–495 (2014).

38. Boraston, A. B., Revett, T. J., Boraston, C. M., Nurizzo, D. & Davies, G. J. Structural and thermodynamic dissection of specific mannan recognition by a carbohydrate binding module, TmCBM27. *Structure* **11**, 665–675 (2003).

39. Boraston, A. B. *et al.* Structure and ligand binding of carbohydrate-binding module CsCBM6-3 reveals similarities with fucose-specific lectins and 'galactose-binding' domains. *J. Mol. Biol.* **327**, 659–669 (2003).

40. van Bueren, A. L. & Ficko-Blean, E. Carbohydrate-Binding Modules. (2018). Available at: http://www.cazypedia.org/index.php/Carbohydrate-binding_modules. (Accessed: 2nd January 2019)

41. Oliveira, C., Carvalho, V., Domingues, L. & Gama, F. M. Recombinant CBM-fusion technology - Applications overview. *Biotechnol. Adv.* **33**, 358–369 (2015).

42. Tormo, J. *et al.* Crystal structure of a bacterial family-III cellulose-binding domain: a general mechanism for attachment to cellulose. *EMBO J.* **15**, 5739–5751 (1996).

43. Phelps, M. R., Hobbs, J. B., Kilburn, D. G. & Turner, R. F. B. An autoclavable glucose biosensor for microbial fermentation monitoring and control. *Biotechnol. Bioeng.* **46**, 514–524 (1995).

44. Phelps, M. R., Hobbs, J. B., Kilburn, D. G. & Turner, R. F. B. Technology for regenerable biosensor probes based on enzyme-cellulose binding domain conjugates. *Biotechnol. Prog.* **10**, 433–440 (1994).

45. Tolba, M. *et al.* Oriented Immobilization of Bacteriophages for Biosensor Applications. *Appl. Environ. Microbiol.* **76**, 528–535 (2010).

46. Hinkley, T. C. *et al.* Reporter bacteriophage T7NLC utilizes a novel NanoLuc::CBM fusion for the ultrasensitive detection of: Escherichia coli in water. *Analyst* **143**, 4074–4082 (2018).

47. Hussack, G. *et al.* Multivalent anchoring and oriented display of single-domain antibodies on

cellulose. *Sensors* **9**, 5351–5367 (2009).

48. Rosa, A. M. M. *et al.* Capture and Detection of DNA Hybrids on Paper via the Anchoring of Antibodies with Fusions of Carbohydrate Binding Modules and ZZ-Domains. *Anal. Chem.* **86**, 4340–4347 (2014).

49. Rosa, A. M., Nazaré, M. R. & Prazeres, D. M. Colorimetric detection of DNA strands on cellulose microparticles using ZZ-CBM fusions and gold nanoparticles. *Biotechnol. J.* **1800590**, 1800590 (2019).

50. Janegitz, B. C., Cancino, J. & Zucolotto, V. Disposable Biosensors for Clinical Diagnosis. *J. Nanosci. Nanotechnol.* **14**, 378–389 (2014).

51. Zhou, F., Noor, M. O. & Krull, U. J. Luminescence Resonance Energy Transfer-Based Nucleic Acid Hybridization Assay on Cellulose Paper with Upconverting Phosphor as Donors. *Anal. Chem.* **86**, 2719–2726 (2014).

52. Delaney, J. L., Doeven, E. H., Harsant, A. J. & Hogan, C. F. Use of a mobile phone for potentiostatic control with low cost paper-based microfluidic sensors. *Anal. Chim. Acta* **803**, 123–127 (2013).

53. Noiphung, J. *et al.* Electrochemical detection of glucose from whole blood using paper-based microfluidic devices. *Anal. Chim. Acta* **788**, 39–45 (2013).

54. Cunningham, J. C., Brenes, N. J. & Crooks, R. M. Paper electrochemical device for detection of DNA and thrombin by target-induced conformational switching. *Anal. Chem.* **86**, 6166–6170 (2014).

55. Justino, C. I. L., Rocha-Santos, T. A. P. & Duarte, A. C. Advances in point-of-care technologies with biosensors based on carbon nanotubes. *TrAC - Trends Anal. Chem.* **45**, 24–36 (2013).

56. Shen, Y., Tran, T.-T., Modha, S., Tsutsui, H. & Mulchandani, A. A paper-based chemiresistive biosensor employing single-walled carbon nanotubes for low-cost, point-of-care detection. *Biosens. Bioelectron.* **130**, 367–373 (2018).

57. Wu, Y., Xue, P., Kang, Y. & Hui, K. M. Paper-Based Micro fluidic Electrochemical Immunodevice Integrated with Nanobioprobes onto Graphene Film for Ultrasensitive Multiplexed Detection of Cancer Biomarkers. *Anal. Chem.* **125**, 8661–8668 (2013).

58. Shi, Z., Wu, X., Gao, L., Tian, Y. & Yu, L. Electrodes/paper sandwich devices for in situ sensing of hydrogen peroxide secretion from cells growing in gels-in-paper 3-dimensional matrix. *Anal. Methods* **6**, 4446–4454 (2014).

59. Ma, C. *et al.* 3D origami electrochemical immunodevice for sensitive point-of-care testing based on dual-signal amplification strategy. *Biosens. Bioelectron.* **63**, 7–13 (2015).

60. Li, L. *et al.* A 3D origami electrochemical immunodevice based on a Au@Pd alloy nanoparticle-

paper electrode for the detection of carcinoembryonic antigen. *J. Mater. Chem. B* **20**, 6669–6674 (2014).

61. Li, L. *et al.* Sensitive origami dual-analyte electrochemical immunodevice based on polyaniline/Au-paper electrode and multi-labeled 3D graphene sheets. *Electrochim. Acta* **120**, 102–109 (2014).

62. Li, L. *et al.* Growth of gold-manganese oxide nanostructures on a 3D origami device for glucose-oxidase label based electrochemical immunosensor. *Biosens. Bioelectron.* **61**, 76–82 (2014).

63. Su, M. *et al.* Paper-based electrochemical cyto-device for sensitive detection of cancer cells and in situ anticancer drug screening. *Anal. Chim. Acta* **847**, 1–9 (2014).

64. Demirel, G. & Babur, E. Vapor-phase deposition of polymers as a simple and versatile technique to generate paper-based microfluidic platforms for bioassay applications. *Analyst* **139**, 2326–2331 (2014).

65. Liu, W. *et al.* Paper-based colorimetric immunosensor for visual detection of carcinoembryonic antigen based on the high peroxidase-like catalytic performance of ZnFe 2 O 4 -multiwalled carbon nanotubes. *Analyst* **139**, 251–258 (2014).

66. Oh, K. *et al.* Immunochromatographic assay of hepatitis b surface antigen using magnetic nanoparticles as signal materials. *IEEE Trans. Magn.* **50**, 4–7 (2014).

67. Barnett, J. M. *et al.* An inexpensive, fast and sensitive quantitative lateral flow magneto-immunoassay for total prostate specific antigen. *Biosensors* **4**, 204–220 (2014).

68. Chen, Y. *et al.* Rapid detection and quantification of tumor marker carbohydrate antigen 72-4 (CA72-4) using a superparamagnetic immunochromatographic strip. *Anal. Bioanal. Chem.* **408**, 2319–2327 (2016).

69. Zhou, W., Gao, X., Liu, D. & Chen, X. Gold Nanoparticles for In Vitro Diagnostics. *Chem. Rev.* **115**, 10575–10636 (2015).

70. Zhang, Y., Bai, J. & Ying, J. Y. A stacking flow immunoassay for the detection of dengue-specific immunoglobulins in salivary fluid. *Lab Chip* **15**, 1465–1471 (2015).

71. Ruivo, S., Azevedo, A. M. & Prazeres, D. M. F. Colorimetric detection of D-dimer in a paper-based immunodetection device. *Anal. Biochem.* **538**, 5–12 (2017).

72. Gao, X. *et al.* An enzyme-amplified lateral flow strip biosensor for visual detection of MicroRNA-224. *Talanta* **146**, 648–654 (2016).

73. Lie, P., Liu, J., Fang, Z., Dun, B. & Zeng, L. A lateral flow biosensor for detection of nucleic acids with high sensitivity and selectivity. *Chem. Commun.* **48**, 236–238 (2012).

74. Hu, J. *et al.* Oligonucleotide-linked gold nanoparticle aggregates for enhanced sensitivity in lateral flow assays. *Lab Chip* **13**, 4352–4357 (2013).

75. Tsai, T. T., Shen, S. W., Cheng, C. M. & Chen, C. F. Paper-based tuberculosis diagnostic devices with colorimetric gold nanoparticles. *Sci. Technol. Adv. Mater.* **14**, (2013).

76. Zhao, W., Brook, M. A. & Li, Y. Design of gold nanoparticle-based colorimetric biosensing assays. *ChemBioChem* **9**, 2363–2371 (2008).

77. Almeida, A., Rosa, A. M. M., Azevedo, A. M. & Prazeres, D. M. F. A biomolecular recognition approach for the functionalization of cellulose with gold nanoparticles. *J. Mol. Recognit.* **30**, e2634 (2017).

78. Ström, G., Öhgren, C. & Ankerfors, M. *Nanocellulose as an additive in foodstuff*. *Innventia* (2013).

79. Turkevich, J., Stevenson, P. C. & Hillier, J. A study of the nucleation and growth process in the synthesis of colloidal gold. *Discuss. Faraday Soc.* **55**, 55–75 (1951).

80. Liu, B. & Liu, J. Freezing Driven DNA Adsorption on Gold Nanoparticles: Tolerating Extremely Low Salt Concentration but Requiring High DNA Concentration. *Langmuir* acs.langmuir.9b00746 (2019). doi:10.1021/acs.langmuir.9b00746

81. Micsonai, A. *et al.* BeStSel: A web server for accurate protein secondary structure prediction and fold recognition from the circular dichroism spectra. *Nucleic Acids Res.* **46**, W315–W322 (2018).

82. Goodman, R. P. *et al.* A Facile Method for Reversibly Linking a Recombinant Protein to DNA. *ChemBioChem* **10**, 1551–1557 (2009).

83. Pires, V. M. R. R. *et al.* Stability and Ligand Promiscuity of Type A Carbohydrate- binding Modules Are Illustrated by the Structure of Spirochaeta thermophila St CBM64C. *J. Biol. Chem.* **292**, 4847–4860 (2017).

84. Mollenhauer, D. Nitrogen- and phosphine-binding ligands in interaction with gold atoms, clusters, nanoparticles and surfaces. in *Chemical Modelling* **12**, 293–350 (2016).

85. Bürgi, T. Properties of the gold-sulphur interface: from self-assembled monolayers to clusters. *Nanoscale* **7**, 15553–15567 (2015).

86. Zhang, X., Servos, M. R. & Liu, J. Instantaneous and quantitative functionalization of gold nanoparticles with thiolated DNA using a pH-assisted and surfactant-free route. *J. Am. Chem. Soc.* **134**, 7266–7269 (2012).

87. Liu, B. & Liu, J. Methods for preparing DNA-functionalized gold nanoparticles, a key reagent of bioanalytical chemistry. *Anal. Methods* **9**, 2633–2643 (2017).

88. Storhoff, J. J. *et al.* What Controls the Melting Properties of DNA-Linked Gold Nanoparticle Assemblies? *J. Am. Chem. Soc.* **122**, 4640–4650 (2000).

89. Valenti, L. E., De Pauli, C. P. & Giacomelli, C. E. The binding of Ni(II) ions to hexahistidine as a model system of the interaction between nickel and His-tagged proteins. *J. Inorg. Biochem.* **100**,

192–200 (2006).

90. Wegner, S. V & Spatz, J. P. Cobalt(III) as a stable and inert mediator ion between NTA and His6-tagged proteins. *Angew. Chemie - Int. Ed.* **52**, 7593–7596 (2013).

91. Orengo, C. *et al.* CATH – a hierarchic classification of protein domain structures. *Structure* **5**, 1093–1109 (2004).

Annex II

Scanning electron microscopy images

As discussed in section 4.2., SEM images of the different cellulose matrices tested (chromatographic paper, Sigmacell 20 microparticles and microfibrilated cellulose) at different magnifications were obtained. These images are presented below.

Chromatographic paper

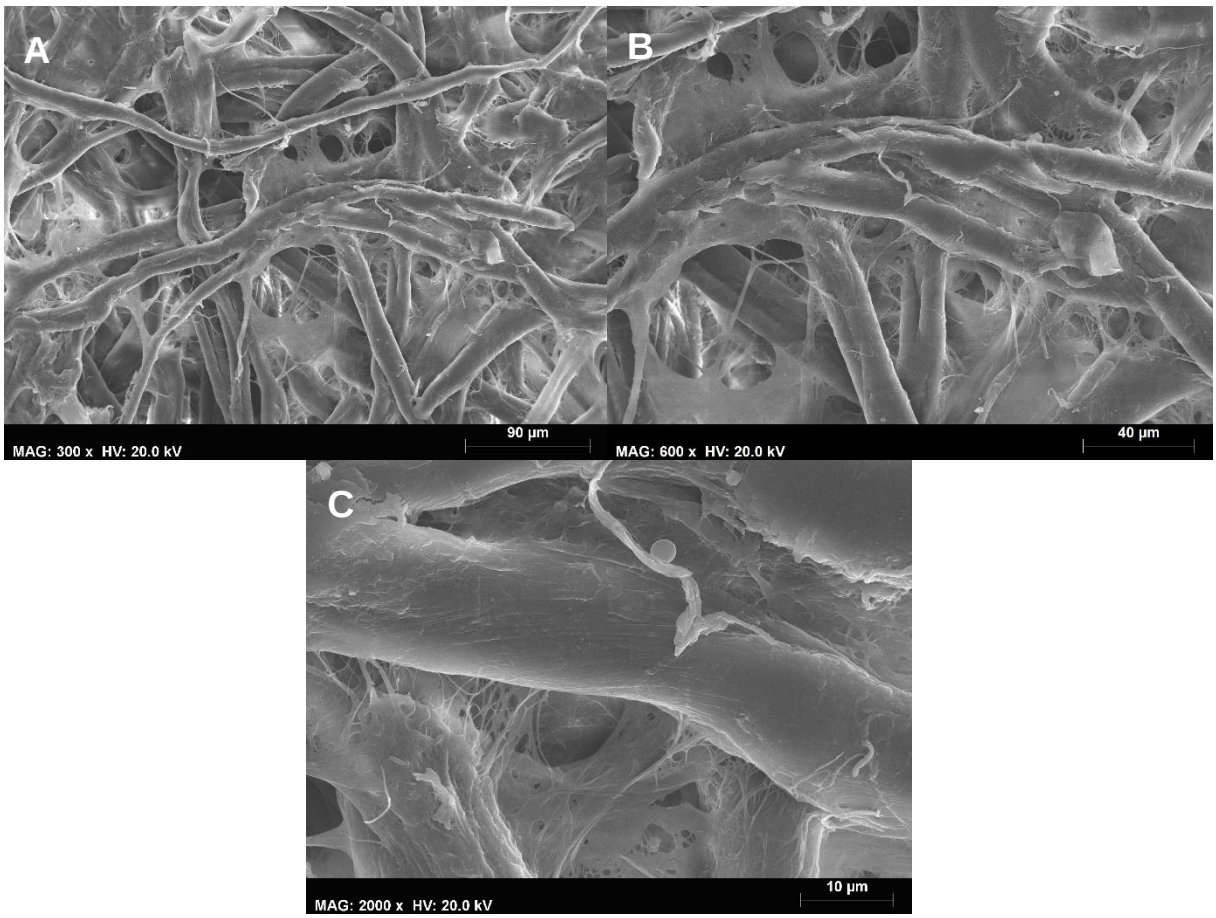

Figure II-1: SEM images of chromatographic paper at different magnifications. A – Image obtained at 300x magnification (scale bar: 90 µm); B – Image obtained at 600x magnification (scale bar: 40 µm); C – Image obtained at 2,000x magnification (scale bar: 10 µm). Microscope: Hitachi S 2400 Scanning Electron Microscope.

Cellulose microparticles

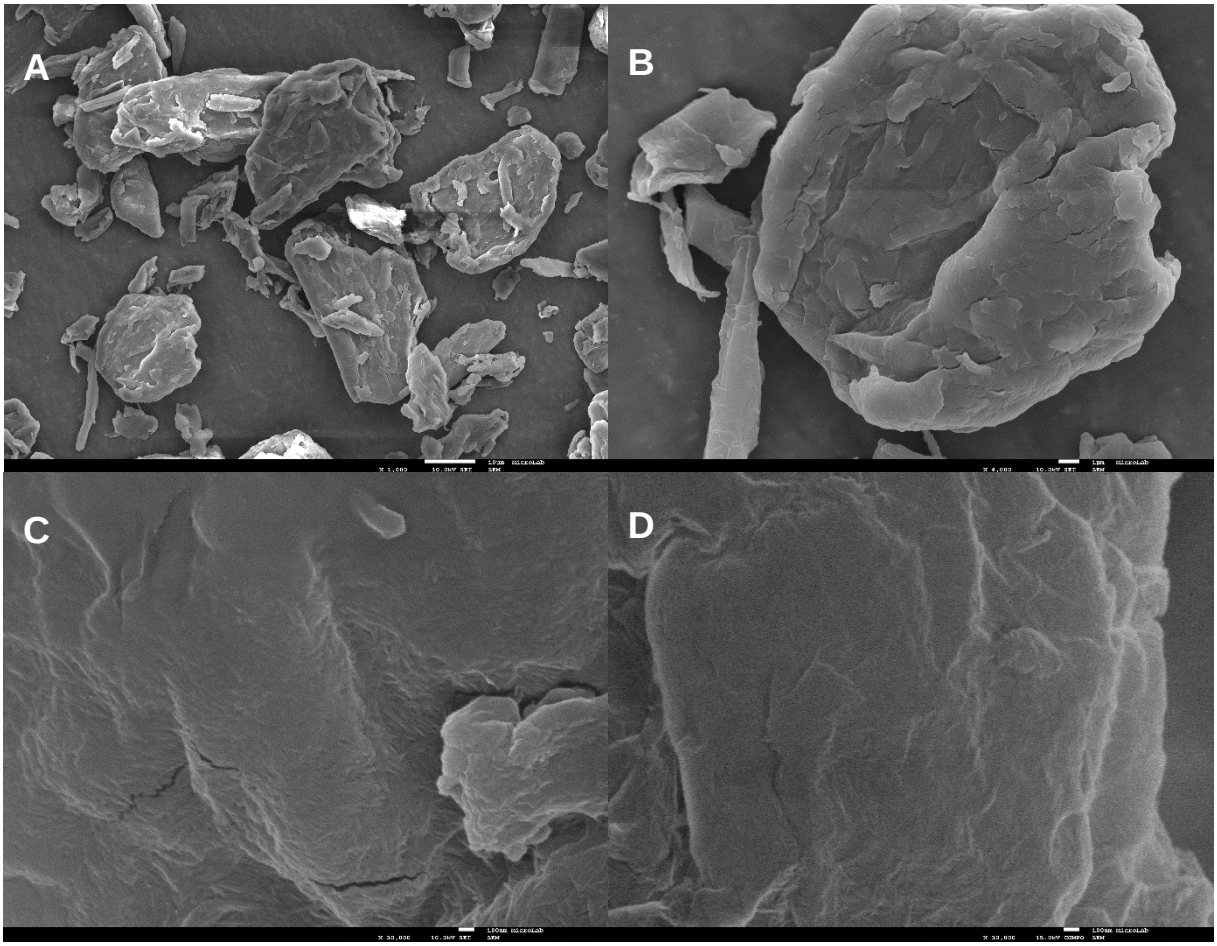

Figure II-2: SEM images of cellulose microparticles at different magnifications. A – Image obtained at 1,000x magnification (scale bar: 10 µm); B – Image obtained at 4,000x magnification (scale bar: 1 µm); C and D – Images obtained at 30,000x magnification (scale bar: 100 nm). Images A – C were obtained using secondary electron imaging, while image D was obtained using composition back scattered electron imaging. Microscope: JEOL JSM7001F Field Emission Gun Scanning Electron Microscope.

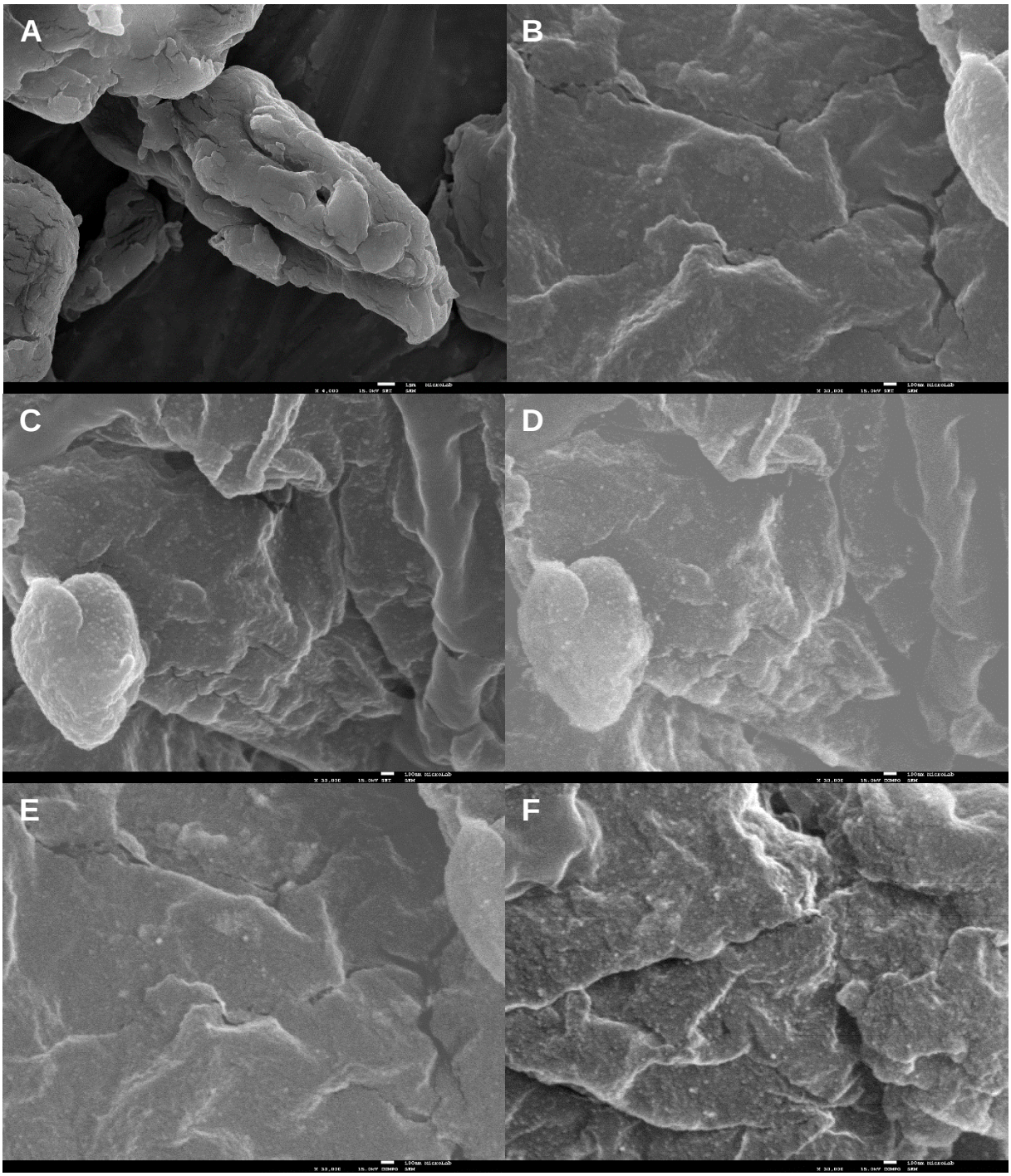

Figure II-3: SEM images of cellulose microparticles with AuNPs adsorbed via CBM3-C at different magnifications. A – Image obtained at 4,000x magnification; B to F – Images obtained at 30,000x magnification. Scale bar: 100 nm. Images A – C were obtained using secondary electron imaging, while images D – F were obtained using composition back scattered electron imaging. Microscope: JEOL JSM7001F Field Emission Gun Scanning Electron Microscope.

Cellulose nanoparticles

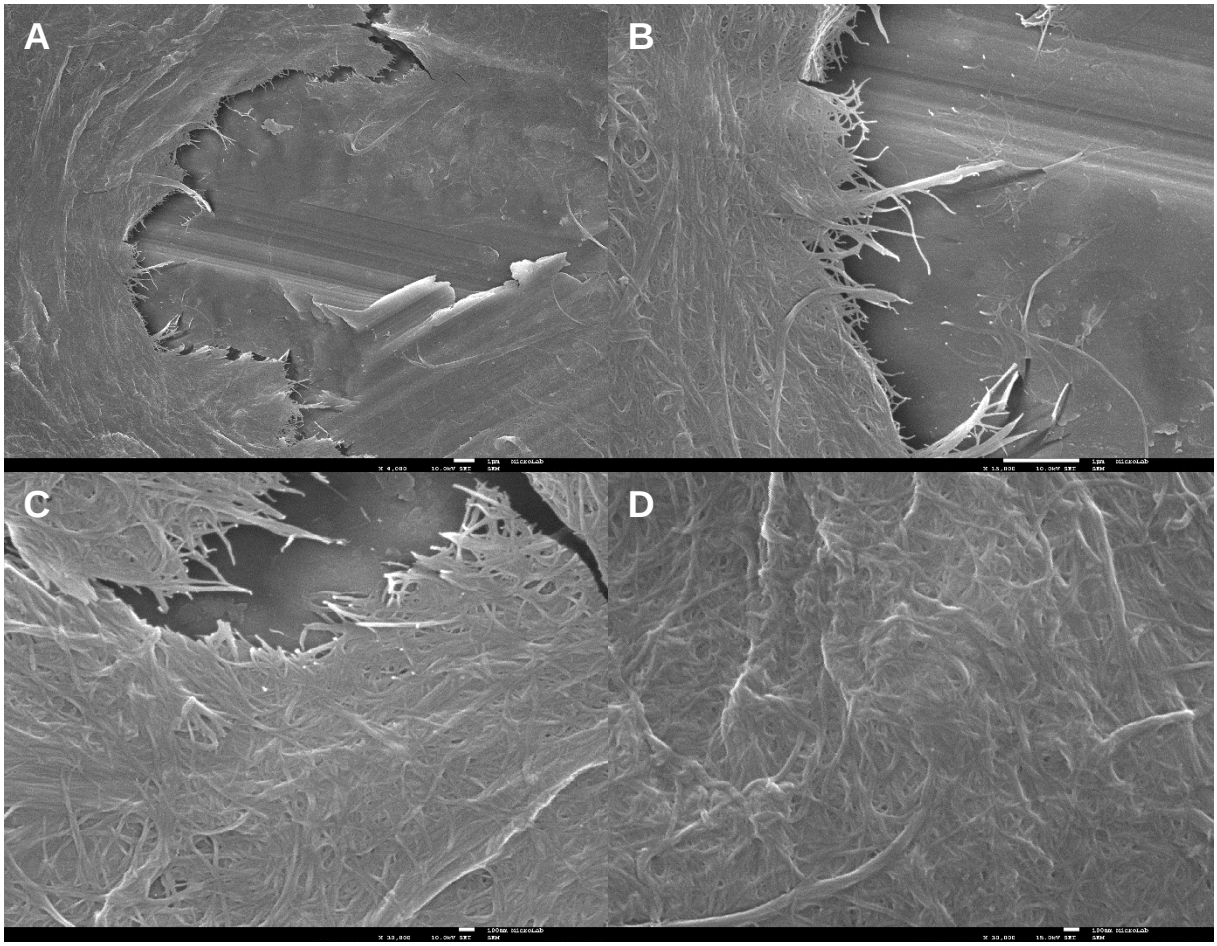

Figure II-4: SEM images of cellulose nanoparticles at different magnifications. A – Image obtained at 4,000x magnification (scale bar: 1 µm); B – Image obtained at 15,000x magnification (scale bar: 1 µm); C and D – Images obtained at 30,000x magnification (scale bar: 100 nm). All images were obtained using secondary electron imaging. Microscope: JEOL JSM7001F Field Emission Gun Scanning Electron Microscope.

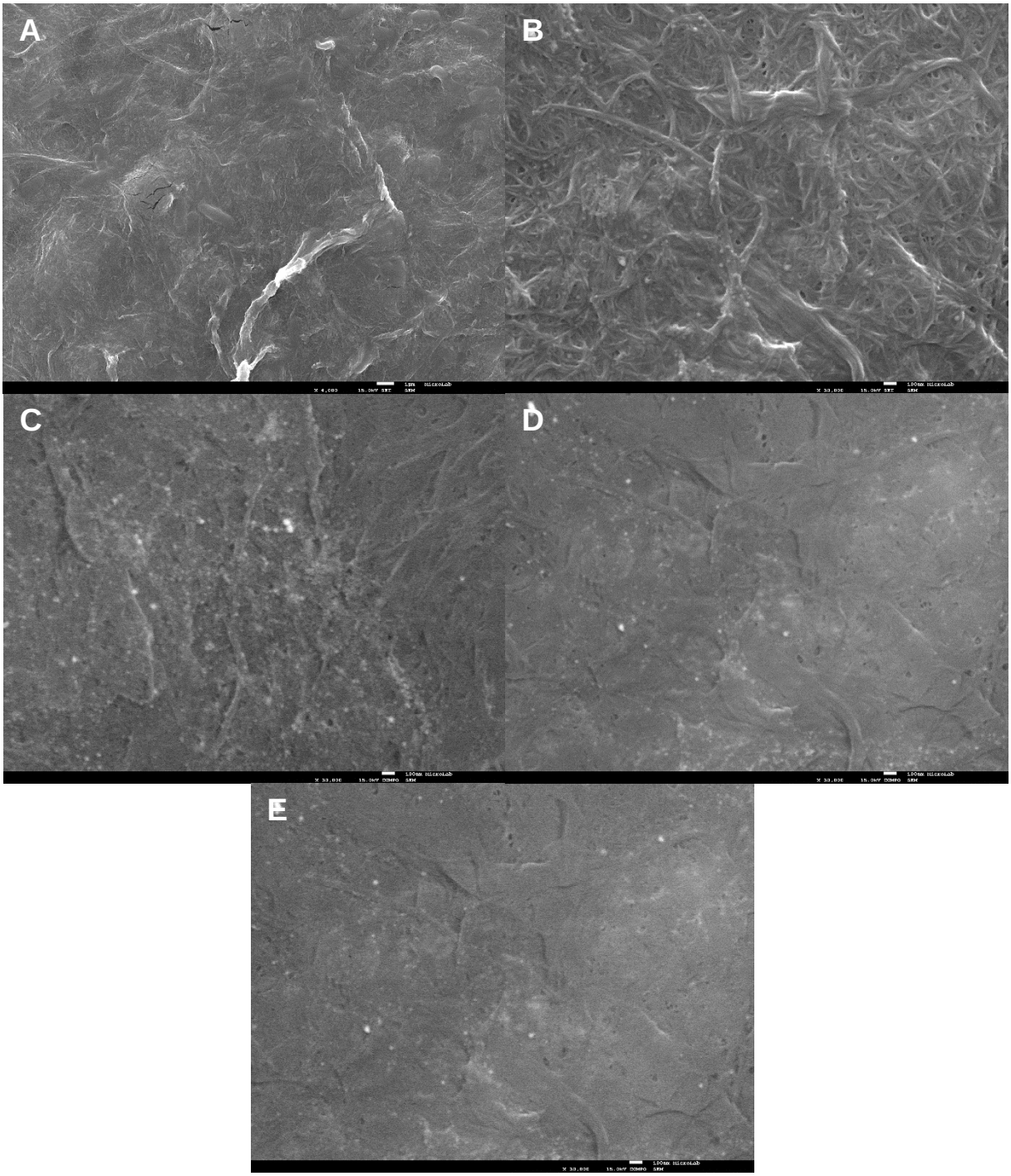

Figure II-5: SEM images of cellulose nanoparticles with AuNPs adsorbed via CBM3-C at different magnifications. A – Image obtained at 4,000x magnification (scale bar: 1 µm); B to E – Images obtained at 30,000x magnification (scale bar: 100 nm); Images A – B were obtained using secondary electron imaging, while images C – E were obtained using composition back scattered electron imaging. Microscope: JEOL JSM7001F Field Emission Gun Scanning Electron Microscope.

µPAD tests

The images of the µPAD tests corresponding to the data presented in sections 4.3. and 4.4. are shown below.

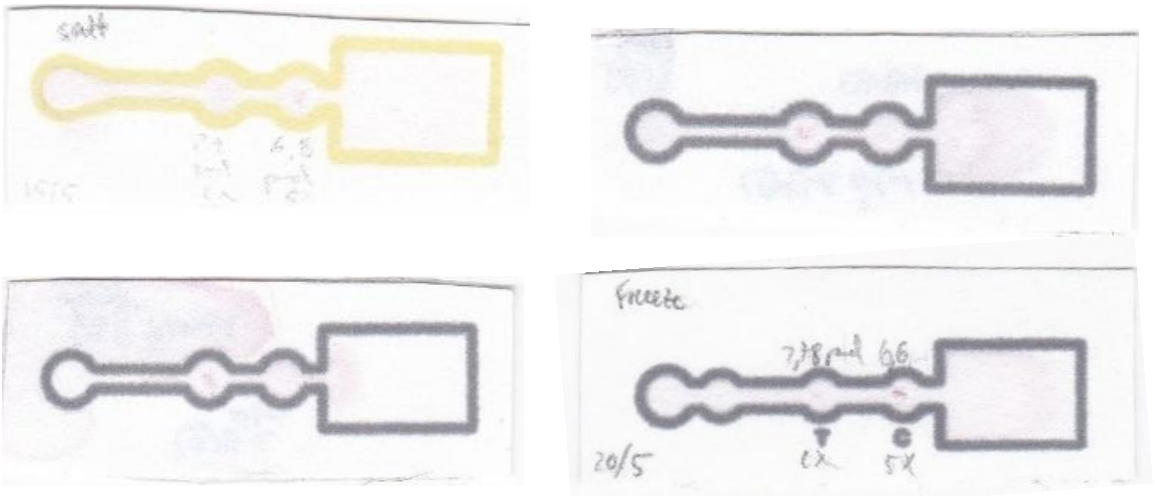

Figure II-6: µPAD tests with CBM3-C:D3N and CBM64:DNA conjugates, concerning section 4.3.3.1., testing salt-aged AuNPs versus freezing-functionalized AuNPs. Top row, left: CBM3-C:D3N tested with salt-aged AuNPs functionalized with the complementary DNA strand DSH. Addition of 2.7 pmol and 6.8 pmol of CBM3-C:D3N conjugate was performed to the test and control spots, respectively. Top row, right: CBM3-C:D3N and CBM64:D3N tested with salt-aged AuNPs functionalized with the complementary DNA strand DSH. Addition of 3 pmol of CBM3-C:D3N and CBM64:D3N was performed to the test and control spots, respectively. Bottom row, left: CBM3-C:D3N tested with freezing-functionalized AuNPs with the complementary DNA strand DSH. Addition of 3 pmol of CBM3-DN3 conjugate and TST was performed to the test and control spots, respectively. Bottom row, right: CBM3-C:D3N tested with freezing-functionalized AuNPs with the complementary DNA strand DSH. Addition of 2.78 and 6.6 pmol of CBM3-C:D3N conjugate was performed to the test and control spots, respectively.

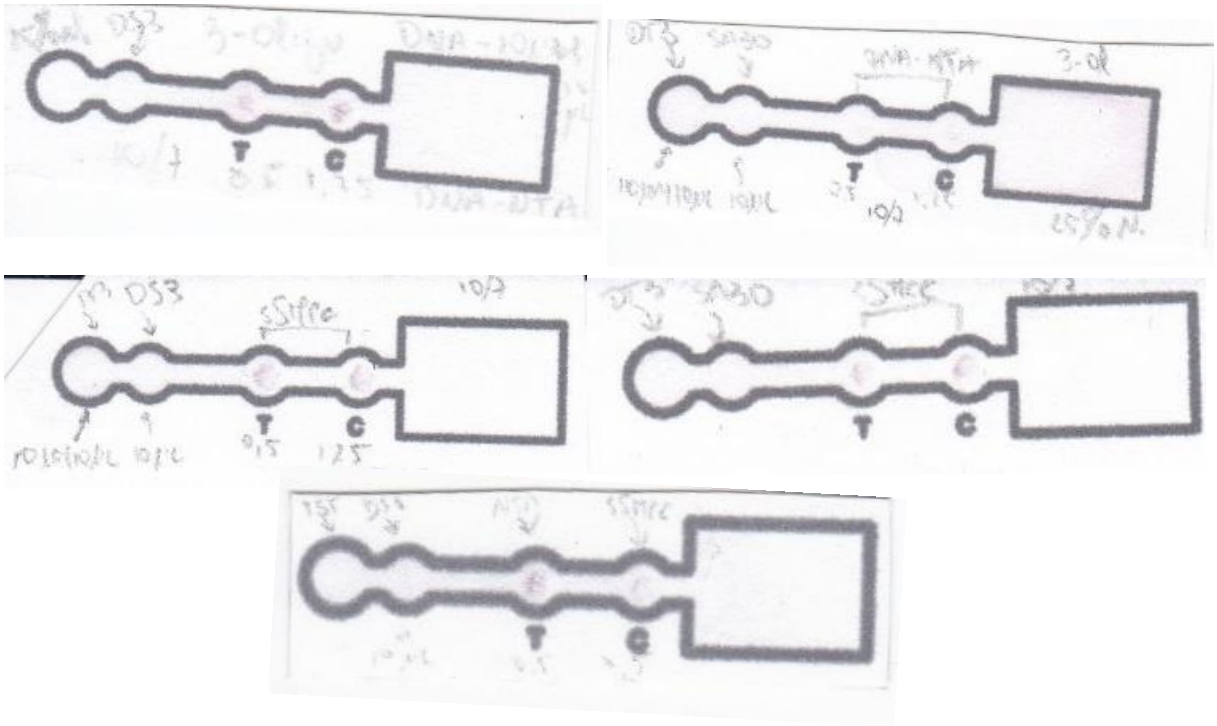

Figure II-7: µPAD tests with CBM3-C:D3N3 and CBM3-C:DN3 conjugates, concerning section 4.4.2., 3-oligonucleotide capture system. Top row, left: CBM3-C:D3N3 conjugated with 25% nickel excess tested with AuNPs functionalized with the complementary DNA strand DS3. Addition of 10 µL of 10 µM DT3 oligonucleotide solution was performed to the sample loading site, as well as 3.3 pmol and 8.2 pmol of CBM3-C:DN3N conjugate to the test and control spots, respectively. Top row, right: CBM3-C:D3N3 conjugated with 25% nickel excess tested with AuNPs functionalized with the non-complementary DNA strand SA30. Addition of 10 µL of 10 µM DT3 oligonucleotide solution was performed to the sample loading site, as well as 3.3 pmol and 8.2 pmol of CBM3-C:DN3N conjugate to the test and control spots, respectively. Middle row, left: CBM3-C:DN3 tested with AuNPs functionalized with the complementary DNA strand DS3. Addition of 10 µL of 10 µM DT3 oligonucleotide solution was performed to the sample loading site, as well as 4.8 pmol and 12 pmol of CBM3-C:D3N conjugate to the test and control spots, respectively. Middle row, right: CBM3-C:DN3 tested with AuNPs functionalized with the non-complementary DNA strand SA30. Addition of 10 µL of 10 µM DT3 oligonucleotide solution was performed to the sample loading site, as well as 4.8 pmol and 12 pmol of CBM3-C:DN3 conjugate to the test and control spots, respectively. Bottom row: CBM3-C:D3N3 conjugated with 25% nickel excess and CBM3-C:DN3 tested with AuNPs functionalized with the complementary DNA strand DS3. Addition of 10 µL of TST buffer was performed to the sample loading site, as well as 3.3 pmol of CBM3-C:D3N3 and 4.8 pmol of CBM3-C:DN3 conjugate to the test and control spots, respectively. Freeze-functionalized AuNPs were used on all the aforementioned tests.

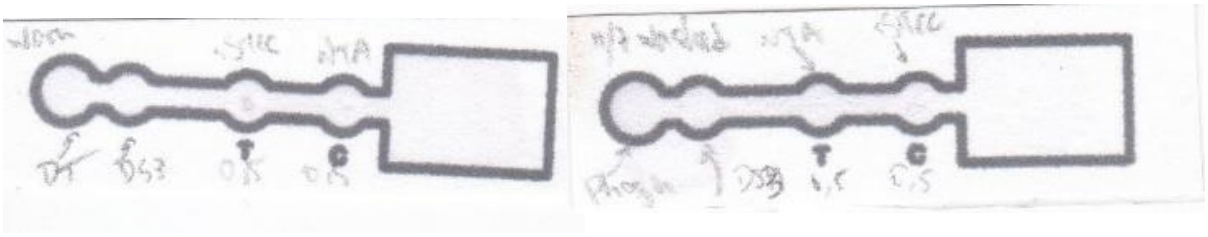

Figure II-8: µPAD tests with CBM3-C:D3N3 and CBM3-C:DN3 conjugates, concerning section 4.4.2.1., wash with low salt buffer. Left: CBM3-C:D3N3 conjugated with 25% nickel excess and CBM3-C:DN3 tested with AuNPs functionalized with the complementary DNA strand DS3. Addition of 10 µL of 10 µM DT3 oligonucleotide solution was performed to the sample loading site, as well as 4.8 pmol of CBM3-C:D3N and 3.3 pmol of CBM3-C:D3N3 conjugate to the test and control spots, respectively. Right: CBM3-C:D3N3 conjugated with 25% nickel excess and CBM3-C:DN3 tested with AuNPs functionalized with the complementary DNA strand DS3. Addition of 10 µL of 20 µM phosphate buffer was performed to the sample loading site, as well as 3.3 pmol of CBM3-C:D3N3 and 4.8 pmol of CBM3-C:DN3 conjugate to the test and control spots, respectively. After deposition of the conjugates, the device was washed five times with 20 µL of 20 µM phosphate buffer, pH 7.6. Freeze-functionalized AuNPs were used on all the aforementioned tests.